MASSIVELY PARALLEL PICK AND PLACE VIA ELECTROOSMOSIS

A Thesis

Presented to the Faculty of the Graduate School

of Cornell University

In Partial Fulfillment of the Requirements for the Degree of

Masters of Science in Mechanical Engineering

by

Cheryl Ann Perich

May 2012

ABSTRACT

The quest to move small objects quickly, efficiently, safely, and effectively has been a goal of robotics and manufacturing since the beginning of mass production and the decreasing size of components of technological interest (i.e. electronic components and other similar materials). While there is a lot of diversity in the mechanism of transport, such as the number of degrees of freedom in a robotic arm as well as the type and number of end efforts handling the object, there is still a lack of consistency, accuracy, and delicacy in moving millimeter, micro- and nano-scale objects. This paper explores the use of electroosmosis to transport mm-sized spheres which are used to assembly large scale objects. In contrast to previous works, [1, 2], which focused on using arrays of bridges to grab a single substrate, we demonstrate individually controlling each element in the array to pick up objects from positions of our choosing. The advantage of this water droplet method is that it allows for delicacy in transport due to the lack of mechanical grabbing mechanisms. What makes this device particularly unique is the ability to individually address each droplet channel to control the droplet growth. The droplet size can be predicted, and the emerging droplets and surface tension to pick up objects can be controlled prior to any motion. Furthermore, this device has the capability to be expanded for massively parallel (on the scale of millions) assembly.

BIOGRAPHICAL SKETCH

Cheryl Ann Perich was born in Burbank, IL on September 10, 1987 to Bruce M. and Sandra A. Perich. She was raised in Orland Park, IL, attending public schools and participating in a variety of sports including gymnastics, lacrosse, and cross-country running. Her parents and brother were extremely supportive of all of her varied endeavors and encouraged her to constantly explore any and all interests she found. With their support, she was able to truly become a well-rounded individual with a support network that set the foundation for future success.

From there, Cheryl was the first in her family to attend college, seeking education at Marquette University. While many were able to find their passion immediately, Cheryl found herself enthralled by all subjects ranging from philosophy, French literature and culture, mathematics and engineering. Having studied many of these subjects beyond the necessary graduation criteria, she realized that her passions for philosophy and French literature could be full-filled through independent study and studying abroad, while her desire to utilize her strengths in mathematics and science could only be satisfied by perusing a Mechanical Engineering degree.

In this pursuit, Cheryl chose to embark on a five year graduation plan in order to co-op and gain real-world experience, working for Caterpillar Inc., The Boeing Company, and NASA during her rotations. These positions further deepened her passion for engineering and technology. In these times she was able to work in the Mission Evaluation Room (MER) for STS-127, sit inside both a space shuttle and an F-18, and to travel to a number of NASA sites and military bases, while helping to grow her passion for travel.

After graduation, Cheryl spent six week backpacking through Europe in order to learn more about other cultures, learn how to interact with those different from herself, and learn how to problem solve in difficult situations. It was an experience that has greatly shaped the way she thinks about the world around her and how her work will affect

society as a whole. From there, Cheryl attended Cornell University on a New York Space Grant Consortium scholarship, and later received an NSF Graduate Student Researchers Program Fellowship. Cheryl then began work in the Creative Machines Laboratory, under advisor Dr. Hod Lipson. Her project allowed her to collaborate with the Chemical Engineering department and the Steen Group. Her time at Cornell has allowed her to learn how to be a proper independent researcher, how to problem solve in areas that were new to technological progress, and contribute to the future of technology. Upon graduation, Cheryl will be entering an Operations Leadership Development Program that will combine her past experiences with her interest in business management. In this program she will pursue a Masters in Business Administration. Beyond occupational plans, she hopes to continue her passions for travel and aforementioned interests in her spare time.

To my parents who have constantly supported me throughout all my endeavors, and to my brother, David, who has been an integral part in keeping me motivated and positive.

ACKNOWLEDGEMENTS

This work was supported by DARPA Grant No. W911NF-11-1-0093**,** NSF Grant No. DGE-0707428, and the New York Space Grant Consortium.

I would also like to give my deepest gratitude to the following people who have made this journey possible:

To Hod Lipson for constantly challenging me and for pushing me outside my comfort zone in order to intellectually excel.

To Paul Steen for welcoming me into his lab and his group, and for opening up a whole new world of chemistry, fluids, and engineering that I did not know existed.

To Erik Huber for helping me translate data, build models, understand porous medium, and most importantly, for constantly being a source of support throughout the entire process.

To Devin Lachowsky for helping me with most program tasks, and for being a motivating and supporting person through the ups and downs of this experience.

To Ashley Macner who has been there through all the trials and broken devices, and who has given hours of her time to troubleshoot the PICEM and to encourage me to continue pushing through the tough times.

To Robert MacCurdy for constantly being my go-to person for all of my questions--be it large or small.

To all the members of the Creative Machines Laboratory for all their constructive criticism and input throughout the phases of this project.

TABLE OF CONTENTS

LIST OF TABLES

LIST OF FIGURES

CHAPTER 1

INTRODUCTION

In the last few decades, automated assembly processes have played a key role in the rate, cost, and complexity of product manufacturing. Assembly processes are critical when a product comprises multiple parts that cannot be co-fabricated, but instead are made separately and then assembled. For many production processes, the assembly stage is the most rate limiting factor, often the only step involving manual labor.As the complexity of products we consume increases, the role of automated assembly will become increasingly critical. One way to alleviate this bottleneck is to explore methods for parallel assembly, allowing multiple parts to be assembled simultaneously. The goal of this research is to explore methods for parallel assembly that will scale to very large numbers of components – potentially allowing the parallel assembly of millions of components at the same time, a process we call *Massively Parallel Assembly*.

Traditional, low-count parallel assembly has helped to decrease assembly time. For example, the bottling industry has used parallel assembly in order to cap and fill multiple bottles at once. The solar cell industry has used suction cups to pick and place solar cells throughout the production line. Even the circuit board industry has incorporated some use of parallel assembly to increase the speed of production. However, none of these processes are massively parallel: They move objects on the scales of ones, tens, and at most hundreds. However, were this process to become massively parallel, on the scale of millions, the rate of production would greatly increase.

At the millimeter, micro- and nano-scale production, this idea of parallel assembly, let alone massively parallel assembly has not yet been explored. In the world

of electronics, components have become exponentially smaller as time progresses. Using massively parallel assembly, it would be possible to assemble objects more quickly, efficiently, and even more accurately. In robotics, it would be possible for large scale integration levels for essential building blocks for robotic structures. The possibilities for massively parallel assembly on small scales would allow for the ability to quickly and efficiently assembly the tiny structures necessary for the electronic components, robotic structures, computer integration and microstructures that are quickly becoming integral parts of our daily lives. This work looks at integrating the industry standard of parallel pick and place but as a means of moving small (less than 1 mm) object in a massively parallel fashion.

There are three main issues to consider when deciding on a transport method for a small object. First, the end effector has to be uniquely and specifically designed for a predetermined shape and has to be able to pick up the object without destroying or damaging the part. Second, the devices currently designed to pick up these small objects tend to be extremely delicate, often as delicate as the objects they are trying to pick up. This leads to major issues in speed of motion, since all objects must be carefully controlled. Finally, repeatability of the picking motion is essential for large scale operations; picking each object individually, one at a time, is an extremely slow and tedious process. The repeatability and reliability of the end effector can be increased by using parallel pick and place operations. Some of the current pick and place mechanisms are discussed further.

A common end effector is a vacuum where glass pipettes are used to harness the effects of electrostatic attraction, Van der Waals forces, and capillary forces [3]. This

vacuum idea, however, is not usually a parallel process, allowing for only one object to be picked up at a time due to the need of an extensive control system and multiple tool systems on small scales to adjust the object. Furthermore, the releasing process is based on scraping the object off of the vacuum making it next to impossible to accurately place an object. Another popular choice has been the use of tweezers, attached to a parallelogram robot, which has been fabricated in nanofabrication facilities to pick and place three-dimensional micro structures from fine particles [4-12]. While these tweezers and other end effectors can be arduously designed for specific shapes using photolithography or silicon etching, they are not universal and the tool head itself is now just as delicate as the tiles they pick up. Some techniques use cylinders with electrostatic forces to manipulate tiles [5-6], others use simple dual cylinder tweezers [7] or even more complex hinged structures using plastic deformation to perform their moving assignments [8-10]. Each has their own inherent flaw, be it the complication of the end effector geometry to the delicacy of the device, to the lack of repeatability of the pick and place procedure. Other techniques go further utilizing not only Scanning Electron Microscopes (SEM) in their movements but including Atomic Fore Microscopy (AFM) [11-12]. These techniques, some using soldering to move and remove parts or laser ablation for decomposition, are beneficial in that there is easy identification of manipulation location, high efficiency in user-friendly design, and material extraction in micron and nanometer scales. However, hysteresis and creep decrease reproducibility and material manipulation is limited to mainly cutting applications [11]. While these techniques could theoretically be used in parallel by combining more than one end effector to robotic arms or increasing their

number of machines, they do not have the capacity for massively parallel motion, to the degree of millions of objects being transported.

Other techniques use chemically triggered micro grippers. While this technique requires low energy input, it requires the submersion of materials in chemicals, which could degrade and deform potential components [13]. In looking further into liquid assembly, self-assembly through use of water droplets has been used to align tiles, removing some of the precision boundaries in assembly [14-15]. However, these techniques still require external grippers or mechanisms to manipulate the tiles. In previous work explored the Creative Machines Laboratory, parallel rapid assembly using spherical components (the same as used in experiments conducted in this paper) was explored. Pre-fabricated elements were poured into feeders and self-aligned into a lattice structure and wetted using a deposition tool. A projector was used to selectively dry unwanted cells, and the head was put into contact with the matrix picking up only the wetted spheres. This could be repeated for multiple layers. While this technique is a step in the direction of massively parallel assembly, the feeding tools and self alignment cause limitations on large scales. Optical drying can also become arduous if extended to a larger matrix [35].

The inspiration for the PICEM (Parallel and Individually Controlled Electroosmosis Mechanism) stems from work in developing the Electroosmotic Droplet Switch (EODS) and the Switchable Electronically-controlled Capillary Adhesion Device (SECAD) [1-2]. The EODS used an electroosmosis pump and varying voltages under 5 V to displace water between two nozzles. The electroosmosis pump was, in effect, used to balance surface tension and capillary forces. In cases, they were able to pick and drop

a piece of aluminum foil with the aid of two spacer pins and to grab an offset sphere using a droplet growth and withdrawal [1]. The SECAD, drawing upon this work, uses electroosmosis to move an array of droplets which form capillary bridges upon contact with a single substrate [2]. See Figure 1.1. It is mentioned that individual or regional addressability is possible, which would allow for real-time wettability gradients that could move objects along a path. However, the full extent of electroosmosis and its use for pick and place has not yet been explored.

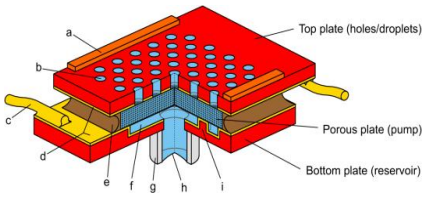

Figure 1.1: SECAD cutaway [1].

By using the PICEM device as described in this paper, it is possible to avoid the complications involved in creating micro-fabricated tweezers or end-effectors. Other benefits include self-alignment of tiles as a result of the drops seeking the lowest energy state and individual channel addressability to selectively pick and place small objects.

CHAPTER 2

DESIGN OF THE PICEM AND ROW TESTING

2.1 ELECTROOSMOSIS AND THE PICEM

When a liquid and solid are introduced, such as distilled water into a borosilicate glass frit, an electric double layer of counter ions will form at the liquid-solid interface. When a tangential electric field is applied, the ions in this double layer succumb to Coulombic forces and move towards the electrode of opposite polarity. As this happens, the fluid near the wall moves with these ions due to viscous forces, creating what looks like a plug flow in the bulk fluid [21]. If a porous frit is used as the solid, a considerable pressure drop occurs across the frit, which must be taken into consideration when looking at bulk flow of fluid through the medium. The smaller the channels or pores, the larger the capillary pressure is across the menisci [22]. This phenomenon allows for fluid motion without any mechanical devices necessary to control a constant, pulse-free fluid flow. The ideal properties of this pump are large flow rates and high maximum pressures, meaning that the porous medium should have small pores for high pressure generation and a large surface charge density to ensure maximum flow rate [22].

The PICEM device was created using mainly 3D printed components (See Figure 2.1). Besides the electrodes, printed circuit board, O-ring and connectors, all layers were created using Objet 3D printed soft and hard materials (photocurable plastic and rubber-like materials). The soft Tango+ material (tensile strength 0.8-1.5 psi) allows for a rubber-like flexibility, which, under the compression of the screws and top plate, serves as a means of keeping the water in their directed channels [18]. Furthermore, it allows for a

tight fit around the borosilicate glass frit, which is integral in ensuring that the electroosmosis process occurs. The SolidWorks parts can be seen in Figure 2.2. A syringe was used to fill the reservoir and provide a water source to replenish water lost via evaporation. A cross section of the device can be seen in Figure 2.3.

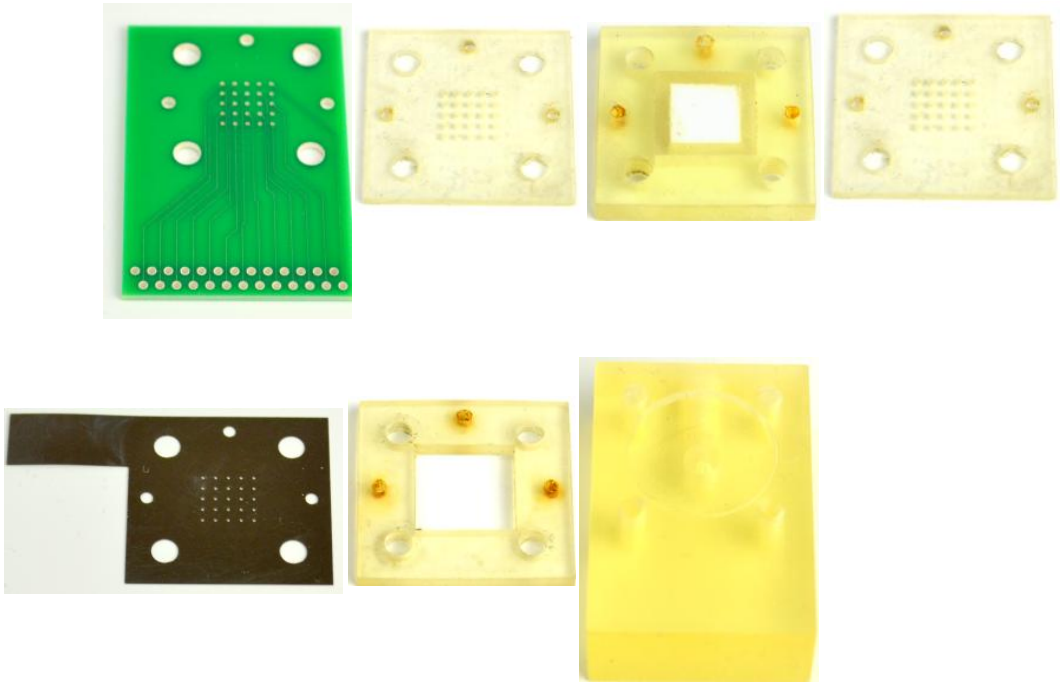

Figure 2.1: PICEM components. From left to right: printed circuit board, Tango + gasket, Fullcure 720 outer support with Tango+ inner frit support and borosilicate glass frit, Tango+ gasket, stainless steel electrode, Fullcure 720 plate, Fullcure 720 reservoir. Not shown: secure pins, screws, syringe fixture, O-ring which sits in reservoir, rubber ring inside of O-ring.

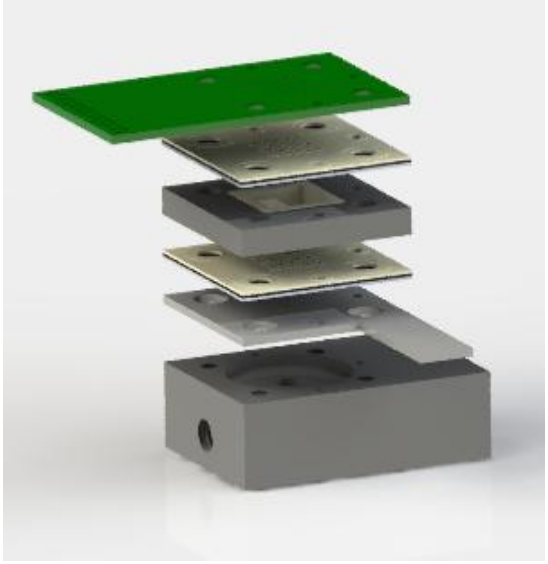

Figure 2.2: SolidWorks images of parts. Light yellow materials signify Tango+ material; dark grey signifies FullCure720 (or VeroBlack). Also included: Circuit board and silver electrode.

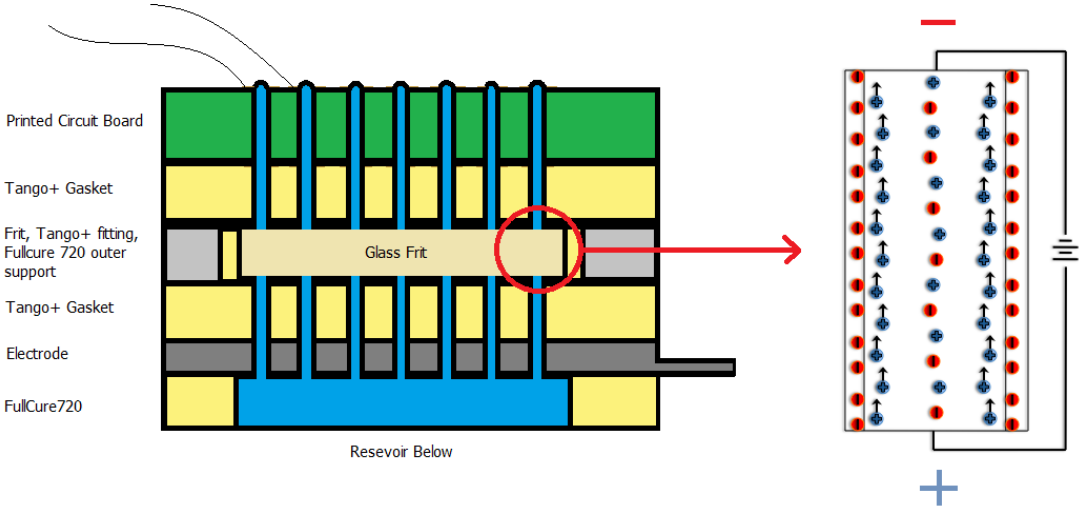

Figure 2.3: Close up of PICEM cutaway and the electroosmosis process occurring through pores [23].

The most important feature of this device is the printed circuit board head. Two configurations of the circuit board head were tested. The first allowed for the individual control of columns of the device, where each row has either a different hole diameter and Si/Pb plating diameter. This set-up allowed for the testing of the use of individual control

as well as exploring the accuracy and limitations of printed circuit board components on small scales. The second device, which is the final goal of this exploration, allows for the individual control of each channel. This new circuit board is connected to an insulation displacement connector (IDC) and to a ribbon cable. The ribbon cable allows for the individual connection of chosen channels when clamped to a voltage source. The basic procedure can be seen in Figure 2.4.

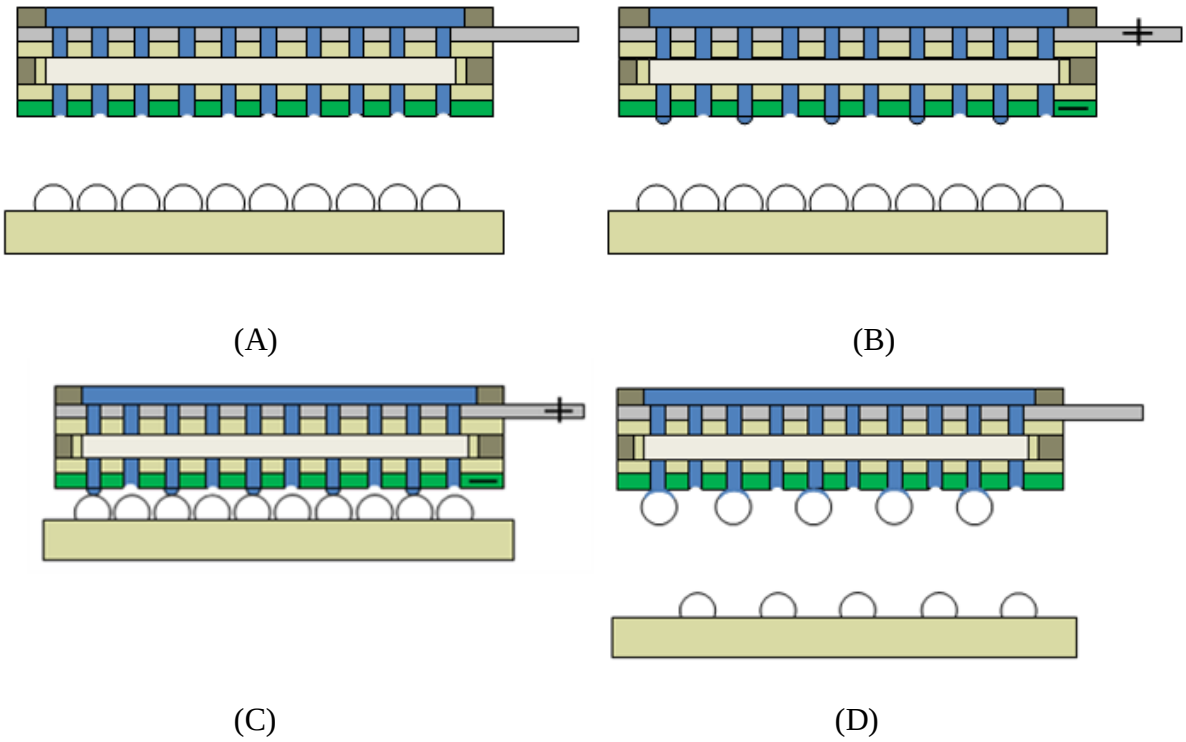

Figure 2.4: Basic Process: (A) PICEM device is brought into alignment with base and spheres. (B) A voltage is applied causing the water droplets to form in the selected channels (ever other channel). (C) The PICEM device is brought into contact with the spheres. (D) The base is pulled away from PICEM device and the selected spheres are removed.

2.2 Row Connections

Initial testing began with the connected arrays under a microscope. This allowed for the visual display of water movement inside the channels before they are visible to the naked

eye, as well as allowing one to see more in depth any unwanted effects on the other inactivated channels. The printed circuit board also allowed for rows of droplets to be addressed and stimulated independently of the other rows of the board. The board, as seen in Figure 2.5, consists of a 6 x 6 matrix of holes. The rows were divided into sets of two, allowing for testing of different size holes, and therefore different size droplets. The diameter sizes from left to right are 14, 20, and 25 mils. The coating of the holes was a base of copper with a Sn/Pb (ratio of 63/37) coating. The coating diameter varied for each row to test the ability of the holes to have a consistent ring of Sn/Pb coating around the edges since the accuracy in punching the holes into the top coated circles was reaching the limits of precision for the company used (PCB Unlimited). However, it can be seen that the rings were able to encircle the holes for all arrays, meaning that smaller electrode rings can be used to allow for closer placement of the droplet holes.

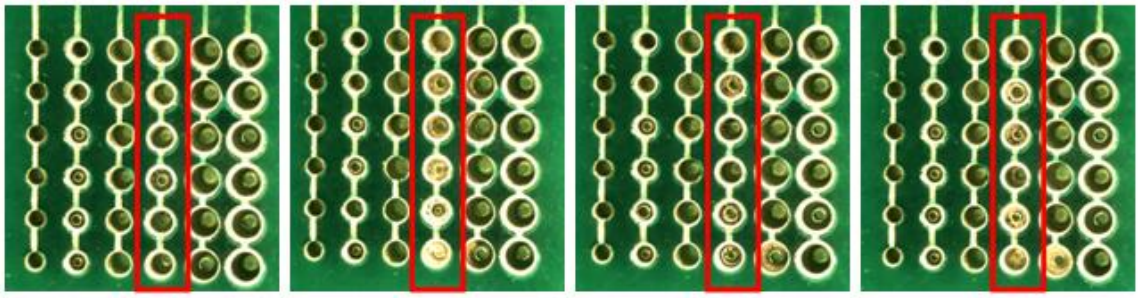

Figure 2.5: Microscopic view (20x) of channel water growth over time. Time from left to right: 2 sec: 0V no water growth; 12 sec: 27 V water growth in selected row, 37 sec: 0 V: No growth seen; 70 sec: -27 V water droplets recess into channels.

One of the major issues encountered using this microscope was the view angle. The microscope was only able to look at a top view of the droplets, making it difficult to determine volumes of the droplets. However the reflection of the microscope light on the droplets, which formed a ring on the water, helped to determine the size of the droplets as

they grew and shrunk with the changing voltages. Beyond this difficulty, it was noted that air bubbles were present inside of the water droplets—an issue not encountered using the previous SECAD. These air bubbles could potentially interrupt and change the surface tension of the water droplets, and thus affect the ability and consistency of the droplets to pick and place tiles effectively.

The creation of these bubble formations could be due to a number of reasons. One theory involves the degradation of the frits over time, and the fact that these frits are not direct cylindrical channels but instead compressed glass cylinders with varied directional flows. The frit that was used in this experiment has been used very often and for an extended length of time, and may be allowing air bubbles to become trapped.

Furthermore, the individually controlled arrays were tested, and it was found that the nearby arrays (either the next one or two rows over) were also forming droplets (and air bubbles). This issue could be due to the large voltage (30 V), and thus the large electric field being produced. Since the electric field acts in an elliptical shape (see Figure 2.6), other nearby holes could be receiving some of the field lines and thus a flow could be induced in the neighboring channels.

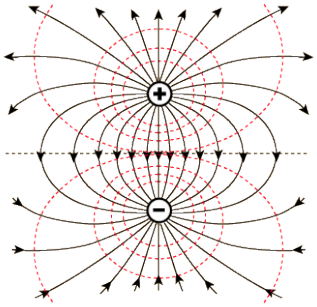

Figure 2.6: Electric field lines across two point charges. Notice how the electric field lines not directly vertical between the two charges give off field charges in both the upward and outward direction [16].

CHAPTER 3

INDIVIDUAL CONTROL OF CHANNELS

3.1 Individual Control of new PICEM Assembly

After exploring the intricacies of the printed circuit board, it was decided to utilize the 20 mils diameter holes with the 0.66 mm diameter plating in a 5 x 5 array. This was chosen due to the comparative droplet size created (ideally 20 mils in diameter without losing shape or overflowing past the channel circumference, also known as walking), which would be ideal in contacting as much surface area of our tiles or spheres as possible. It was chosen to space the channels 2 millimeters apart (which would mean it could pick up every 4th 500 micron tile or each 1.5mm sphere). This spacing was chosen to better analyze the effects of spacing with regards to the vector components of the generated electric field in the inactivated channels. The PICEM individually controlled channel version can be seen in Figure 3.1.

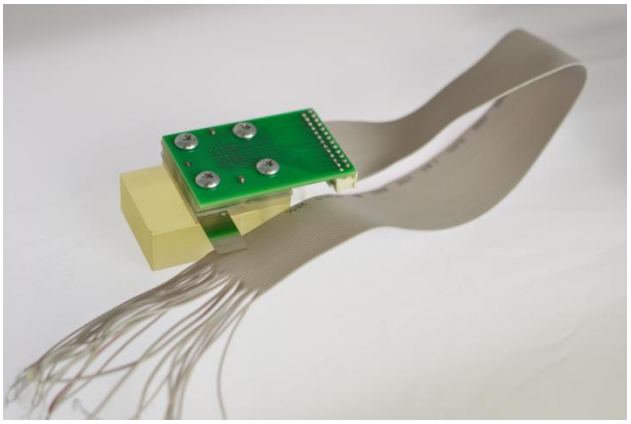

Figure 3.1: PICEM with individual addressability.

Tests were performed by individually selecting the channels by the corresponding ribbon cable wire and connecting those wires to a switch, battery source, and the electrode. Trials were conducted to create a "C" shape, and multiple successful trials were able to produce the desired droplet configuration. No unwanted water growth in other channels was experienced, and at a voltage of 15 V, no air bubbles were observed. Based on this information, the spacing allowed for the electric field to be weak enough not to affect the local neighboring channels, and the lower voltage reduced air bubble creation from hydrolysis. See Figure 3.2 for test trials.

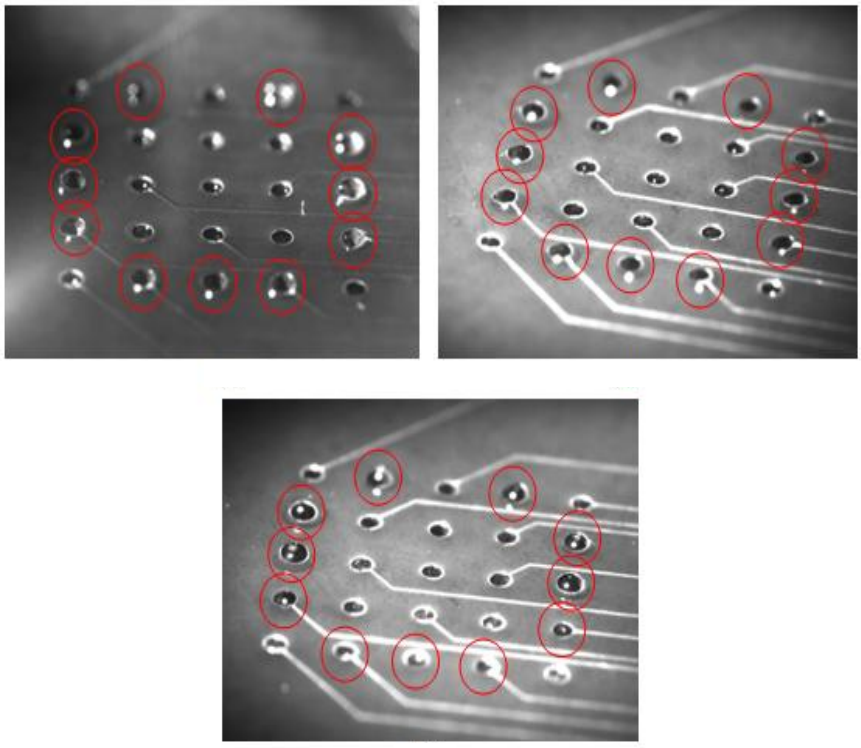

Figure 3.2: Three successful trials of creating a "C" shaped configuration using individual control (20x magnification).

3.2 XYZ Platform Testing

An XYZ platform was built in order to allow mobility of the PICEM device in all three axes. This would allow the device to pick up tiles or spheres from any location on the platform and place them to any other location on the platform. The device electronically consists of three servo motors and a Snap hub, while structurally it is composed mainly of laser cut acrylic, 3D printed joints and connectors, and metal poles to connect the structure.

It is controlled using a Visual Basic program modified from previous work [17], whose template was the inspiration for this current platform. The program allows for homing, selection of speeds, accelerations, and positions of the assembler head. See Figure 3.3-3.4.

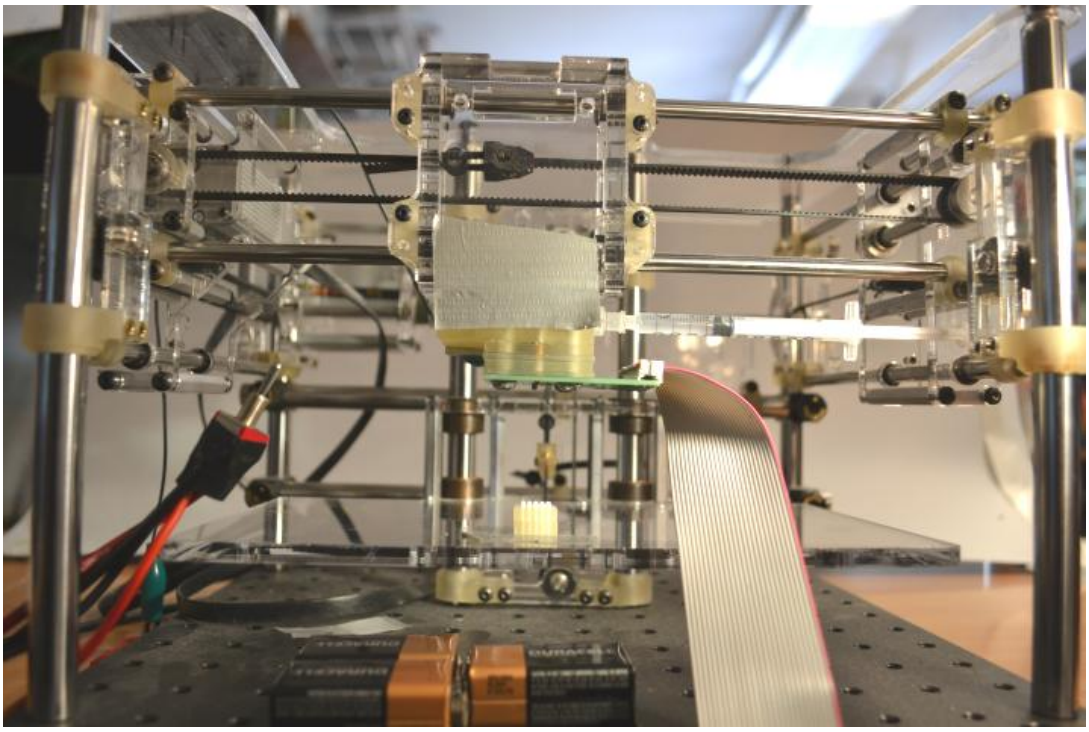

Figure 3.3: XYZ Platform with PICEM.

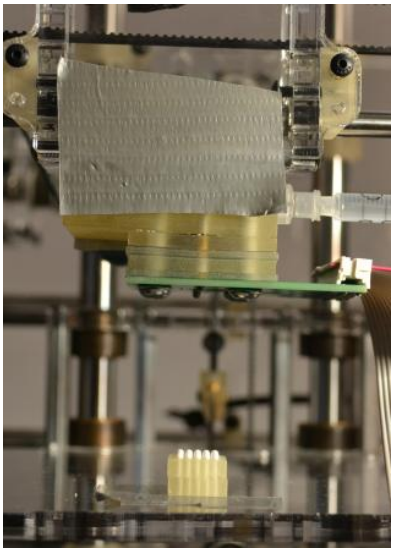

Figure 3.4: Close up of sphere platform and PICEM device.

3.3 Testing the Picking ability

To test the device, the PICEM device was attached with adhesive tape to the translating head. The device was then aligned using pins to the base plate which was a 3D printed Fullcure720 cube with cylindrical holes of diameter 0.7 mm. The plastic spheres of diameter 1.5 mm were placed on this platform spaced in such a way that the PICEM would pick up all spheres with no space in between, were all channels to be activated. This same configuration would work for smaller tiles; however, it would only pick up every fourth 500 micron tile, meaning it would thus require multiple passes to complete a row on a tile platform. Tile platforms have been created using both photolithography and 3D printing, but have not been thoroughly tested since the tile geometric configurations are much more complex than the spherical objects currently studied, and their final

geometric configuration has not been confirmed. In future tests, these tiles could be used in order to test interlocking abilities, as well as stacking capabilities.

Once all PICEM channels were tested for current flow capacity, individual channels were activated by selecting the proper wire from the ribbon cable and connecting it to the voltage source. A switch was created in which the device would allow for positive voltage, negative voltage, or no voltage to generate electric fields through the channels. This allows for the droplets to grow and shrink on command. The first of many tests looked at a single channel. The single wire corresponding to the leftmost forward sphere was activated (15 V), and using the Visual Basic Program, the platform was lifted such that the spheres made contact with the formed water droplet. No other droplets were formed since the other channels were not activated. After contact was made, the platform was then lowered, showing the single chosen sphere to have been removed from the platform and adhered to the circuit board. The voltage was switched off and the sphere continued to stay in place. This shows the novelty that this device uses low voltages only periodically to control droplet motion, while still allowing peak performance. This test was repeated for a number of individual channels, all showing similar results. This process can be seen in Figure 3.5.

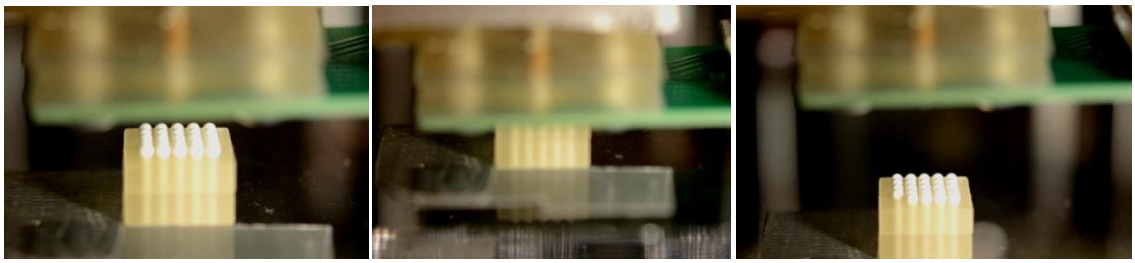

(A) (B) (C)

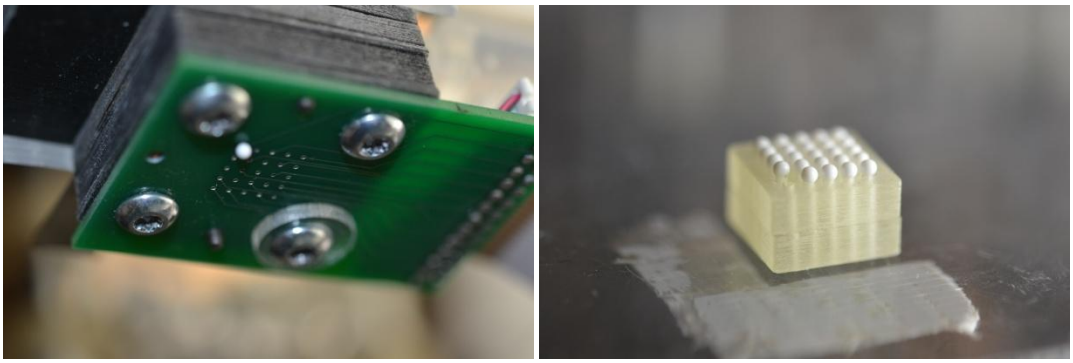

(D) (E)

Figure 3.5: (A) Initial platform with all spheres. (B) Sphere making contact with water droplet. (C) Single droplet removing forward, left-most sphere. (D) View of circuit board. (E) View of empty sphere platform.

This test was repeated for a number of individual channels, all showing similar results. The next step was to activate multiple channels at once. Therefore, a row was chosen to be activated. In the following images (Figure 3.6) the process can be seen again, but with multiple channels activated.

(A) (B) (C)

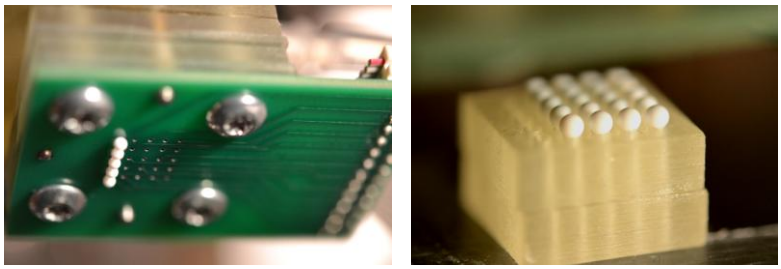

(D) (E)

Figure 3.6: (A) Initial platform with all spheres. (B) Spheres making contact with water droplets. (C) Droplets removing entire row. (D) View of circuit board and droplets. (E) Final view of platform with missing row.

3.4 Under the Microscope

To better evaluate the droplet growth, a microscope was used to view the changes inside the channels and water droplets on an individual and collective scale (referring to how each activated channel affects inactivated channels). Based on Figure 3.7, the device was connected to 9 V battery (A), and the second to bottom row was activated (B), deactivated (C), and re-activated with a negative voltage (D). Throughout this process, based on the rings of light on the water droplets, growth and recession can be seen from an overhead view. By looking at the other channels around the row, it is possible to determine if any other channels were activated as shown in the connected column tests as previously mentioned. At this reduced voltage and higher channel spacing, minimal unwanted growth is experienced. In (C) some of the channels in the lower right hand corner seem to show some activation with both positive and negative voltage. However, it seems that these tend to be much less extensive than those chosen to be actuated. This issue could be resolved using a control system with negative voltage being supplied to the nearby channels to prevent actuation. On a more practical note, these droplet growths are of no concern as long as they are not large enough to become visible above the level of the circuit board. Furthermore, very little bubbling has been seen from hydrolysis, which is likely a product of the lowered voltage.

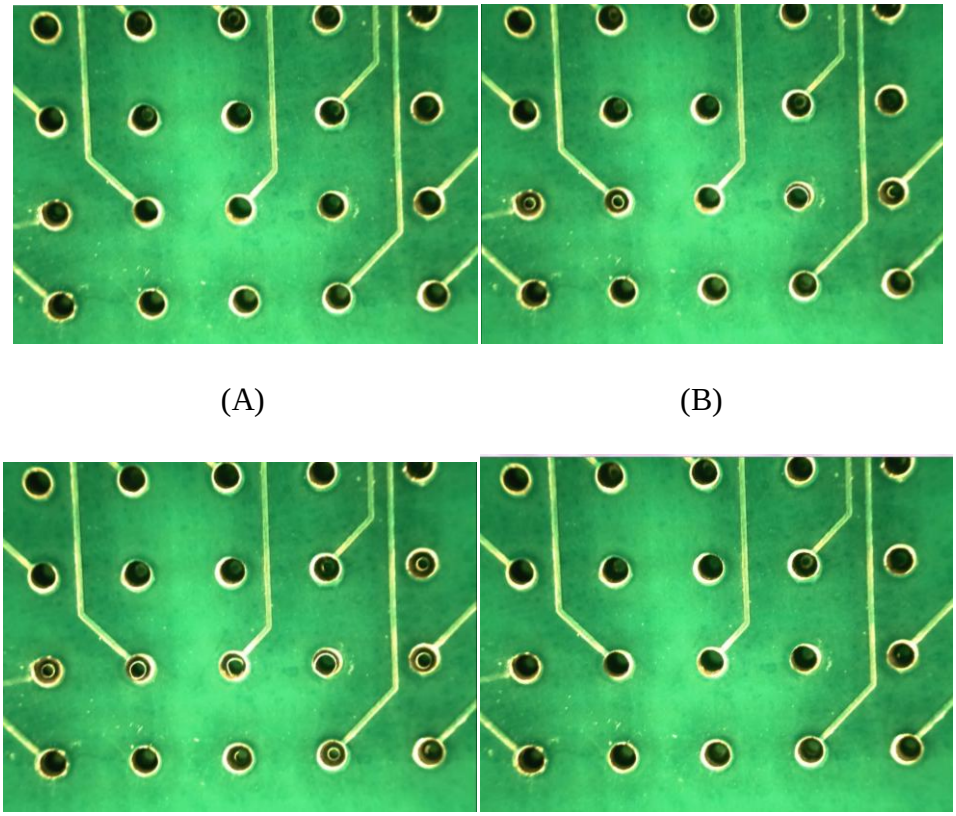

(A) (B)

(C) (D)

Figure 3.7: Magnification 20x. (A) Time: 28 sec, 0 V. (B) Time: 46 sec, 9 V. (C) Time 68 sec, 9 V. (D)Time: 79 sec, -9 V.

CHAPTER 4

TESTING UNIQUE CONFIGURATIONS

4.1 Materials Update on PICEM

Over time, some of the FullCure720 material parts were showing crack propagation around the screw holes due to the stress of screw compression. Therefore many of the FullCure720 materials were replaced with VeroBlack. The material properties of these two Objet materials can be seen in Tables 4.1 and 4.2.

Table 4.1: FullCure720 Material Properties [18].

Objet FullCure720					
	ASTM	Units	Metric	Units	Imperial
Tensile strength	D-638-03	MPa	50-65	psi	7250-9450
Elongation at break	D-638-05	%	15-25	%	15-25
Modulus of elasticity	D-638-04	MPa	2000-3000	psi	290,000-435,000
Flexural Strength	D-790-03	MPa	80-110	psi	12000-16000
Flexural Modulus	D-790-04	MPa	2700-3300	psi	390,000-480,000
HDT, °C @ 0.45MPa	D-648-06	°C	45-50	°F	113-122
HDT, °C @ 1.82MPa	D-648-07	°C	45-50	°F	113-122
Izod Notched Impact	D-256-06	J/m	20-30	ft lb/inch	0.375-0.562
Water Absorption	D-570-98 24hr	%	1.5-2.2	%	1.5-2.2
Tg	DMA, E»	°C	48-50	°F	118-122
Shore Hardness (D)	Scale D	Scale D	83-86	Scale D	83-86
Rockwell Hardness	Scale M	Scale M	73-76	Scale M	73-76
Polymerized density	ASTM D792	g/cm3	1.18-1.19		
Ash content	USP281	%	0.01-0.02	%	0.01-0.02

Table 4.2: VeroBlack Material Properties [18].

Objet VeroGray FullCure850, VeroBlack FullCure870, VeroWhitePlus FullCure835					
	ASTM	Units	Metric	Units	Imperial
Tensile strength	D-638-03	MPa	50-65	psi	7250-9450
Elongation at break	D-638-05	%	10-25	%	10-25
Modulus of elasticity	D-638-04	MPa	2000-3000	psi	290,000-435,000
Flexural Strength	D-790-03	MPa	75-110	psi	11000-16000
Flexural Modulus	D-790-04	MPa	2200-3200	psi	320,000-465,000
HDT, °C @ 0.45MPa	D-648-06	°C	45-50	°F	113-122
HDT, °C @ 1.82MPa	D-648-07	°C	45-50	°F	113-122
Izod Notched Impact	D-256-06	J/m	20-30	ft lb/inch	0.375-0.562
Water Absorption	D-570-98 24hr	%	1.1-1.5	%	1.1-1.5
Tg	DMA, E»	°C	52-54	°F	126-129
Shore Hardness (D)	Scale D	Scale D	83-86	Scale D	83-86
Rockwell Hardness	Scale M	Scale M	73-76	Scale M	73-76
Polymerized density	ASTM D792	g/cm3	1.17-1.18		
Ash content VeroGray, VeroWhitePlus	USP281	%	0.23-0.26	%	0.23-0.26
Ash content VeriBlack	USP281	%	0.01-0.02	%	0.01-0.02

The VeroBlack was chosen as a replacement because of its similar material properties. It can be seen that the tensile strength, modulus of elasticity, hardness, etc, are all very similar. However, it has been found through experiment that the VeroBlack tends to resist cracking much better than the Fullcure720, and was therefore used as a replacement for many of the FullCure pieces. Furthermore, many of the Tango+ gaskets were tearing, again, due to the stress induced by the screws. They were also found to be absorbing water throughout the process, making it difficult to ensure proper water flow through the channels. Therefore a new design was created, using the digital materials option on the Connex500 3D printer, in which multiple materials can be printed simultaneously. To increase rigidity of the gasket, a VeroBlack core was used with a Tango+ coating. The VeroBlack helps to prevent ripping at the screw and dowel holes, while the Tango+ allows for the flexibility of a rubber like material to make a tight compression fit around the channels. To further prevent water leaking, raised seals were designed and placed around the screw, dowel and channel openings to increase the compression in these areas. The new design can be seen in Figure 4.1-4.2.

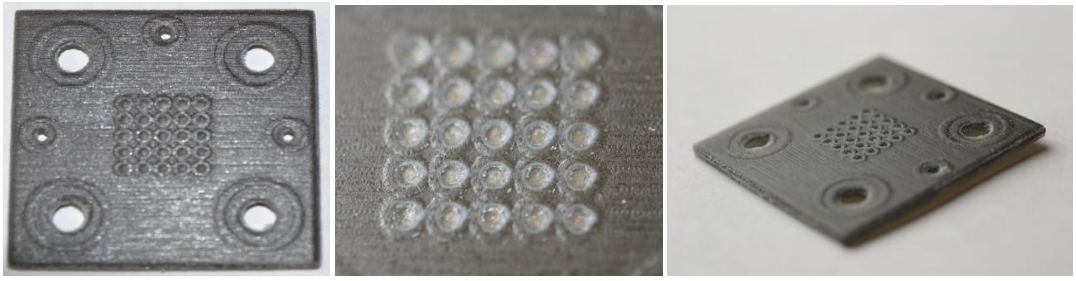

Figure 4.1: New gasket design with Tango+ and VeroBlack in Digital Materials mode.

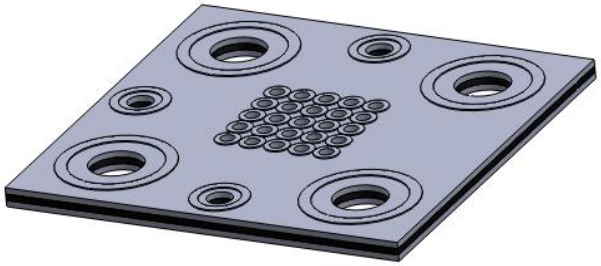

Figure 4.2: SolidWorks model of new gasket. Note the VeroBlack core and the grey top and bottom coating of Tango+.

Another modification included using the digital material mode on the Connex 500 3D printer. In the previous configuration, the frit was inserted into a square of Tango+ soft material. This composition was then inserted into a VeroBlack square with holes for final assembly. This configuration worked well for most trials, but over time, the gasket material (Tango+) would leave a gap between itself and the VeroBlack casing due to stress and deformation. Therefore a new model was used where the Tango+ and VeroBlack were printed as one object in Digital material mode, making the Tango+ square irremovable from the VeroBlack outer shell (Figure 4.3). This guarantees better seals between the gaskets and outer shell since the two materials were adhered together in printing under the UV curing process.

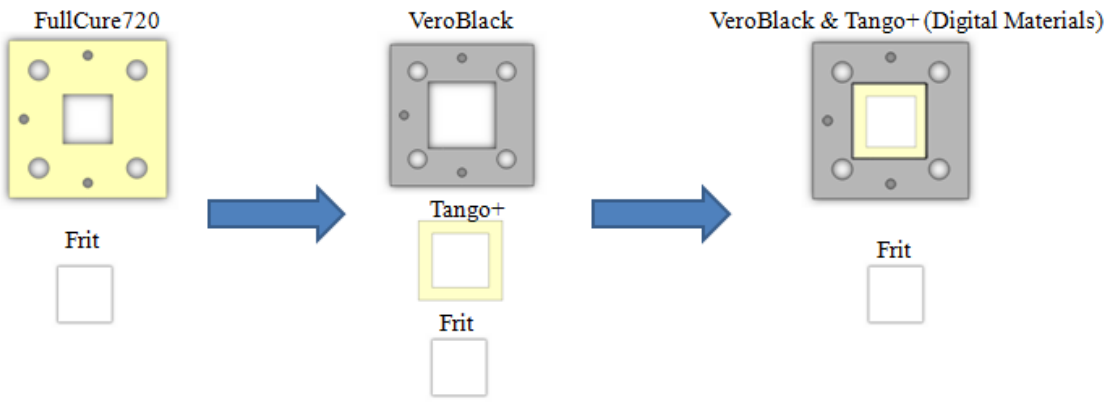

Figure 4.3: Transition from initial, improved, and final frit holders.

4.2 Picking up All Spheres

The next step was to attempt to pick up all spheres at once using the PICEM device. This test was performed 25 times, with a voltage of 15 V. The success rates and number of successful pick-ups per hole can be seen below in Figure 4.5 and 4.6. From these tests it was found that the lowest success rate was 80%, while the highest was at 100% for the 25 trials (Table 4.3). The mean and standard deviation amongst all the trials were calculated, with a mean of 22.72, standard deviation of 1.45, and an average success rate of 90.88%. These statistics were based on the Binomial Distribution. What is more important to note, however, is the success rate of water droplet formation. Although pickup was not 100% for each channel, the water droplet growth for the activated channels was seen in every trial, giving a success rate of 100% for every channel. This means that the electroosmosis process and the individual addressability features are fully functional, accurate, reliable, and repeatable.

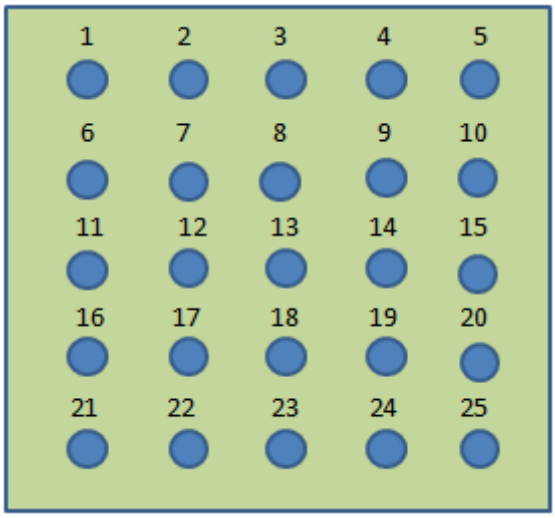

Figure 4.4: Basic numbering system for Figures 4.5-4.6, 4-9-4.10, 4.12-4.15.

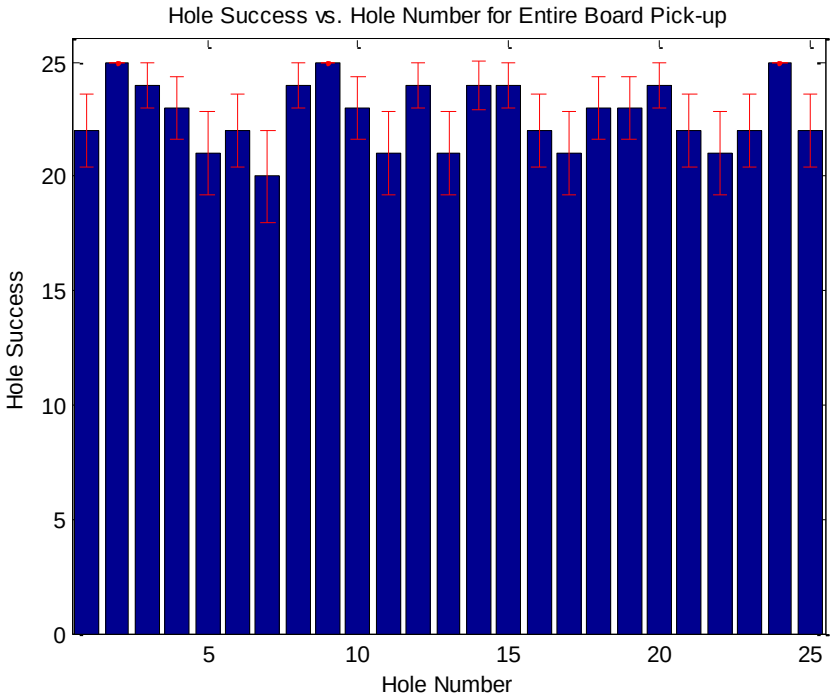

Figure 4.5: Hole Success vs. Hole Number for Entire Board Pick-up.

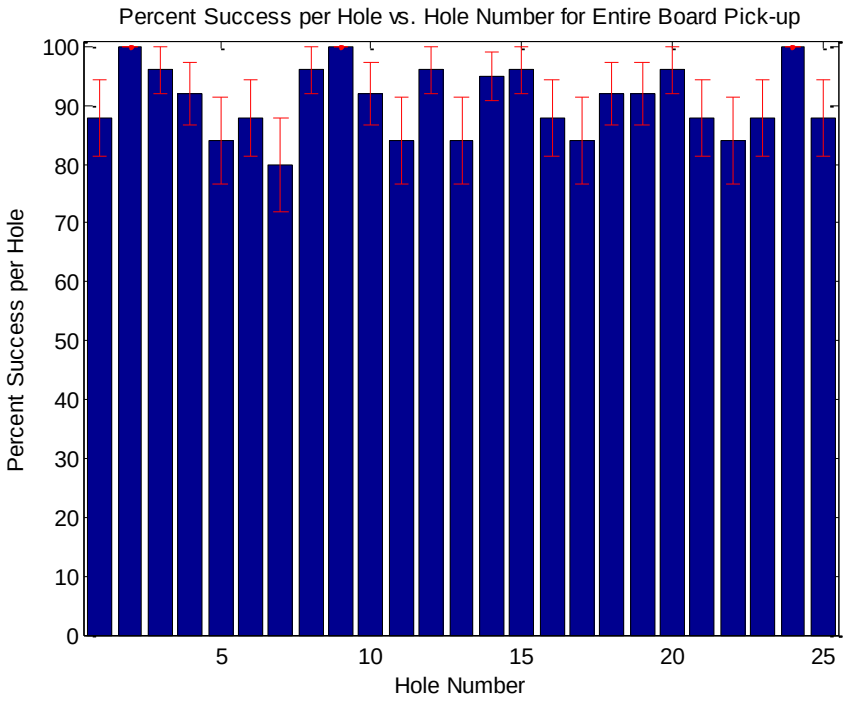

Figure 4.6: Percent Success vs. Hole Number for Entire Board Pick-up.

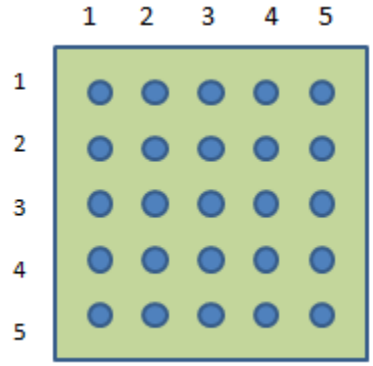

Figure 4.7: Basic numbering system for collected data in Tables 4.3 and 4.4.

Table 4.3: Collected data for 25 trials with standard deviations using numbering system in Figure 4.7.

Number of Successful Pick-ups Per Location						Percent Success Rate per Location for 25 trials					
Location	1	2	3	4	5	Location	1	2	3	4	5
1	22±1.6	25±0.0	24±1.0	23±1.4	21±1.8	1	88±6	100±0	96±4	92±5	84±7
2	22±1.6	20±2.0	24±1.0	25±0.0	23±1.4	2	88±6	80±8	96±4	100±0	92±5
3	21±1.8	24±1.0	21±1.8	24±1.0	24±1.0	3	84±7	96±4	84±7	95±4	96±4
4	22±1.6	21±1.8	23±1.4	23±1.4	24±1.0	4	88±6	84±7	92±5	92±5	96±4
5	22±1.6	21±1.8	22±1.6	25±0.0	22±1.6	5	88±6	84±7	88±6	100±0	88±6

4.3 Picking of Checkerboard Pattern

In order to test the accuracy of the individual control, a checkerboard pattern was tested. This configuration allowed for the testing of the ability to isolate channels in close contact, while still providing a deliberate pattern. Furthermore, it examined the effect of unwanted droplet growth on picking up individual spheres (Figure 4.8).

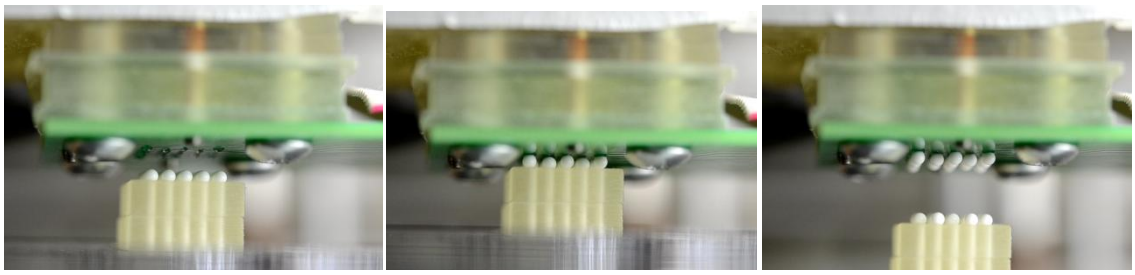

(A) (B) (C)

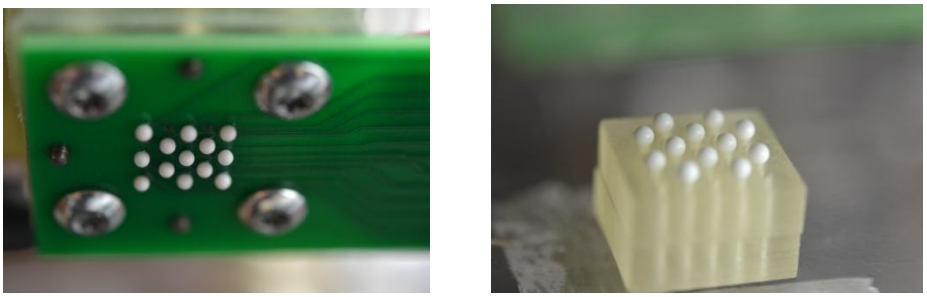

(D) (E)

Figure 4.8: (A) Set at 15V, water droplets begin to form on the circuit board of the PICEM device, (B) the platform is raised so that the droplets make contact with the spheres, (C) the activated channels (those creating a checkerboard pattern) pick up the spheres from the platform, leaving behind all spheres on the grid corresponding to inactivated channels. (D) View of checkerboard pattern from under the circuit board. (E) View of left over spheres from inactivated channels.

In order to test the reliability of this process, the test was repeated 25 times. The standard deviation and mean was calculated for both the number of successes per channel as well as for the probability of pick up (Figures 4.9-4.10, Table 4.4). Success is defined as an activated channel picking up a sphere or an inactivated channel not picking up a sphere. Starting with position 1, every other bar (1,3,5, etc) correspond to activated channels. All even numbered bars correspond to inactivated channels.

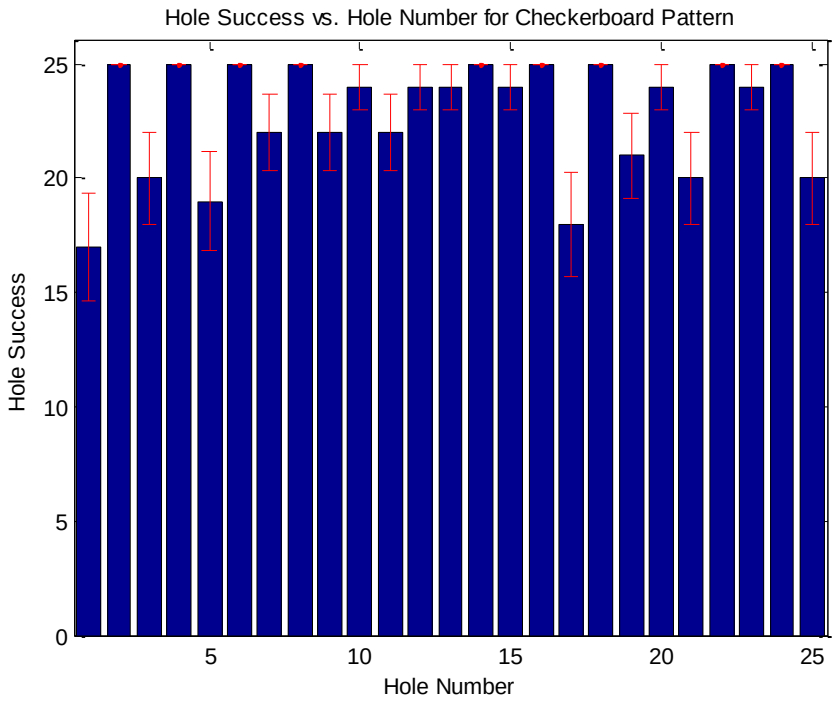

Figure 4.9: Hole Success vs. Hole Number for Checkerboard Pattern. Note same numbering system is used as in Figure 4.4.

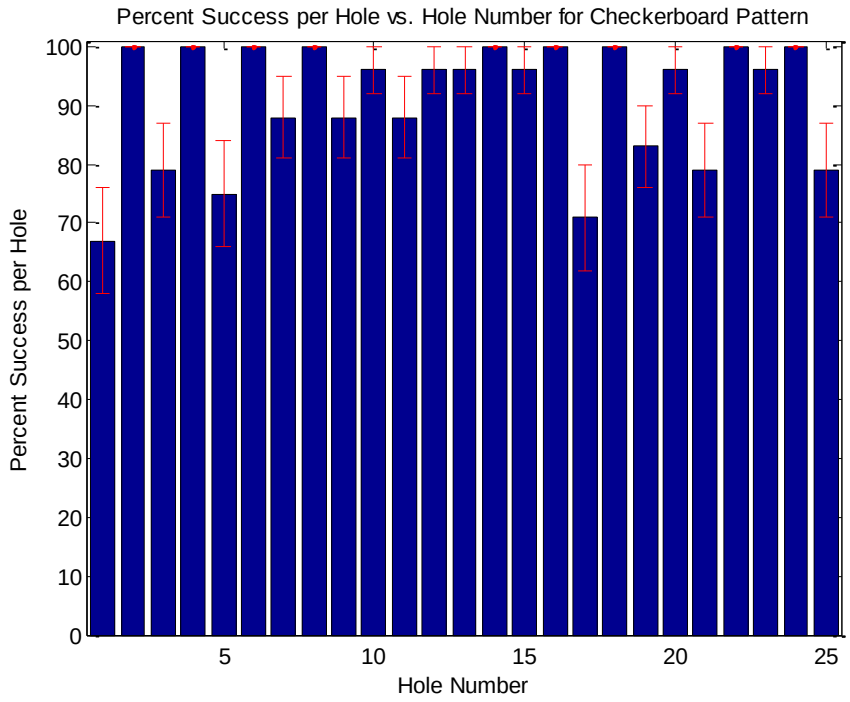

Figure 4.10: Percent Success vs. Hole Number for Checkerboard Pattern. Note same numbering system is used as in Figure 4.4.

Table 4.4: Collected data for 25 trials with standard deviations. Note same numbering system as in Figure 4.7.

Number of Successful Pick-ups Per Location						Percent Success Rate per Location for 25 trials					
Location	1	2	3	4	5	Location	1	2	3	4	5
1	17±2.4	25±0.0	20±2.0	25±0.0	19±2.2	1	68±9	100±0	80±8	100±0	76±9
2	25±0.0	22±1.7	25±0.0	22±1.7	24±1.0	2	100±0	88±6	100±0	88±6	96±4
3	22±1.7	24±1.0	24±1.0	25±0.0	24±1.0	3	88±6	96±4	96±4	100±0	96±4
4	25±0.0	18±2.3	25±0.0	21±1.9	24±1.0	4	100±0	72±9	100±0	84±7	96±4
5	20±2.0	25±0.0	24±1.0	25±0.0	20±2.0	5	80±8	100±0	96±4	100±0	80±8

Again, these statistics were based on the Binomial Distribution. It can be seen that the lowest success rate was 67%, while the highest was 100% for the 25 trials. The mean and standard deviation amongst all the trials was calculated, with a mean of 22.80, standard deviation of 2.52, and an average success rate of 90.83%. Again, what is more important to note, however, is the success rate of water droplet formation. Although pickup was not 100% for each channel and avoided pickup was not 100% for every channel, the water droplet growth for the checkerboard pattern was seen for every trial,

giving a droplet generation success rate of 100% for every channel. Any unwanted pick up was due to walking of the droplets or misalignment.

4.4 Superhydrophobic Coating Picking up All Spheres

In many cases, when the water droplets were growing from the channels, the water droplets did not stay pinned to the holes, and instead "walked". This means that the water droplets no longer kept a spherical shape and bled out onto the circuit board. This could cause the picking up of unwanted spheres or for the inability to pick up desired spheres since the droplets where no longer in their designated location. Therefore, a superhydrophobic coating was applied to the circuit board using vapor deposition by Integrated Surface Technologies. The goal was to ensure pinning the droplets at the holes to increase reliability in the picking process. This coating, called "Repellix" guaranteed 25-85 times more repellant to water than uncoated surfaces. The coating was 10-100nm thick and was applied using vapor deposition [25]. The effects of this coating can be seen in Figure 4.11.

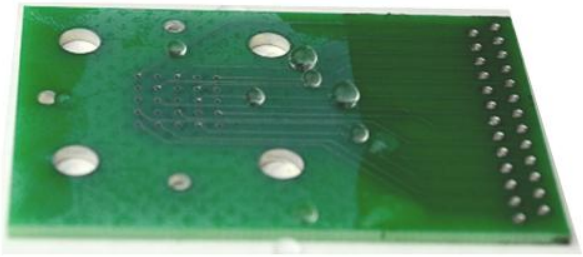

Figure 4.11: Superhydrophobic coating with water droplets on surface. Note droplets are almost perfectly spherical. The coating ends where the right-most droplets are positioned.

4.4.1 Picking up All Spheres

Using this new coating, the trials were repeated and it was found that the average pick-up rate for the 25 trials was 23.72 spheres per trial with a standard deviation of 1.6 spheres. The average success rate was 94.9%. The average pick up without the coating was 22.72, with a standard deviation of 1.5 spheres, and an average success rate of 90.9%. While all but the standard deviation made a substantial improvement, it is important to note that for the superhydrophobic trials, most of the error was on the left row, particularly the top left channel. This channel had 7 failed pick-ups, which is much larger than the average. Water was being filtered through the channel, and droplets were being formed. However, the sphere was not being picked up. Just like the uncoated trials, the water droplet formation had a 100% success rate. Therefore, this leads to suggest that there was error due to alignment, and was not due to the electroosmosis device. See Figures 4.12-4.13 and Table 4.5 for data.

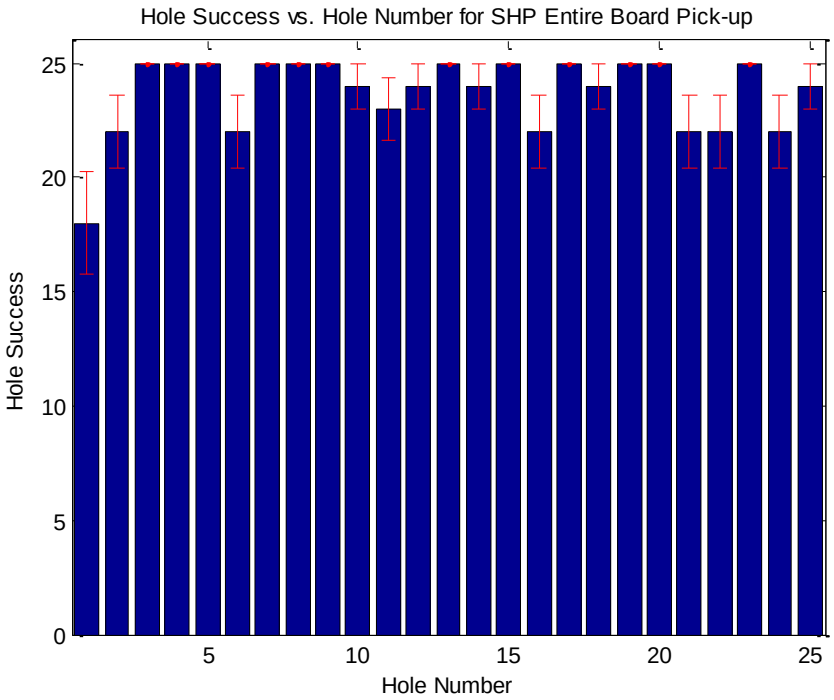

Figure 4.12: Hole Success vs. Hole Number for Super-Hydrophobic Coating Entire Board Pick-up. Note same numbering system is used as in Figure 4.4.

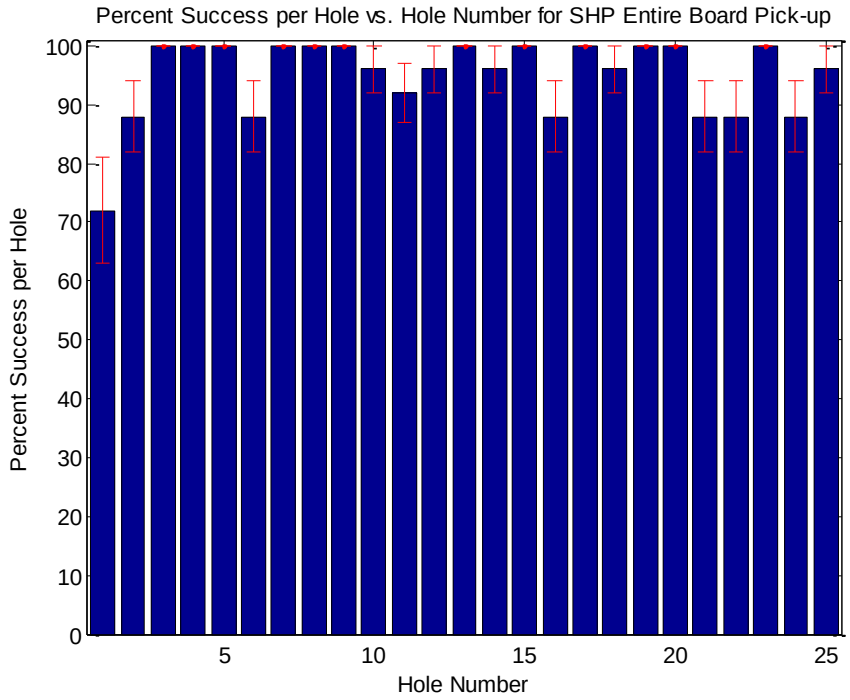

Figure 4.13: Percent Success vs. Hole Number for Super-Hydrophobic Coating Entire Board Pick-up. Note same numbering system is used as in Figure 4.4.

Table 4.5: Collected data for 25 trials with standard deviations. Note same numbering system as in Figure 4.7.

Number of Successful Pick-ups Per Location						Percent Success Rate per Location for 25 trials					
Location	1	2	3	4	5	Location	1	2	3	4	5
1	18±2.2	22±1.6	25±0.0	25±0.0	25±0.0	1	72±9	88±6	100±0	100±0	100±0
2	22±1.6	25±0.0	25±0.0	25±0.0	24±1.0	2	88±6	100±0	100±0	100±0	96±4
3	23±1.4	24±1.0	25±0.0	24±1.0	25±0.0	3	92±5	96±4	100±0	96±4	100±0
4	22±1.6	25±0.0	24±1.0	25±0.0	25±0.0	4	88±6	100±0	96±4	100±0	100±0
5	22±1.6	22±1.6	25±0.0	22±1.6	24±1.0	5	88±6	88±6	100±0	88±6	96±4

4.4.1 Picking up Checkerboard Pattern

Using this new coating, the new average pick-up rate for the 25 trials was 24.52 spheres per trial with a standard deviation of 1.6 spheres. The average success rate was 98.1%. The average pick up without the coating was 22.8, with a standard deviation of 2.5 spheres, and an average success rate of 90.8%. In this case, the superhydrophobic coating improved all general success metrics. However, again the left, top-most channel skewed the data, having 8 failed pick-ups, which is much larger than the average. Water was being filtered through the channel, and droplets were being formed. Just like the uncoated trials, the water droplet formation had a 100% success rate. Therefore, this leads to suggest that there was error due to alignment, and not due to the electroosmosis device. This argument is even stronger, given that this hole also was an issue in the previous trials for picking up all spheres. See Figures 4.14-4.15 and Table 4.6 for data.

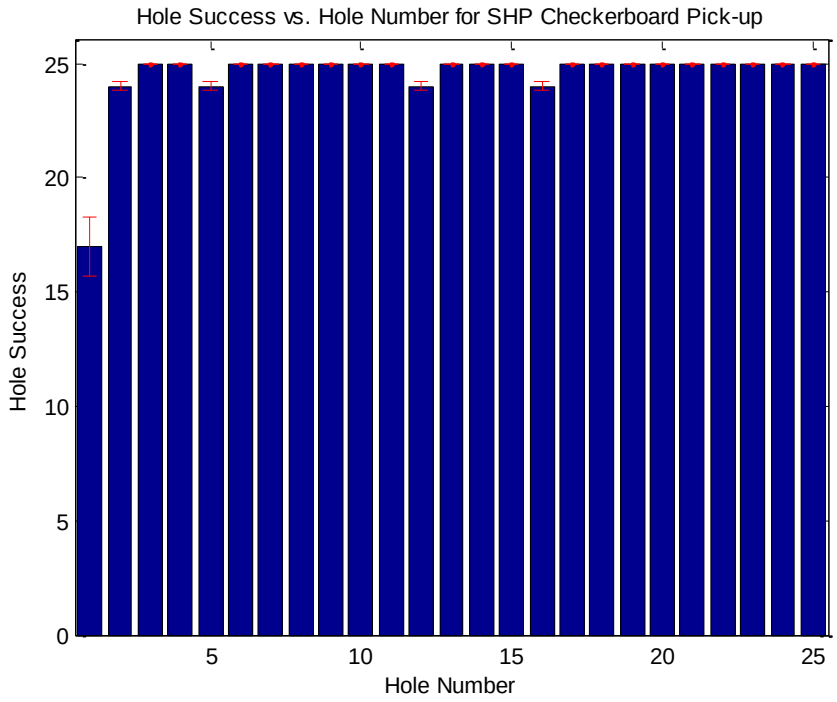

Figure 4.14: Hole Success vs. Hole Number for Super-Hydrophobic Coating for Checkerboard Pattern. Note same numbering system is used as in Figure 4.4.

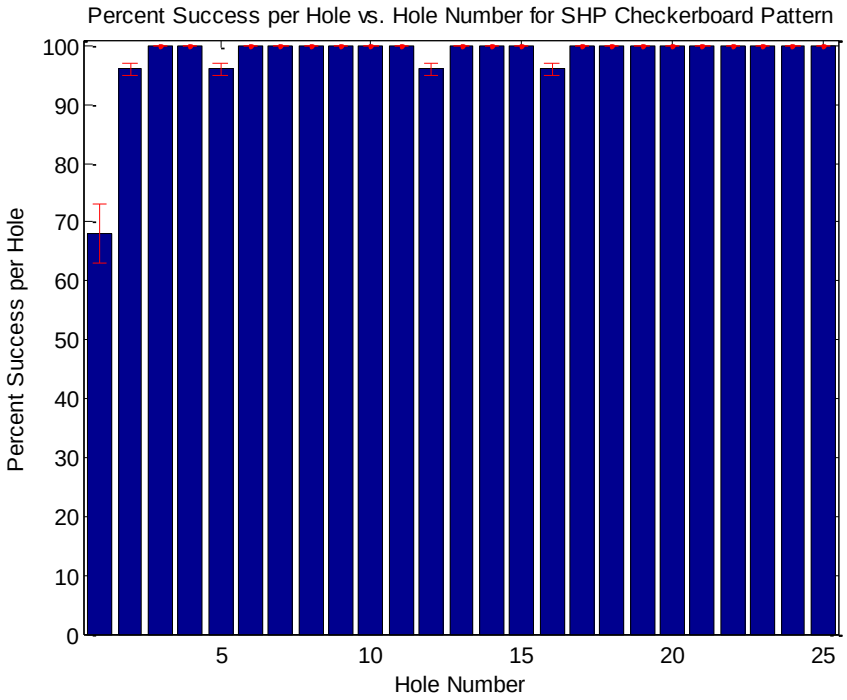

Figure 4.15: Percent Success vs. Hole Number for Super-Hydrophobic Coating for Checkerboard Pattern. Note same numbering system is used as in Figure 4.4.

Table 4.6: Collected data for 25 trials with standard deviations. Note same numbering system as in Figure 4.7.

Number of Successful Pick-ups Per Location						Percent Success Rate per Location for 25 trials					
Location	1	2	3	4	5	Location	1	2	3	4	5
1	17±1	24±0.2	25±0	25±0	24±0.2	1	68±5	96±1	100±0	100±0	96±1
2	25±0	25±0	25±0	25±0	25±0	2	100±0	100±0	100±0	100±0	100±0
3	25±0	24±0.2	25±0	25±0	25±0	3	100±0	96±1	100±0	100±0	100±0
4	24±0.2	25±0	25±0	25±0	25±0	4	96±1	100±0	100±0	100±0	100±0
5	25±0	25±0	25±0	25±0	25±0	5	100±0	100±0	100±0	100±0	100±0

Based on this data, there is one location (location 1, 1 in Table 4.6) that has a much higher failure rate than the other channels. Assuming this is an anomaly, the average, percent average, and standard deviation were calculated leaving this point out for the SHP checkerboard pattern. The values for these three statistics are 24.83, 99.3%, and 0.381 respectively. These values are much more desirable than those including the inconsistent channel.

4.5 Other Configurations

In order to test the reliability of the PICEM, other configurations besides the all-sphere and checkerboard pattern were tested.

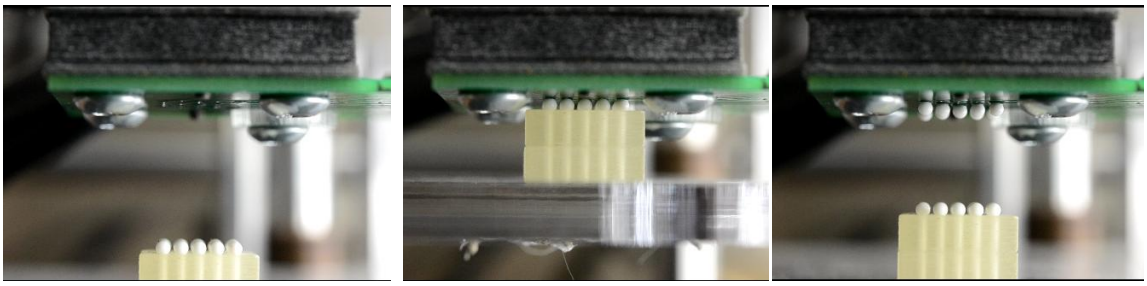

(A) (B) (C)

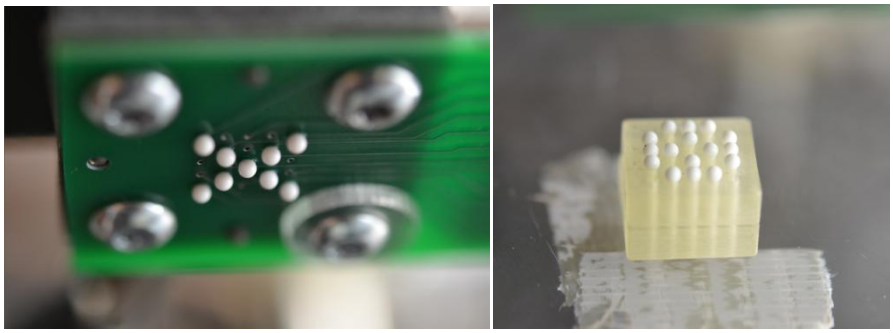

(D) (E)

Figure 4.16: Picking and placing of "X" shape. Figures A-C show the droplets formed, the Z-platform moving up to pick the selected spheres, and the platform recessing. Figures D and C show views after the process was completed.

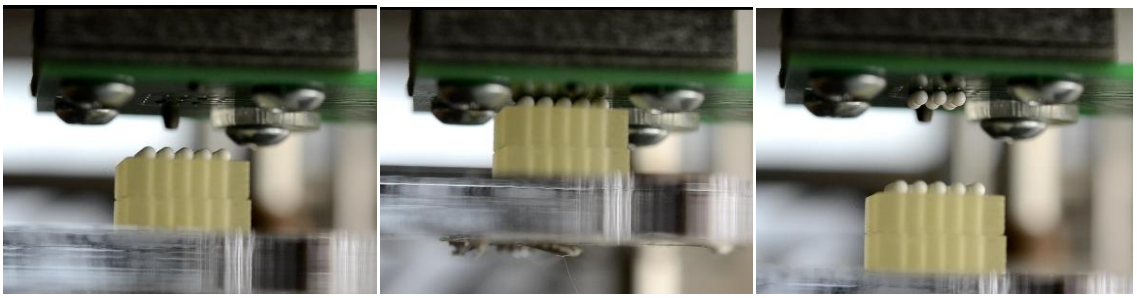

(A) (B) (C)

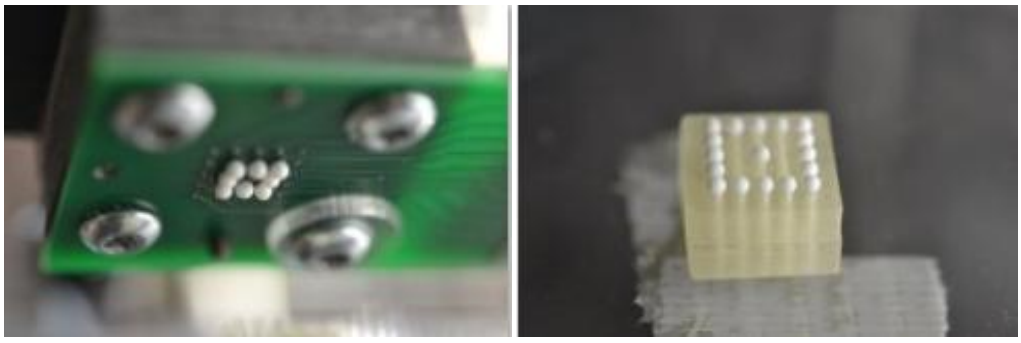

(D) (E)

Figure 4.17: Picking and placing of square shape. Figures A-C show the droplets formed, the Z-platform moving up to pick the selected spheres, and the platform recessing. Figures D and C show views after the process was completed.

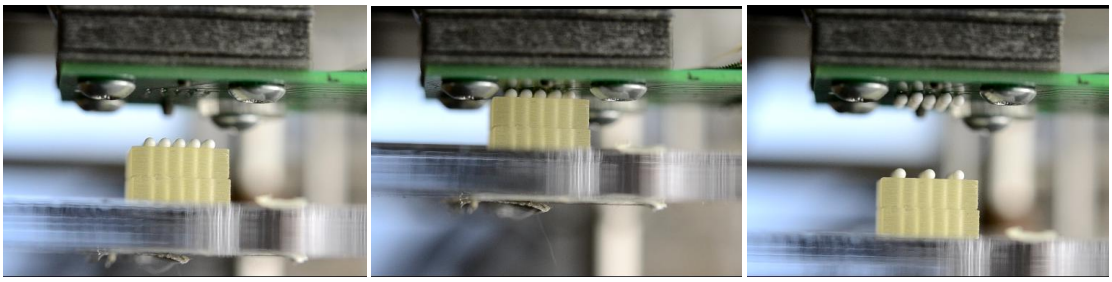

(A) (B) (C)

(D) (E)

Figure 4.18: Picking and placing of a "#" or "pound" shape. Figures A-C show the droplets formed, the Z-platform moving up to pick the selected spheres, and the platform recessing. Figures D and C show views after the process was completed.

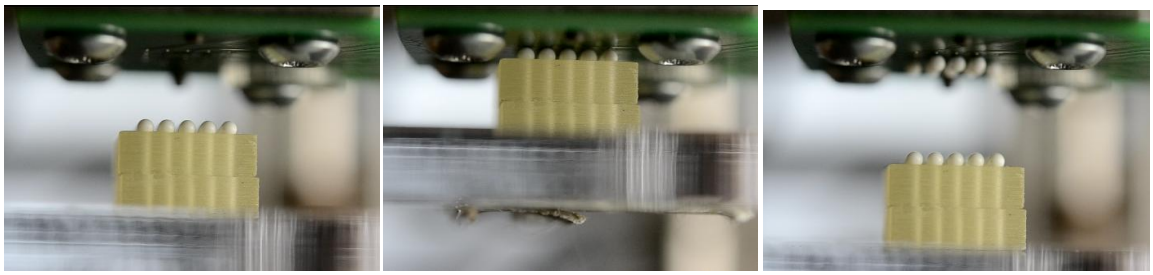

(A) (B) (C)

(D) (E)

Figure 4.19: Picking and placing of a “top hat” shape. Figures A-C show the droplets formed, the Z-platform moving up to pick the selected spheres, and the platform recessing. Figures D and C show views after the process was completed.

4.6 Picking up Other Objects

In order the test the versatility of the PICEM device, it was necessary to pick up objects other than those of just spherical configurations. In actual use, the size, weight, and geometry of the objects being moved will vary. Therefore three tests were performed to evaluate this versatility: picking up 3D printed rotation and flip invariant interlocking tiles (3x3x1 mm), 1.5 mm stainless steel spheres (0.1014 grams), and custom made circuit board tiles (3x3x1 mm). Selective control was used in that only certain channels were activated to pick up chosen objects. See the Figure 4.20.

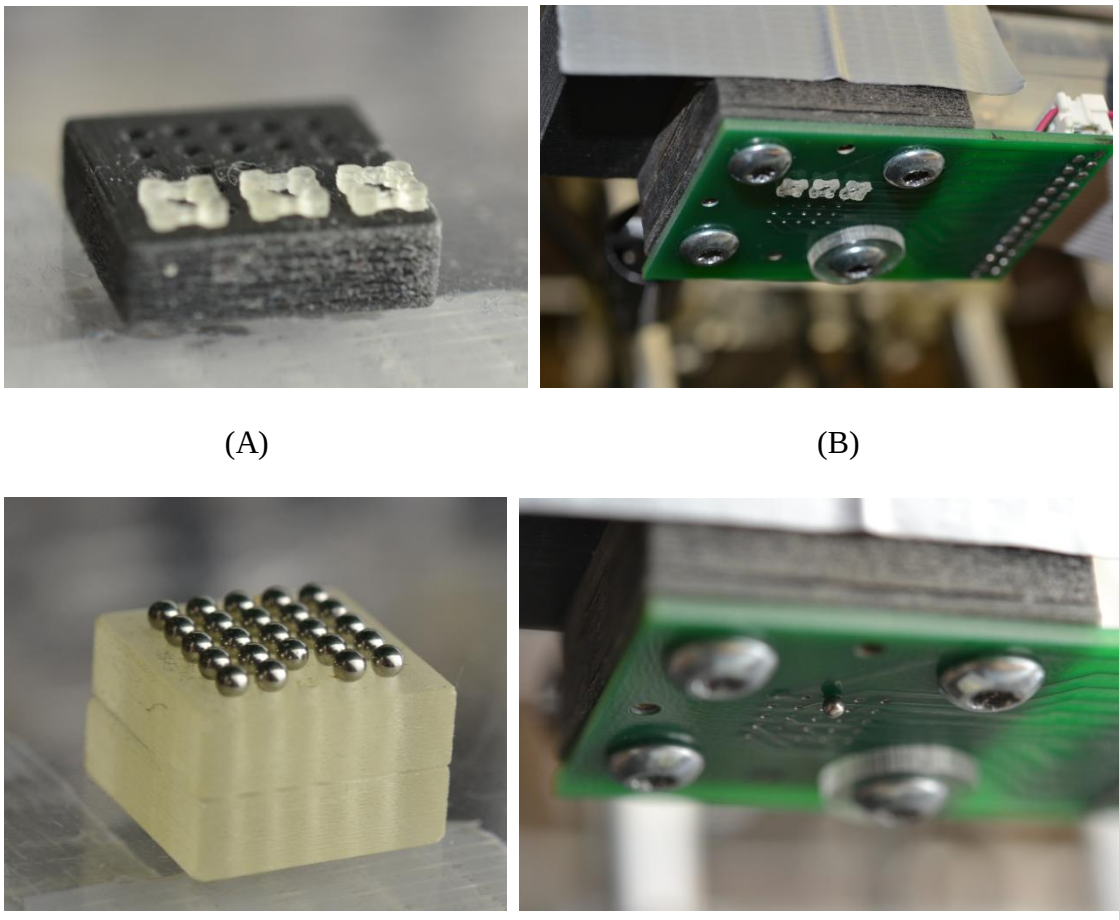

(A) (B)

(C) (D)

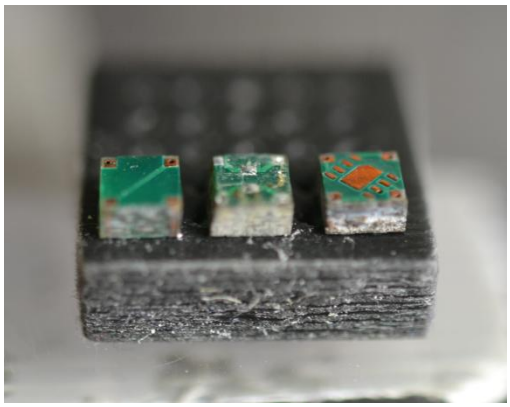

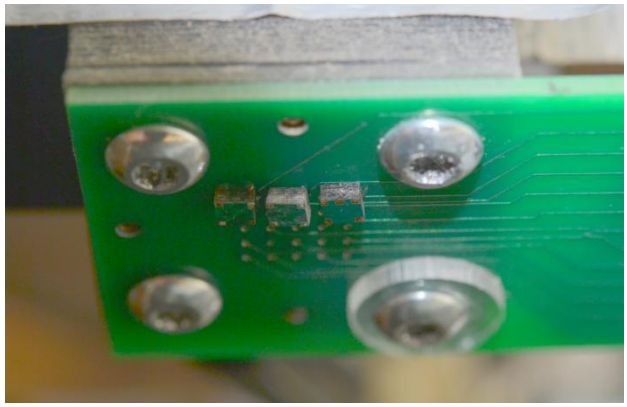

(E) (F)

Figure 4:20: Picking up various objects.

In images (A) and (B) the 3D FullCure720 tiles were picked and placed, activating only three channels. A SolidWorks image of these tiles can be seen in image 4.21. In (C) and (D) a single stainless steel sphere was picked, and only the center, front channel was activated. In (E) and (F) circuit board tiles were picked using only three activated channels. In doing these tests, it was possible to show that the PICEM can pick up a variety of different types of objects with varying sizes, geometries, and weights.

4.7 Placing Spheres

While picking of the spheres was studied extensively in this research, it was necessary to do a proof of concept to observe the PICEM's ability to place spheres. When a positive voltage is applied, water droplets are able to form in and on the selected printed circuit board channels. When the voltages are set back to zero, or turned off, the droplets stay as is until evaporation starts to have effects on the system. If the voltage is reversed,

applying a negative voltage across the frit, the water motion is reversed as well, and the droplets are withdrawn back into the reservoir. Therefore, in order to place these spheres, it is possible to use this negative applied voltage to remove the water droplets, removing the main force that is holding the spheres to the circuit board. However, there are other physics involved in this scenario, especially when the scale decreases. Electrostatic forces and van der Waals forces cause the sphere or object to stay connected to the printed circuit board, despite there being no surface tension forces keeping it in place. However, the final application of this device is for use in picking and placing layers of force fit tiles. Therefore, the printed circuit board will act as a forcing platform to push the tiles into their interlocking configurations (example Figure 4.21).

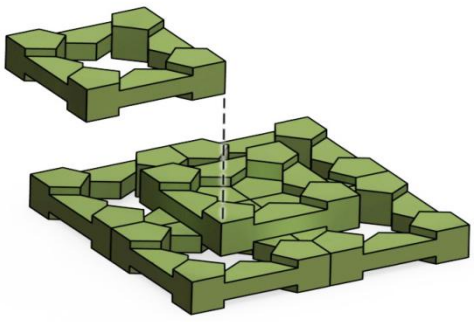

Figure 4.21: SolidWorks image of potential interlocking tiles (image provided by Dr. Jonathon Hiller).

Therefore, since the interlocking force fit will be greater than that of the other forces holding the object to the printed circuit board, these other forces should not be an issue. In order to simulate this placing operation with a larger platform connecting force than those interacting between the sphere and the printed circuit board, adhesive foam mats

were used as the placing platform. In final configurations this would be a base plate specially designed to interlock the objects (example Figure 4.22).

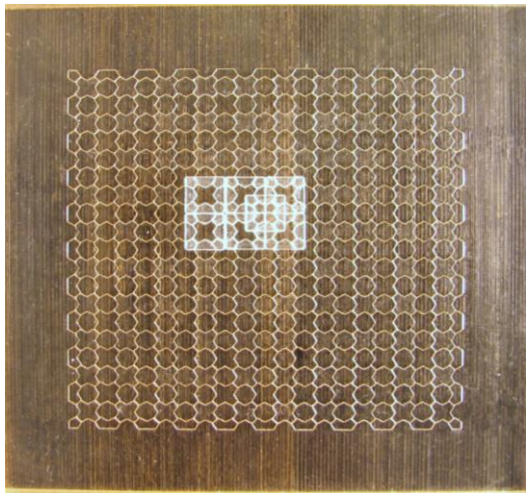

Figure 4.22: 5mm square tiles placed on locking base plate grid (all parts 3D printed FullCure720).

The video stills of the simulated locking platform placing test can be seen in Figure 4.23.

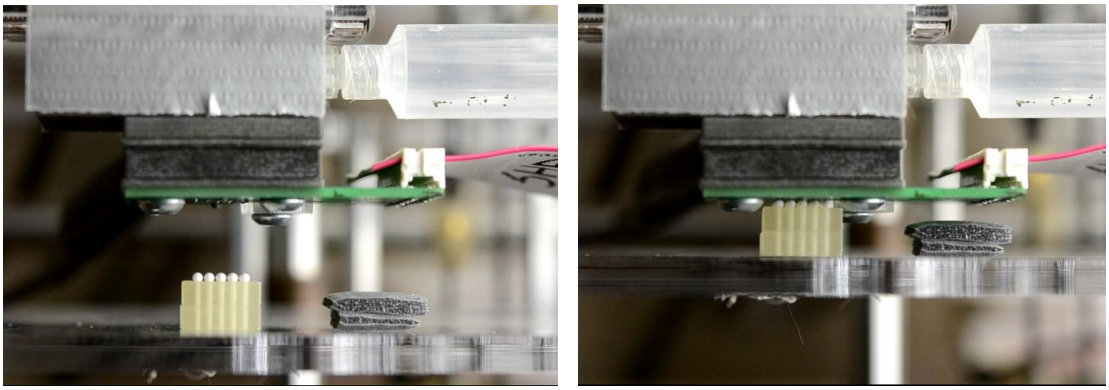

(A) (B)

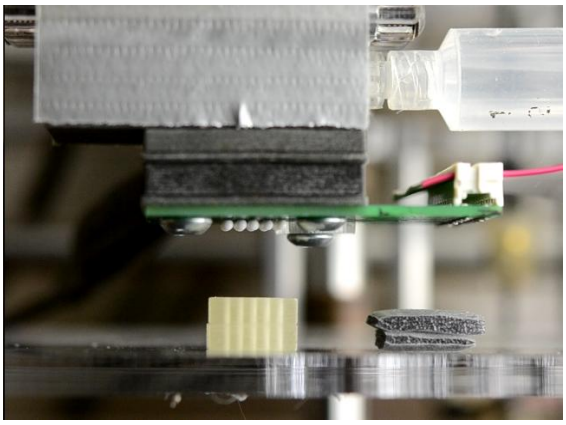

(C)

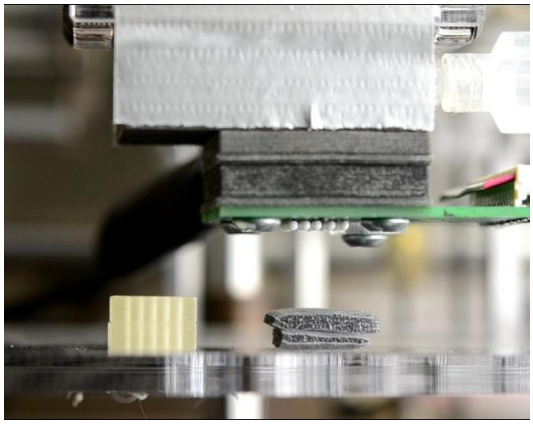

(D)

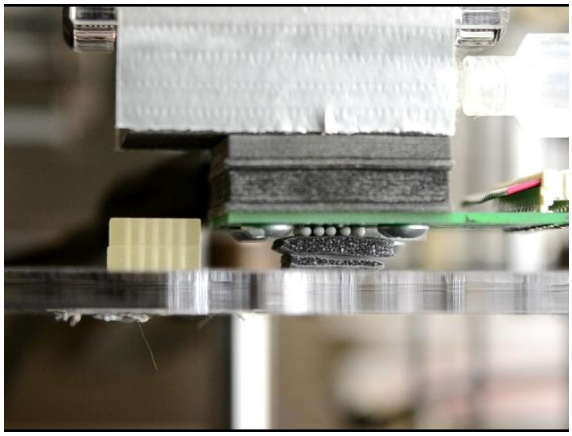

(E)

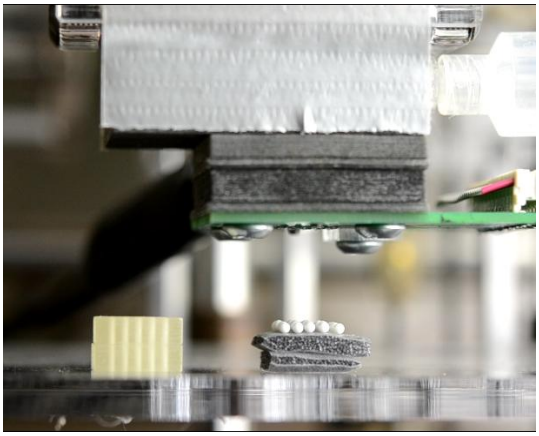

(F)

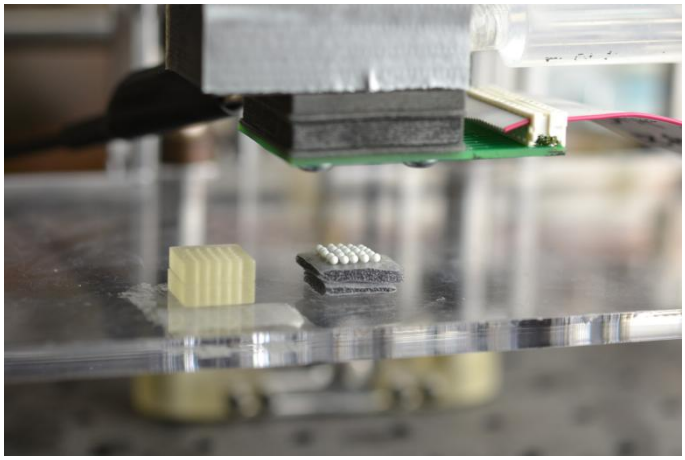

(G)

Figure 4.23: (A) All droplets are activated with 15 V. (B) Z-platform is raised to pick spheres. (C) Platform is lowered, and all spheres were picked. (D) Voltage is turned off. Device moves in the x-direction to align with placing platform. (E) Voltage is turned to -15 V. Z-platform is raised making contact with spheres. (F) Z-platform is lowered, leaving behind all spheres. (G) Wide view of final configuration with all spheres picked from sphere platform and placed onto the final location.

CHAPTER 5

Analytical Solutions vs. Experimental Results

5.1 Manufacturer's Specifications of Borosilicate Glass Frit

While the 55 mm diameter Ultra Fine (UF) borosilicate glass frit was purchased from Ace Glass, the parts were actually made at a company called ROBU, in Hattert, Germany. All specifications of the frit used for testing were obtained from technical detail documents specific to this part through ROBU. Based on ASTM standards, UF for these frits requires a pore size of diameter 0.9-1.4 microns, classifying it a POR5 frit [27]. Based on this class, the pore size distribution, per manufacturer's specifications can be seen in Figure 5.1.

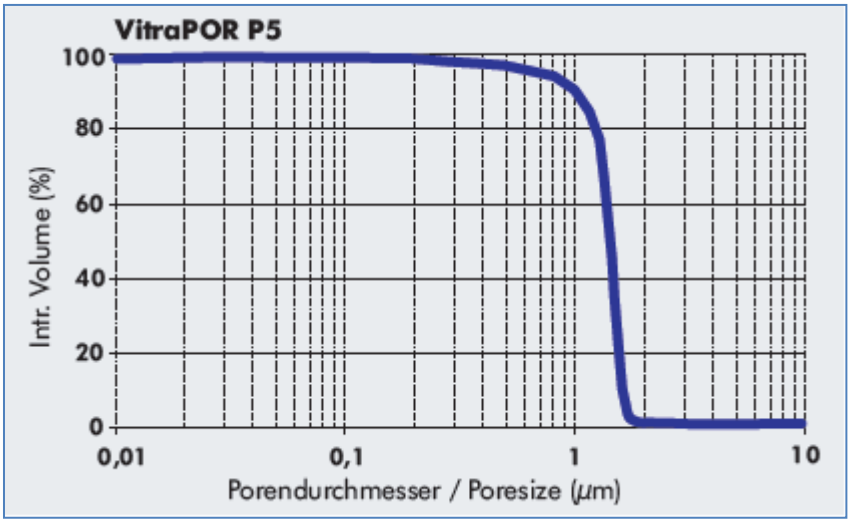

Figure 5.1: Pore size distribution for P5 frit class [26].

This plot shows that about 90% of the internal pore volume has a pore throat size of at least 0.9 microns, and about 75% of the internal pore volume has a pore throat size of at least 1.4 microns. This data is consistent with the pore class of POR5 frits having a pore size of between 0.9-1.4 microns, with an average diameter of 1.15 microns. It is important to note that these frits are made by sintering borosilicate glass beads, then

compressing the matrix into the proper frit dimensions. This means that the original spheres may no longer have a circular contour, and the pore may not be circular.

Furthermore, the porosity was defined as approximately 48%, as read from the ROBU Pore Volumes and Inner Surface table (Figure 5.2).

Porosity Classification	Pore Volume (% void)	Inner Surface (BET)
Por. 00	~ 30%	~ 0,015 m²/gr
Por. 0	~ 33%	~ 0,020 m²/gr
Por. 1	~ 34%	~ 0,085 m²/gr
Por. 2	~ 36%	~ 0,130 m²/gr
Por. 3	~ 41%	~ 0,350 m²/gr
Por. 4 / Por. M	~ 42%	~ 0,500 m²/gr
Por. F	~ 45%	~ 1,200 m²/gr
Por. 5 / Por. UF	~ 48%	~ 1,750 m²/gr

Figure 5.2: Pore volume and Inner Surface BET for different pore classifications [27].

Finally, the permeability was determined by using the Flow rate/Pressure Calculation plot for water on a filtered disk of 30mm with class POR5 (Figure 5.3).

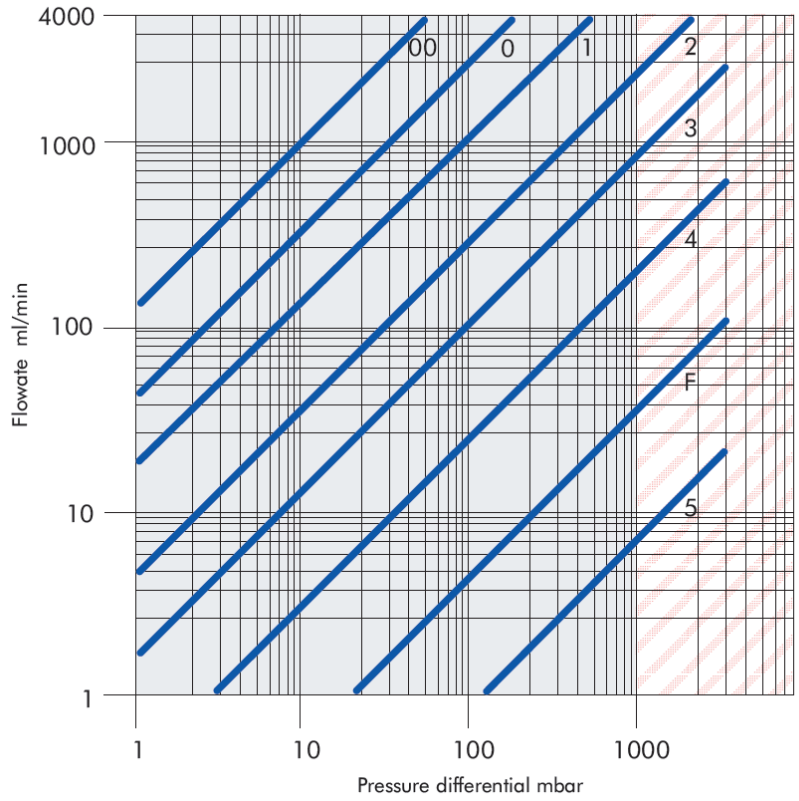

Figure 5.3: Flow rate vs. Pressure differential for 30 mm glass frit for various pore classes [28].

The classification 5 is the line that dictates the flow rate/pressure differential relationship. Using Darcy's Law, $\kappa = \frac{Q\mu L}{A\Delta P}$, and the point 1000 mbar for POR5 class, the flow rate was read to be 6 ml/min. By plugging these numbers into Darcy's equation for permeability, with μ as the viscosity of water, L as the height of the frit (4.76 mm), and A as the area based on the 30 mm frit size. Based on this calculation, the manufacturer's permeability, κ, is found to be 4.95e-15 m^2.

5.2 Outsourced Testing

In order to properly characterize the frit used in these experiments, the frits ordered were sent to Porous Materials Incorporated to compare a number of variables supplied by the manufacturer. A test that was outsourced was the T506 Liquid Permeability test (Figure 5.4). This test uses various compression based pressure steps to determine the fluid output of the device, and thus the permeability. The permeability as a function of pressure can be seen in Tables 5.1-5.3 for three test samples. Note that under atmospheric pressure there is some flow for sample 3, which should not be the case since this would suggest flow exists without a pressure gradient. This could be due to initial improper sealing, as hypothesized by the PMI technicians. Furthermore, all pressures measured in the table include a 0.1 head pressure for water on top of the sample. For raw data, see Appendix B.

Figure 5.4: T506 Liquid Permeability tester [25]. Image provided by PMI (Evan Sorel).

Table 5.1: Permeability determined from LP test based on various pressure steps for Sample 1.

Sample 1		
Pressure (psi)	Flow rate (g/min)	Permeability (m^2)
14.5	0	0
29.81	0.16878	2.29576E-15
39.69	0.3673	3.75239E-15
49.35	0.66635	5.47498E-15

Table 5.2: Permeability determined from LP test based on various pressure steps for Sample 2.

Sample 2		
Pressure (psi)	Flow rate (g/min)	Permeability (m^2)
29.61	0	0
39.81	0.1333	1.90936E-15
49.66	0.2675	3.07161E-15
59.94	0.441	4.19537E-15
69.84	0.7191	5.87129E-15
80.01	0.8455	6.02585E-15

Table 5.3: Permeability determined from LP test based on various pressure steps for Sample 3.

Sample 3		
Pressure (psi)	Flow Rate (g/min)	Permeability (m^2)
14.5	0.0693	6.96998E-16
25.86	0.772	4.35367E-15
35.71	1.8964	7.74474E-15
45.77	2.1544	6.86455E-15
55.46	2.4352	6.40356E-15
65.85	2.9138	6.45313E-15

As these tables show, the permeability and flow rate increase as pressure increases. This data is consistent with theory, in the fact that as a higher pressure is applied, smaller pores are able to allow water flow. The numbers from each chart that pertain to the actual permeability of the porous matrix for use in Darcy's equation are those at the lowest pressures, above atmospheric. The reason these numbers are used is because the

device operates at atmospheric pressure, but it takes a certain amount of added pressure to begin flow through the device and to register an actual permeability. Therefore, the permeabilities corresponding to pressures 29.81, 39.81, and 25.86 from the three tables are those of most interest. The average permeability for these pressures is 2.35e-15 m^2.

A second test was performed on sample three, a Liquid-Liquid Permeability test, which first soaks the frit in a material called silwick, removing air from inside the pores. From there, water is driven through the frit under increasing pressure. The output of this test is a permeability chart which shows flow rate vs. time (Figure 5.5).

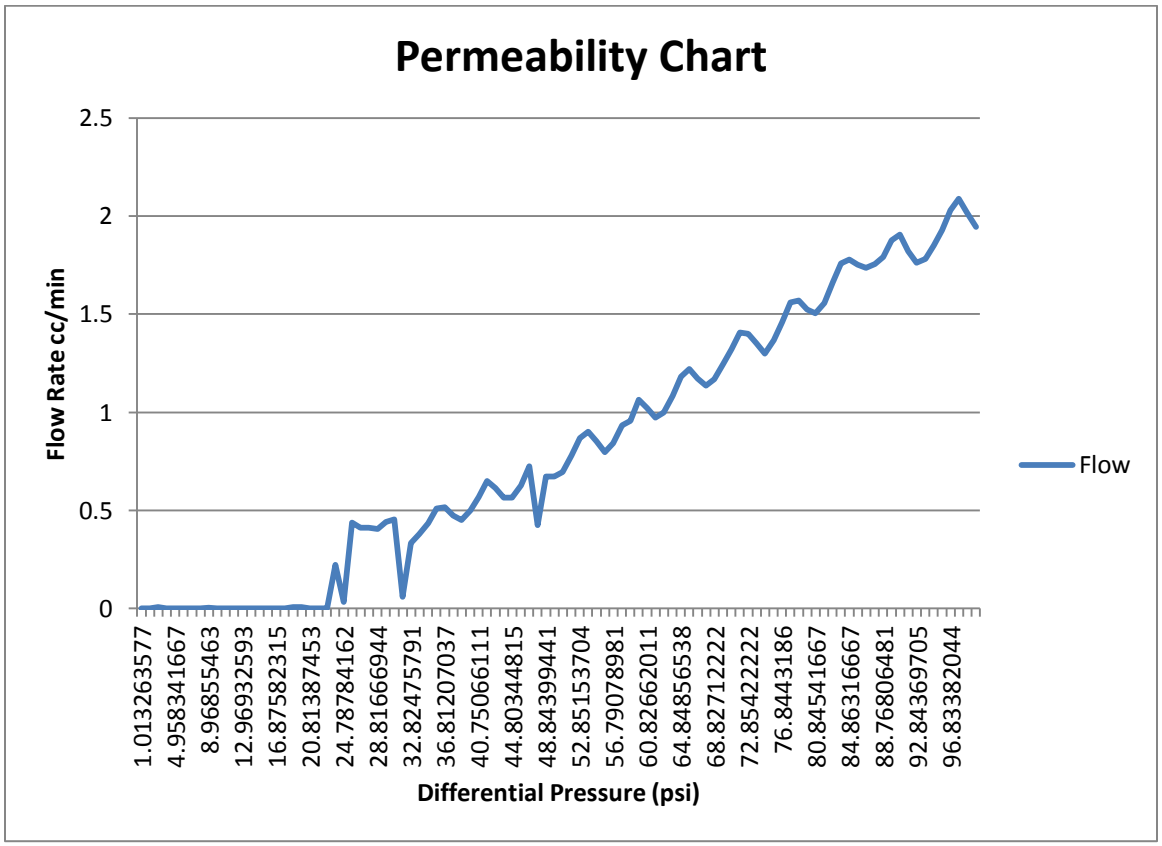

Figure 5.5: Permeability Chart for Sample Three.

From this information, the minimum capillary pressure can be determined (the pressure needed to begin the flow of water through the frit), by looking at the point where flow

begins. This point is approximately 23 psi, and is the minimum capillary pressure present for the pore distribution.

5.3 Microscope Pore Evaluation and Capillary Pressure Testing

In order to confirm the pore diameter of the frits, two 1cm square frits (one cracked at the edge) and three corresponding fractured shards, were observed under a microscope at 80x magnification.

Figure 5.6: Image of Used Frit under 80x magnification.

Figure 5.7: Pores used in determining diameter (black), other noticeable pores (red).

What is important to note is that at different focal lengths it is possible to see different pores of the frit due to the uneven surface. Two pores from each image were used in order to keep consistency in the number of pores taken from each sample. Based on the calibration (the image height displayed represents 50 microns), the diameters were measured and can be seen in Table 10.

Table 5.4: Measured diameters and averages for various frits and shards. The first listed diameter is the width; the second is the height of the pore.

Name	diameter (μm)	diameter (μm)	Average (μm)	diameter (μm)	diameter (μm)	Average (μm)
New Frit 1	4.110	5.479	4.795	3.425	4.795	4.110
New Frit 2	4.795	5.479	5.137	4.110	4.795	4.452
Shard 1	4.110	4.795	4.452	2.740	2.740	2.740
Shard 1b	2.740	2.740	2.740	2.055	2.055	2.055
Shard 2	6.164	8.219	7.192	2.740	2.740	2.740
Shard 2b	5.479	5.479	5.479	1.370	1.370	1.370
Shard 3	4.110	5.479	4.795	5.479	4.110	4.795
Shard 3b	2.740	2.740	2.740	5.479	5.479	5.479
Used Frit 1	4.795	6.164	5.479	2.740	2.740	2.740
Used Frit 2	5.479	5.479	5.479	4.110	4.795	4.452
		Average:	4.829		Average:	3.493
		Ave Rad (μm):	2.414		Ave Rad (μm):	1.747
					Total Rad Ave (μm):	2.080

From this Table, the average radius of the pores is 2.080 microns. Other images of frits under the microscope are available in Appendix C.

Furthermore, to confirm the PMI data, a capillary pressure test was performed in order to determine the amount of pressure necessary to begin flow through the device. The test setup mounted the PICEM vertically where the syringe was hung from a ring stand. An acrylic plate stabilized by two poles, but allowed to slide, was placed atop of the syringe end to provide a larger base for adding masses. Masses were added incrementally on the device until water began to flow from the PICEM. This critical mass was 10.02lbs. The surface area of the syringe base was $0.371in^2$, giving a pressure of approximately 26.95 psi.

5.4 Velocity Testing

In order to determine the velocity of the water droplets coming out of the channel experimentally, individual channels were activated with a set voltage (15 V) and image

acquisition was performed with MotionPro video analysis software. The size of the water droplet was measured over time by an in house MATLAB routine that combines image analysis with a volume calculation that uses a Riemann sum of frustum image elements. The droplets were calibrated using 1.5mm spheres placed on the channels. The volume vs. time was plotted, and the velocity was calculated by dividing the flow rate (volume/time) by the area through which this flow travels, $\pi*(0.508\ \text{mm})^2$. Video stills are available in Figure 5.8. The factor that converts from pixels to a physical length scale is 0.012 mm/pixel.

(A)

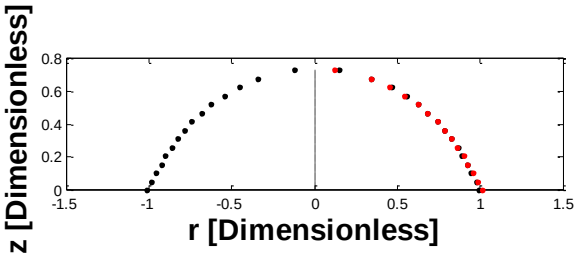

(B)

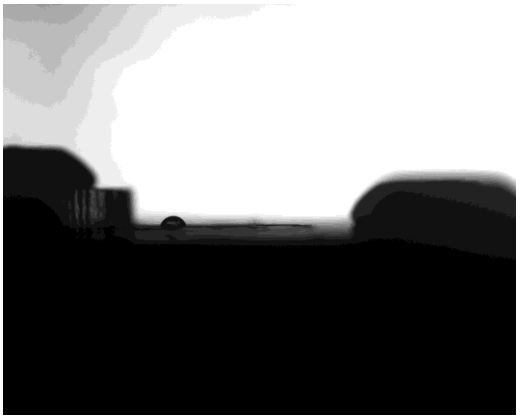

(C)

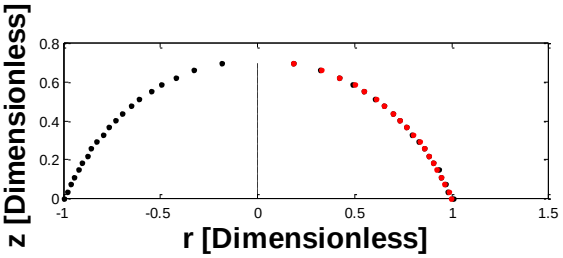

(D)

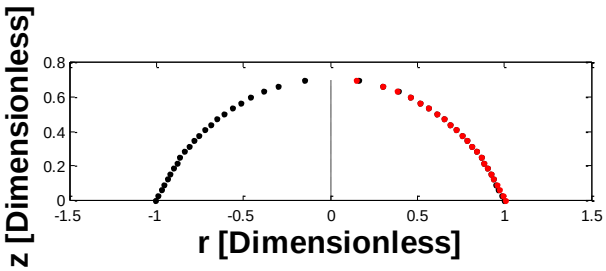

(E) (F)

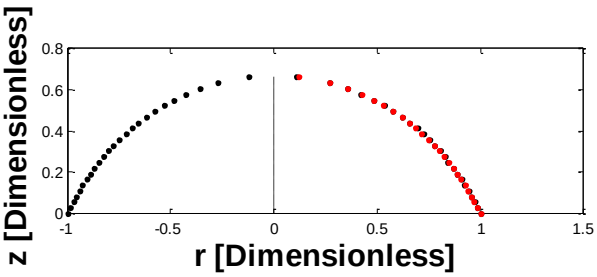

(G) (H)

Figure 5.8: Images on left show actual droplet growth, while images on right show the MotionPro outline growth. The time steps for the four sets of images are 8, 16, 24 and 32 seconds.

Table 5.5: Velocity data from video trials. Location refers to row_column.

Velocity Analysis		
Location	**Slope (mm^3/s)**	**Velocity (mm/s)**
5_1	0.05	0.246690655
5_2	0.0391	0.192912092
5_3	0.0351	0.17317684
4_4	0.0318	0.156895257
4_2	0.0302	0.149001156
3_3	0.0265	0.130746047
3_1	0.0259	0.127785759
2_2	0.0248	0.122358565
2_1	0.023	0.113477701
1_4	0.0246	0.121371802
1_3	0.0328	0.16182907
1_1	0.0198	0.097689499
1_4	0.0171	0.084368204
1_4	0.0136	0.067099858

From this data, it can be seen that there may exhibit different velocities at different locations. Note that location 1_4 was tested multiple times and showed different velocities for different trials. This could have much to do with the pore distribution of the frit, or channel alignment issues inside of the device. However, these velocities are all relatively close in scale. The average velocity for all locations is 0.136 ± 0.0242mm/s (based on a 95% confidence interval).

5.5 Analytical Solution

Beyond just looking at the repeatability of this device, it is necessary to look at the theoretical and experimental flow rates and velocity to determine if there are any factors that could affect the reliability and consistency of the device. In order to determine the velocity or fluid flow through the pores at the base of the circuit board, it was necessary to determine whether or not a bulk flow model could be used. In order to do this the

Debye length was calculated and compared to the diameter of the pore. The Debye length was calculated using the equation: $\lambda_D = \sqrt{\frac{\varepsilon_w RT}{F^2 \sum_{i=0}^{N} c_i {z_i}^2}}$=971 nm (ε=permittivity of water, R=universal gas constant, T=temperature, F=Faraday's constant, c_i=molar concentration of species i, and z_i=valence number (1) of species i normalized by the elementary charge) while the diameter of the pore was found to be 1.15e-6 m [29]. Given that the ratio (d^*) of pore diameter to Debye layer (1.18) was greater than 1, a bulk flow model cannot be used. This is an upper bound on the double layer thickness. In practice, the double layer is likely to be thinner because there are likely to be impurities in the water from contact with the frit and exposure to the air allowing for dissolution of gases (i.e., CO_2).

The net axial velocity of fluid through a channel as a result of an externally applied electric field is a superposition of the Helmholtz-Smoluchowski electroosmotic velocity and Darcy's law modified with the appropriate coefficients to account for finite thickness of the double layer [29].

$$\bar{v}_{net} = \bar{v}_{eo} - \bar{v}_{Darcy} = c_{11} \frac{\varepsilon_{w/f} \psi_s \bar{E}_{ext}}{\mu} - c_{12} \frac{\kappa \bar{\nabla} \mathrm{P}}{\mu} \quad (1)$$

Where $\varepsilon_{w/f}$=reduced permittivity of water due to ϕ, μ=dynamic viscosity, E_{ext}=applied electric field, grad P=pressure gradient, ψ_s=surface potential. While this equation is a vector, the velocity of most interest is that exiting the channel, which will also be in the downward y direction. Assuming that the double layer thickness does not affect the viscosity, the functional dependence of the second term on the right hand side remains the same as that for thin double layers (i.e. c_{12}=1). As for the first term, $c_{11} \neq 1$, since the double layer is finite. The surface potential, ψ_s, for a borosilicate glass frit in contact with

distilled water is typically around -100 mV [20], which does not justify the use of the Debye-Huckel approximation (must be less than 25mV) in deriving the electroosmotic component of the velocity. To account for this non-linearity of bulk flow and high surface potential, $c_{11} \approx 1/(1+\exp[-\alpha(logd^* - logd_0{}^*)]$ is incorporated ($\alpha \approx -0.15|\psi_0| + 3.5$, $d_0{}^* \cong -0.01{\psi_0{}^*}^2 - 0.1|\psi_0{}^*| + 2$) [31]. The permeability (which is assumed to be isotropic) can be estimated analytically for a bed of packed spheres by relating it to the permeability of a series of parallel straight cylinders [19]. Since permeability of spherical packed bed of spheres can be derived analytically, using this derivation, it is possible to estimate the permeability of a porous media using manufacturer's specifications. The resulting equation is:

$$\kappa = \frac{\phi R^2}{24} = 6.613e-15m^2 \quad (2)$$

In this case, ϕ is the porosity based on manufacturer's specifications, 0.48, and the R is the manufacturer's radius. This theory operates by taking the pore size of the frit and assuming it is approximately equivalent to the cylindrical diameter model from which this equation was derived. It is important to note, however, that this R is assumed to be the radius of a cylindrical channel, which can be equated to the radius of a sphere in a packed bed. As mentioned before, due to the compression process in the frit manufacturing, the glass beads are no longer perfectly spherical, which could alter the validity of applying this theoretical model.

Since the electric field is equivalent amongst all channels if all channels are activated, the velocity will also be the same, theoretically, as well. The most simplistic measure of the electric field could be thought of as E=V/L, where L is a constant value of the frit thickness (4.76 mm), and V is the voltage applied in the experiments (15 V). This

gives an electric field of approximately 3138 N/C. However, the experimental set-up uses a large plate electrode on the top and single rings of Sn/Pb on a printed circuit board at the bottom. Therefore, if a single droplet is activated, it is still influenced by the electric field produced by the other locations on the electrode besides the one directly below the top activated channel, which will be treated as a point since its area in relation to the entire electrode is much smaller. Therefore, it is necessary to look at the contribution of the electric field by the rest of the electrode. This could be done by using the method of images, and modeling the PCB electrode ring as a point charge, and the stainless steel electrode as an infinite plate:

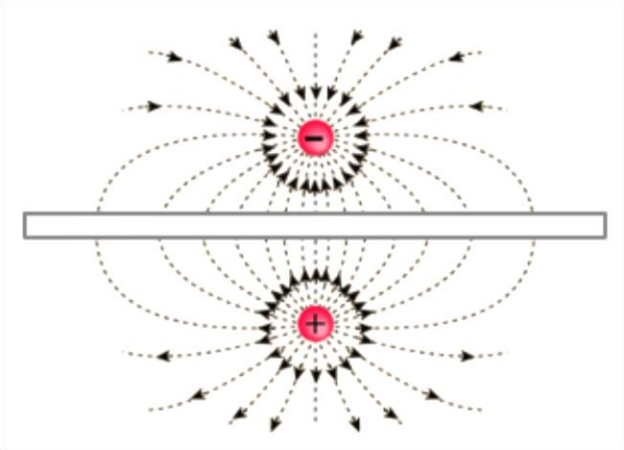

Figure 5.9: Method of images with two point charges is used to find the voltage and electric field at various points between a point charge and infinite plate [24].

Based on this method, the voltage at any point in the region is described as [30]:

$$V = \frac{Q}{4\pi\varepsilon_{w/f}}\left(\frac{1}{\sqrt{\rho^2+(h-y)^2}} - \frac{1}{\sqrt{\rho^2+(h+y)^2}}\right) \quad (3)$$

Since the voltage used for all the tests is known to be 15 V, it is simply a matter of determining the coordinates of the point at which we want to look at the electric field and

finding a representative point charge (Q). Here, h is the height from the bottom electrode to the top printed circuit board (9 mm), and is a constant. The y term will also be constant (7.08 mm), since the electric field and velocity desired is that exiting the frit, which will be constant from there through the channel to the top of the printed circuit board where the droplets grow. To determine the electric field, the partial derivative of V with respect to y is taken because it is the scalar potential of the electric field. It is only with respect to y since the electric field and velocity we are interested in are only in the y direction (the direction that aligns with the channels). The horizontal distance from the point charge, ρ, is first set to zero to determine the equivalent point charge, Q, which would produce a voltage of 15 V. From there it is possible to find the electric field y component at any ρ by evaluating the electric field equation at the calculated point charge and the same h and y:

$$E_y = \frac{Q}{4\pi\varepsilon}\left(\frac{h-y}{\sqrt[1.5]{\rho^2+(h-y)^2}} + \frac{h+y}{\sqrt[1.5]{\rho^2+(h+y)^2}}\right) \tag{4}$$

Now knowing the E-field, the velocity can be determined by equation 1. It is important to note, however, that the electric field crosses through a number of different materials, as well as directly through the water in the channels. The Tango+, VeroBlack or FullCure720, and frit material block some of the effects of the electric field. By looking at the dielectric constants of these materials, it is possible to tell how resistive they are to allowing electric fields to pass through the medium. The dielectric constants for FullCure 720, VeroBlack, Tango+, and Borosilicate Glass (frit material) are 1.98, 1.7, 3.8, and 4.6 respectively (given by manufacturer), while the dielectric constant of water is 80 [29].

The main area of interest, however, only includes the area above and below the frit, which is where water flows. Therefore, the materials of interest include only the frit,

Tango+, and water. When looking through the channels, there is no Tango+ present, and the electrical permittivity can be based on only the frit and water. Since the porosity of the frit is 0.48, the reduced permittivity of the water/frit combination can be thought of as 48% of the electrical permittivity of water. This assumption can be made because the permittivity of glass is so low, it acts almost as an insulator, cutting out 52% of the area that the electric field may pass through. This reduced water electrical permittivity is then 3.398e -10 F/m (dielectric constant is equal to the electrical permittivity divided by the dielectric constant).

Now that all the variables are known, it is possible to solve for the velocity at a number of locations given one active channel. The velocity exiting the activated channel (ρ=0) is calculated to be 0.131 mm/s. This same equation could be used to find the velocity at other channels due to the active channel by changing the value of ρ.

5.6 Simulations

In order to better understand the fluid flow through the channels and frit, COMSOL Multi-physics Simulator was used to determine the fluid velocity of the fluid due to electroosmosis. In the simulation, the frit was drawn, as well as a single channel. In order to simulate this, two physics systems were used: Transport of Dilute Species and General Form PDE. In the first part of the model (Transport of Dilute Species), the continuity equations for the flow velocity and the current density at steady state are solved ($\nabla \cdot \bar{u} = 0$, and $\nabla \cdot \bar{\imath} = 0$, where u is velocity and $i = -\kappa \nabla V$, is the current-density vector). The governing equation for the entire model is:

$$\bar{u} = -\frac{\varepsilon_p a^2}{8\mu\tau}\bar{\nabla}P + \frac{\varepsilon_p \varepsilon_{w\zeta}}{\mu\tau}\bar{\nabla}V \qquad (5)$$

This equation is similar to equation 1. A number of boundary conditions were assumed for this model in order to mimic the conditions of the actual PICEM. At the walls of the frit where water cannot enter or leave, $\bar{u} \cdot \bar{n} = 0$. The pressure at the inlet and outlet of the channel is fixed at zero. Voltage of 15 V was applied to the top surface, and 0V at the bottom outlet (simulating plate and point charge). Furthermore, $\bar{\imath} \cdot \bar{n} = 0$ for all boundaries except for the electrodes. See Figure 5.12 for visualization of boundary conditions.

The governing equations for the dilute species include (See Figures 5.10-5.11 for variables):

$$\nabla \cdot (-\bar{D}_i c_i - z_i u_{mi} F c_i \bar{\nabla} V) + \bar{u} \cdot \nabla c_j = R_j \tag{6}$$

$$\bar{N}_i = -D_i \nabla c_i - z_i u_{mi} F c_i \nabla V + \bar{u} c_i \tag{7}$$

N is the flux vector given by the Nernst-Planck equation (equation 7), where the partial derivative of the concentration of ions with respect to time plus the gradient of N is zero. Essentially, these equations are describing the conservation of mass of a dilute species, and in turn constant concentration.

The governing equations for the general PDE include:

$$e_a \frac{\partial^2 \bar{u}}{\partial t^2} + d_a \frac{\partial \bar{u}}{\partial t} + \nabla \cdot \Gamma = \bar{f} \tag{8}$$

$$\bar{u} = [p, V]^T \tag{9}$$

$$\nabla = [\frac{\partial}{\partial x}, \frac{\partial}{\partial y}] \tag{10}$$

where e_a is a 2x1 zero matrix (since this is a general form equation and there are no second partial derivatives governing the physics of electroosmosis), d_a is a 2x2 Identity matrix, f=0 since there is no forcing function, and Γ is a matrix, "u_flow -kappa*Vx, v_flow -kappa*Vy". Vx and Vy are the gradient of the voltage with respect to the x and y components. These equations use the general PDE form to apply the principles of conservation of momentum (Laplacian of pressure is zero) and the conservation of charges in Darcy flow (Laplacian of voltage is zero). A correction factor was added to account for the thick double layer, as was done in the analytical solution. Throughout the simulation, these equations are used coupled with the above listed boundary conditions in order to solve for the electroosmotic flow throughout the frit and the frit channels. Geometrically, the model consists of a rectangle representing the frit and a channel of proper dimensions projected onto the frit for better visualization of the flow through the area. The constants, their values, and definitions can be seen in Figures 5.10-5.11.

Name	Expression	Value	Description
eps_p	0.48	0.48	Porosity
a	0.575[um]	5.75E-7 m	Average pore radius
eta	1e-3[Pa*s]	0.001 Pa·s	Dynamic viscosity
eps_w	80.2*epsilon0_const	7.101E-10 F/m	Electric permittivity
zeta	-0.1[V]	-0.1 V	Zeta potential
p1	0[Pa]	0 Pa	Inlet pressure
k_p	eps_p*a^2/(8*eta)	1.984E-11 m^3·s/kg	Prefactor, flow-velocity pressure term
k_V	c12*eps_p*eps_w*zeta/eta	m^2/(V·s)	Prefactor, flow-velocity electroosmotic term
kappa	3.5e-4[S/m]	3.5E-4 S/m	Electric conductivity
V1	15[V]	15 V	Anode potential
sigma	0.2[mm]	2.0E-4 m	Concentration-profile peak width
x_m	3[mm]	0.003 m	Concentration-profile peak position
D	1e-9[m^2/s]	1.0E-9 m^2/s	Diffusion coefficient
T	298[K]	298 K	Temperature
nu	D/(R_const*T)	4.036E-13 s·mol/kg	Tracer ion mobility
z	1	1	Tracer ion charge number
c12	0.438	0.438	Correction Factor

Figure 5.10: COMSOL variables, values, and descriptions.

Name	Expression	Unit	Description
u_p	-k_p*px[Pa/m]	m/s	Flow-velocity pressure term, x component
v_p	-k_p*py[Pa/m]	m/s	Flow-velocity pressure term, y component
U_p	sqrt(u_p^2+v_p^2)	m/s	Flow velocity pressure term, magnitude
u_eo	k_V*Vx[V/m]	m/s	Flow-velocity electroosmosis term, x component
v_eo	k_V*Vy[V/m]	m/s	Flow-velocity electroosmosis term, y component
U_eo	sqrt(u_eo^2+v_eo^2)	m/s	Flow-velocity electroosmosis term, magnitude
u_flow	u_p+u_eo	m/s	Flow velocity, x component
v_flow	v_p+v_eo	m/s	Flow velocity, y component
U_flow	sqrt(u_flow^2+v_flow^2)	m/s	Flow velocity, magnitude
c_init	1[mmol/m^3]*exp(-0.5*((x-x_m)/sigma)^2)	mol/m³	Initial concentration distribution

Figure 5.11 COMSOL variables, values, and descriptions.

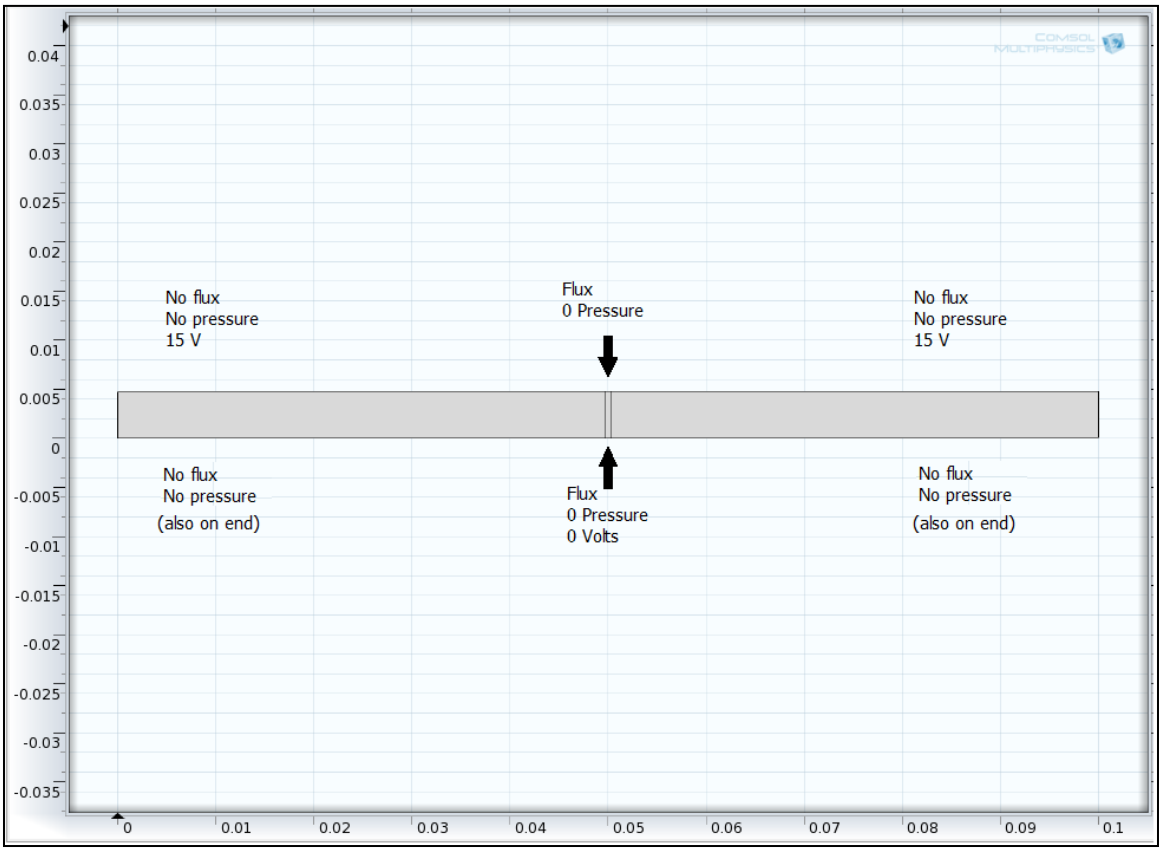

Figure 5.12: Image of COMSOL geometry and boundary conditions.

In the first simulation the frit was modeled with a single channel (2D). Flow was allowed through the inlet and outlet only (since the other areas are blocked off by Tango+, the electrode, and printed circuit board). The results of this simulation included a number of

velocity profiles that explain the movement of water throughout the frit (Figures 5.13-5.16). The first plot, Figure 5.12, shows combined velocity terms due to all of the preset physics and is dependent upon both the dilute species and general form PDE models. The velocity at the inlet and outlet are much higher than the other areas. This is due to the fact that the driving force is the electrode on top and the "point charge" at the outlet. All arrows that come from the inlet, eventually lead to the outlet, and the velocity through the rest of the porous medium tapers off quickly within a millimeter. This model shows that while much of the liquid is going through the channel, some of it is also going through other parts of the frit before coming back to the outlet.

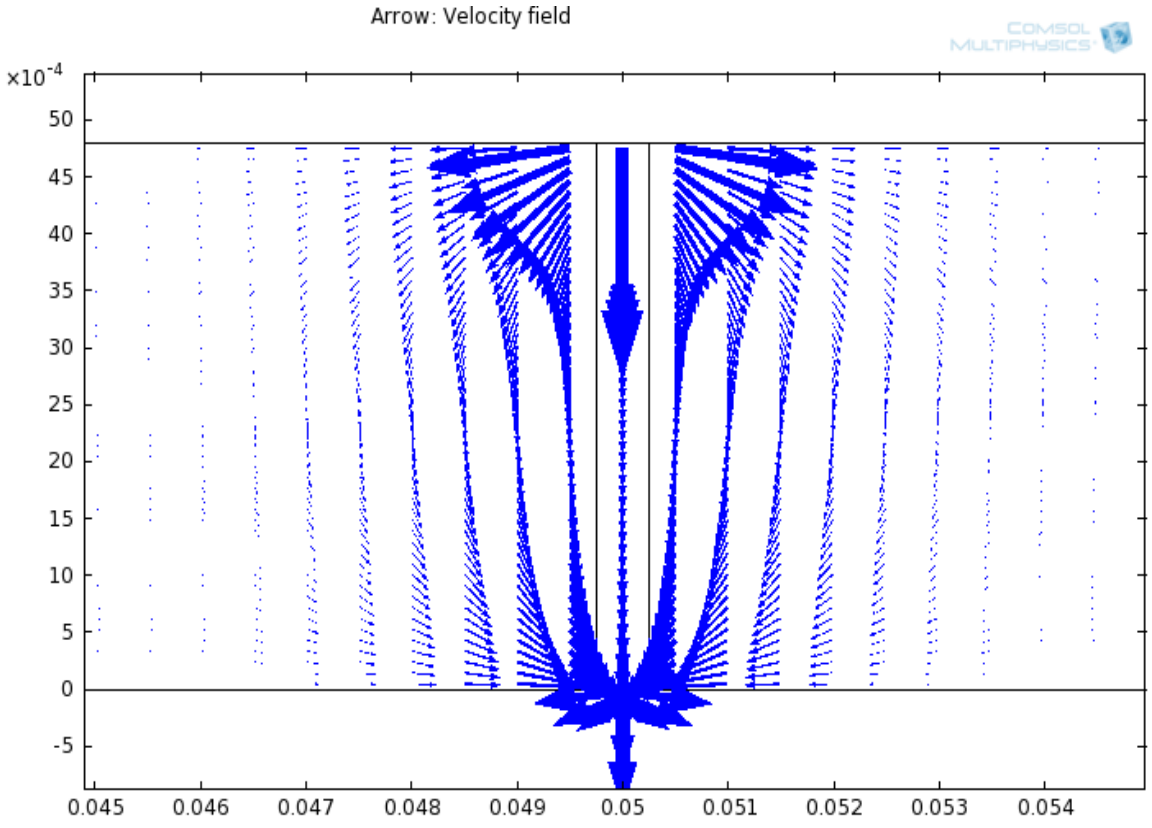

Figure 5.13: Full velocity profile. Arrows represent the velocity and are proportional by size (15V).

A surface plot was created in order to determine magnitudes of the velocity in and around the channel (Figure 5.14). All red areas indicate zero velocity. The area of most interest is the outlet at the bottom, which shows a range of velocities between 0.11-0.13 mm/s. At the corners of the outlet, there are sharp changes in velocity due to the fact that the water that has spread throughout the frit is now gathering back to the outlet. The velocity through the channel in the frit changes due to this dispersion; however, once the water leaves the frit the velocity is constant at the outlet velocity. Furthermore, there is a discontinuity at the corners due to the interface of two different boundary conditions meeting. One allows flux (the outlet); the other (the frit surface blocked by Tango+) does not. Therefore, there are sharp changes in velocity at these points.

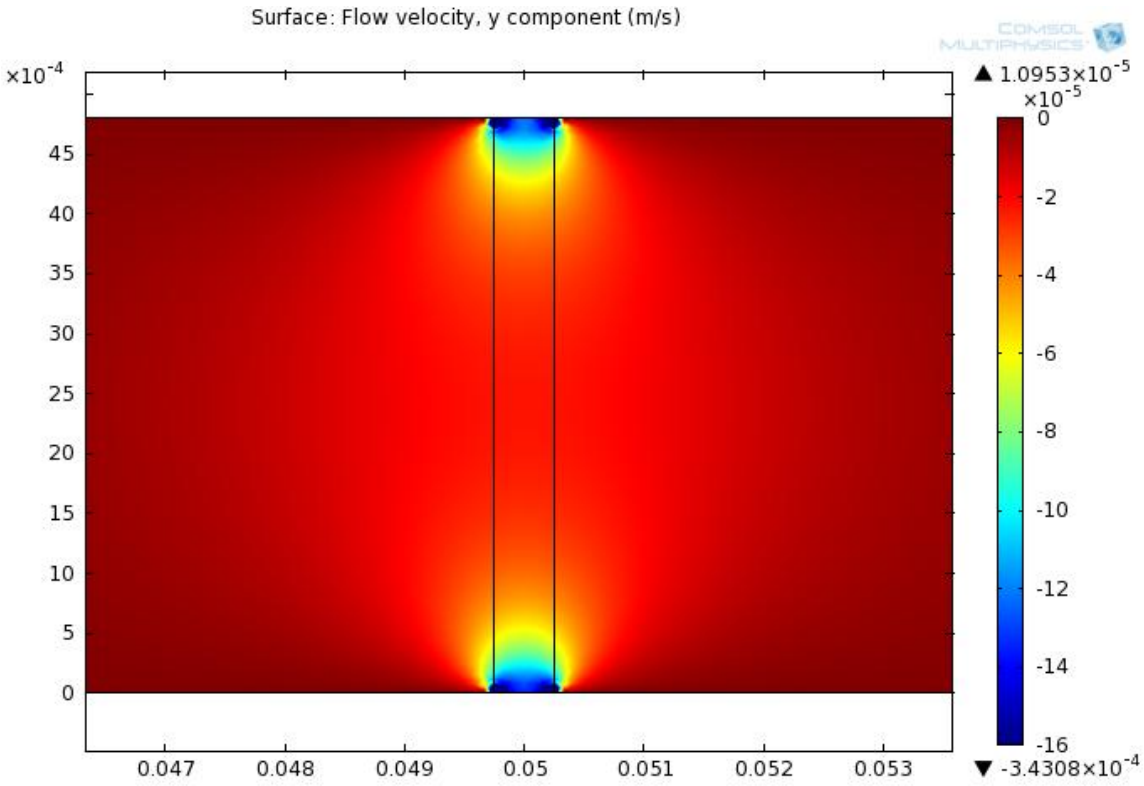

Figure 5.14: Surface plot of the y component of velocity, where y is up and down (15 V).

In order to get a better idea of the velocities at the outlet, a line plot was created for the y velocity (Figure 5.15). In this figure, the horizontal line between the two vertical lines that demark the channel is the outlet. From the scale at the center of the outlet, the velocity can be more accurately read as approximately 0.125 mm/s. Again, at the edges, there are residual effects from the water moving around sharp corners, and the velocity is higher here due to the higher change in velocity as it is pushed towards a more confined outlet area. In these studies, the bulk flow is analyzed, which would be the flow in the center of the channel, and therefore, the effects at the corners will not be considered in further analysis.

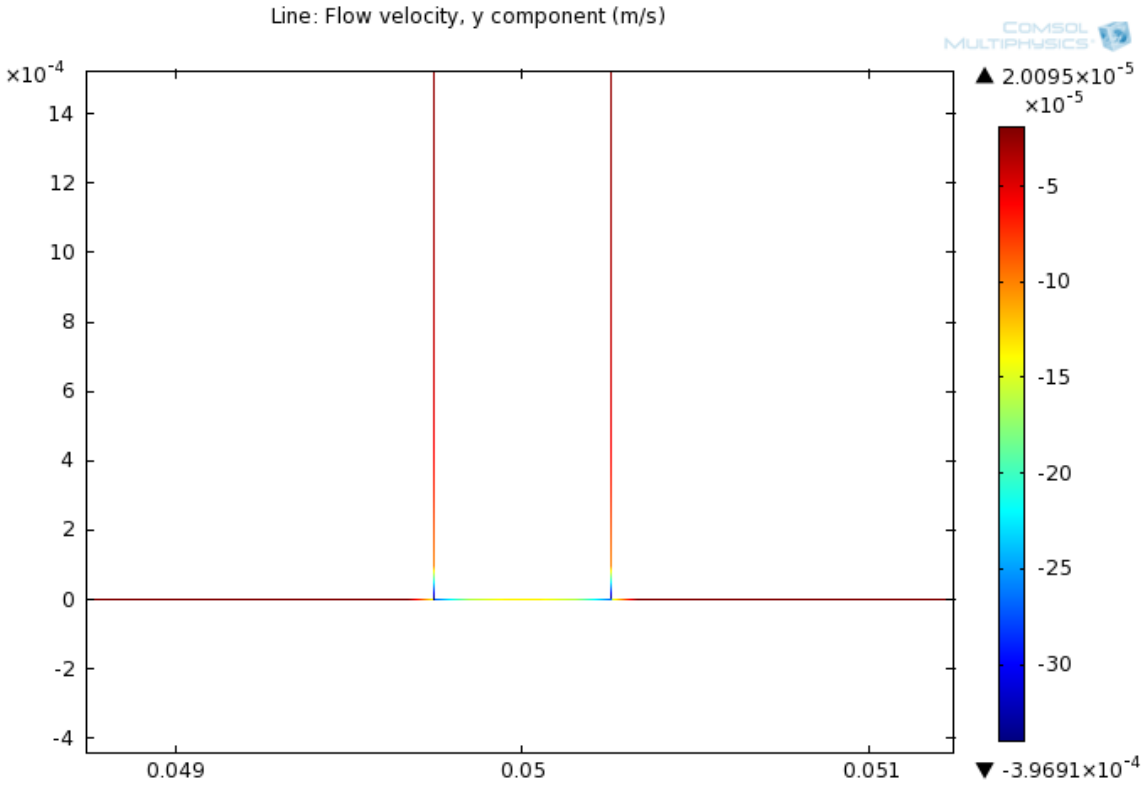

Figure 5.15: Line profile of velocity at the outlet (15 V).

Next, a streamline velocity plot was created to see where the water flows from the inlet. It can be seen that it matches up well with Figures 5.13 and 5.14, where the water moves from the inlet to other areas of the frit, eventually ending up again at the outlet. Again, this is expected since there is nowhere else for the water to go (and must abide by the conservation of mass condition) and the 15 V across the two electrodes (in this case modeled as a point charge at the outlet and a plate on top) drives the water back to the outlet.

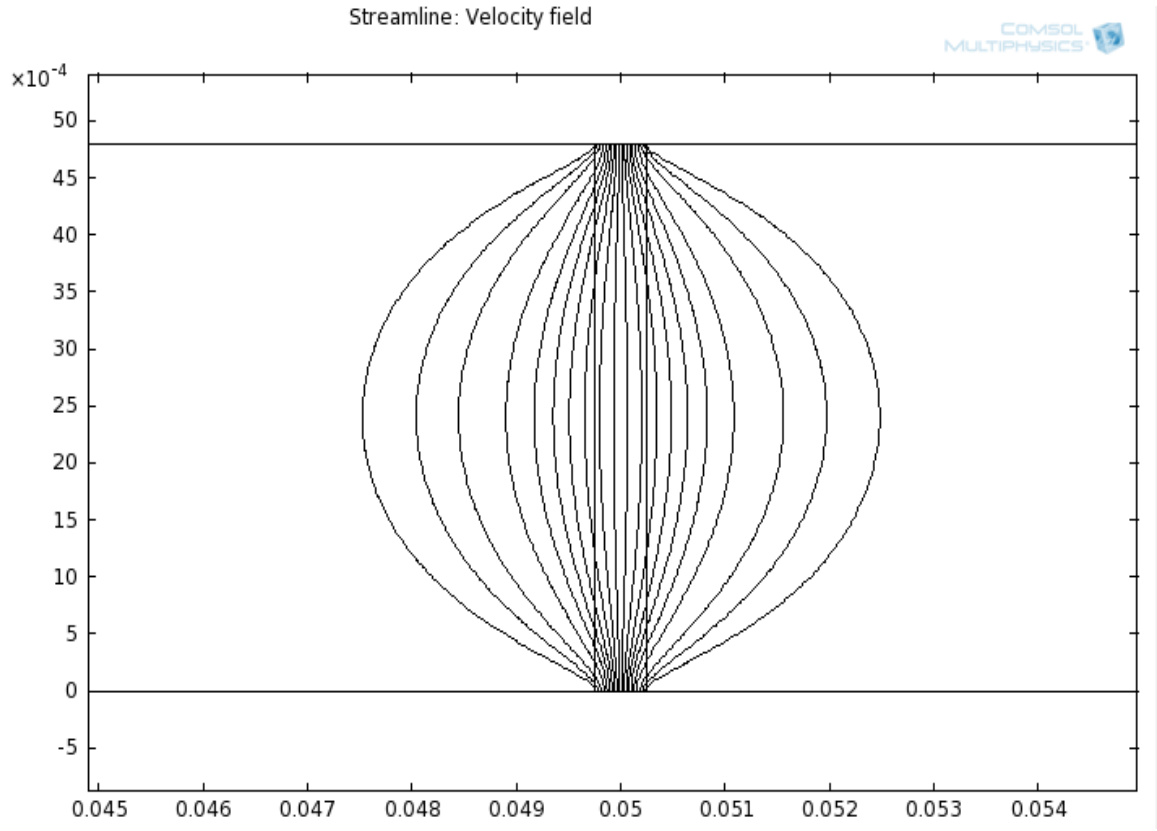

Figure 5.16: Streamline plot of velocity from inlet to outlet (15V).

5.7 Effects of Single Channel Activation on Nearby Channels

As mentioned earlier, some droplet growth was found at inactivated channels nearby an activated channel. This growth was attributed to the y components of the electric field lines causing flow from the base electrode field lines moving towards the small ring of charge at the activated channel. In order to explore these effects further, two COMSOL configurations were examined, and the velocity at each neighboring pore was calculated analytically.

5.7.1 Single Channel Activation with passive neighboring channel

In these simulations, like those before, dilute species and general form PDE were used as the main physics modules. The changes occurred in the boundary conditions. Zero pressure was applied to the inlet and outlet of the second channel, and flux of dilute species was symmetry boundary condition conserving mass throughout the system was applied at these ports as well. In Figure 5.17, the velocity arrow field can be seen for the effects of the two physics modes. Instead of water leaving the second, inactive outlet, the water near that area is actually getting pulled towards the charge at the activated outlet. This is contrary to physical experimentation, where occasionally there is water growth in neighboring channels. The important difference between the experiment and simulation is that the simulation is acting at steady state and the experiment is not necessarily at steady state due to slight voltage fluctuations due to the voltage source, chemical reactions within the frit, and vibrations induced by the xyz platform. Just like the single channel analysis, the flow from both ports acts in an arced motion, spreading through the frit but eventually returning to the outlet with electric charge, which is dictated by the conservation of mass boundary constraints.

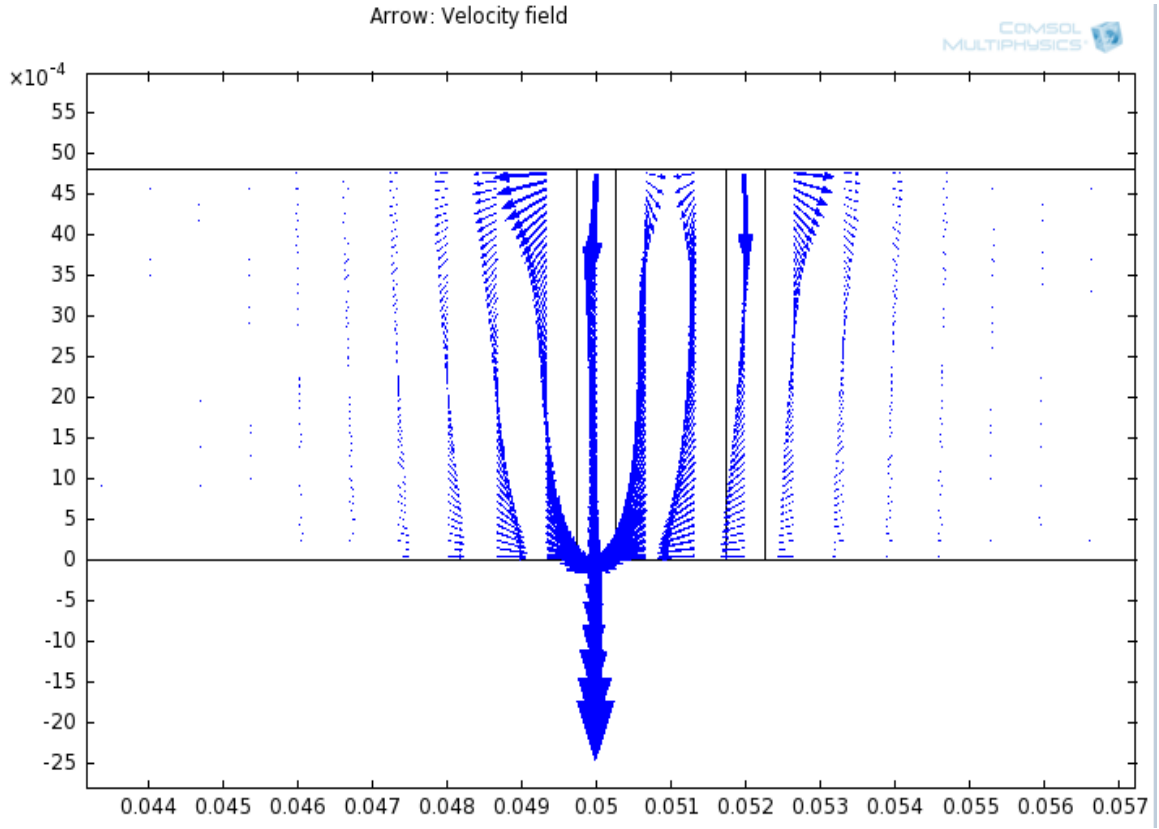

Figure 5.17: Arrow field of velocity experienced when an inactive pore is introduced (15 V).

In order to quantify the velocity, a surface plot was created (Figure 5.18). Based on this plot, velocity at the outlet is approximately 0.14 mm/s, which is slightly higher than the single channel model. This would result from the added water source provided by the second inlet. The velocity at the second outlet is actually positive, or upward, which is in line with the steady state solution in which the water will be pulled from that region towards the outlet with the charge.

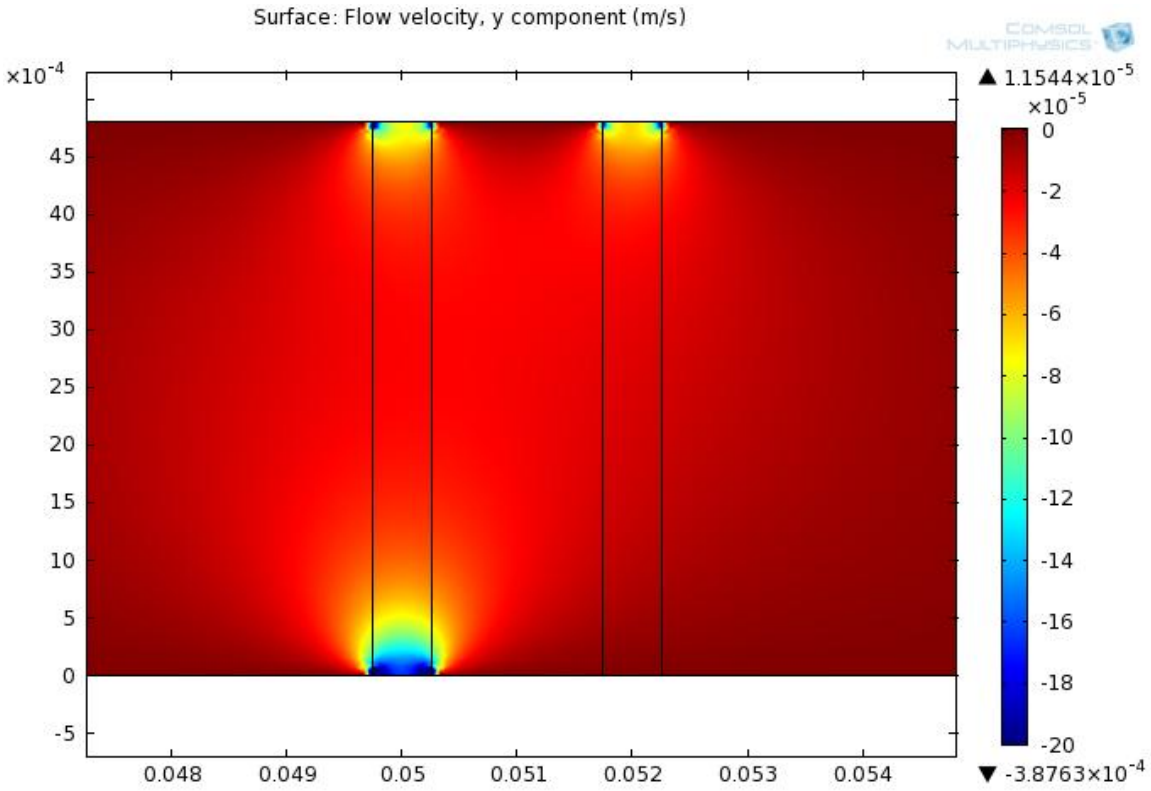

Figure 5.18: Surface plot of y velocity when inactive channel is introduced (15 V).

To get a more accurate reading of velocity, a line plot was used (Figure 5.19). Again, at the activated outlet, the velocity is approximately 0.13 mm/s exiting the channel.

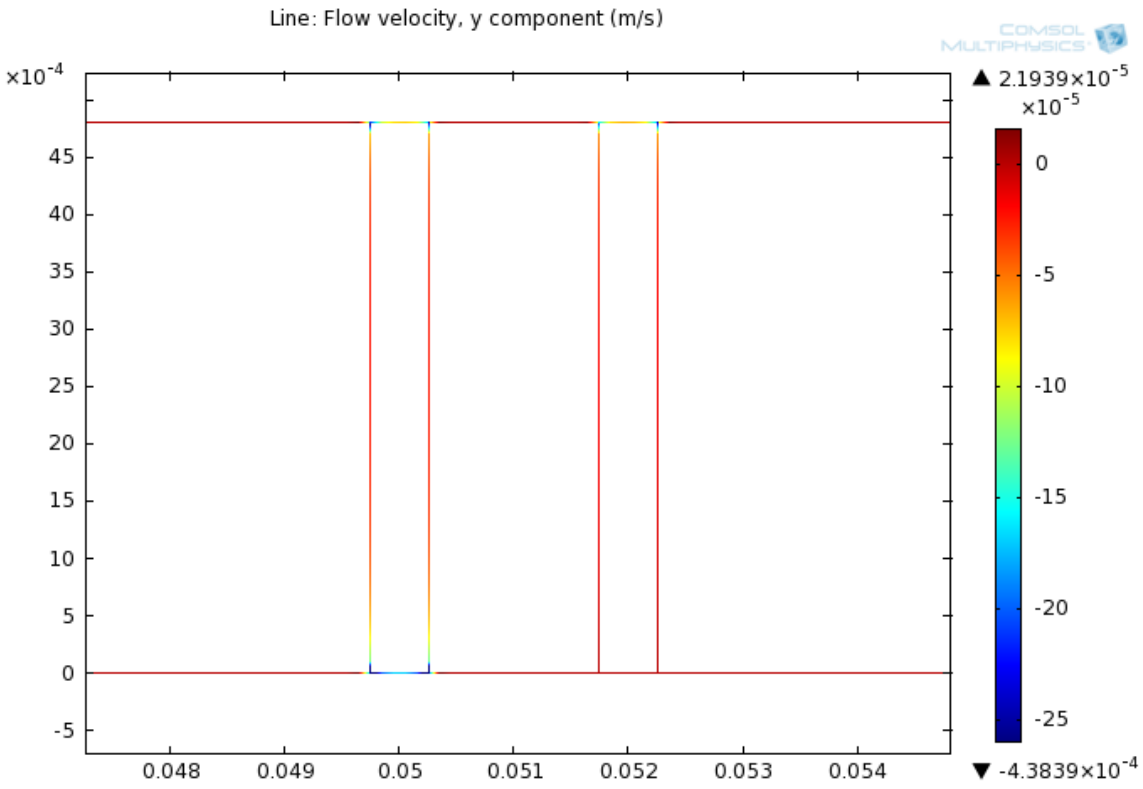

Figure 5.19: Line plot for y velocity when an inactive channel is introduced (15 V).

A streamline plot was created to see where the water from the two inlets is directed (Figure 5.20). It can be seen, again, that once the water enters the frit, it spreads out from the inlet, but eventually gets pulled back to the outlet voltage source. The distance between the lines denotes the magnitude of the velocity different between neighboring lines. Note that the lines near the outlet are very close, indicating that they are all very high velocity.

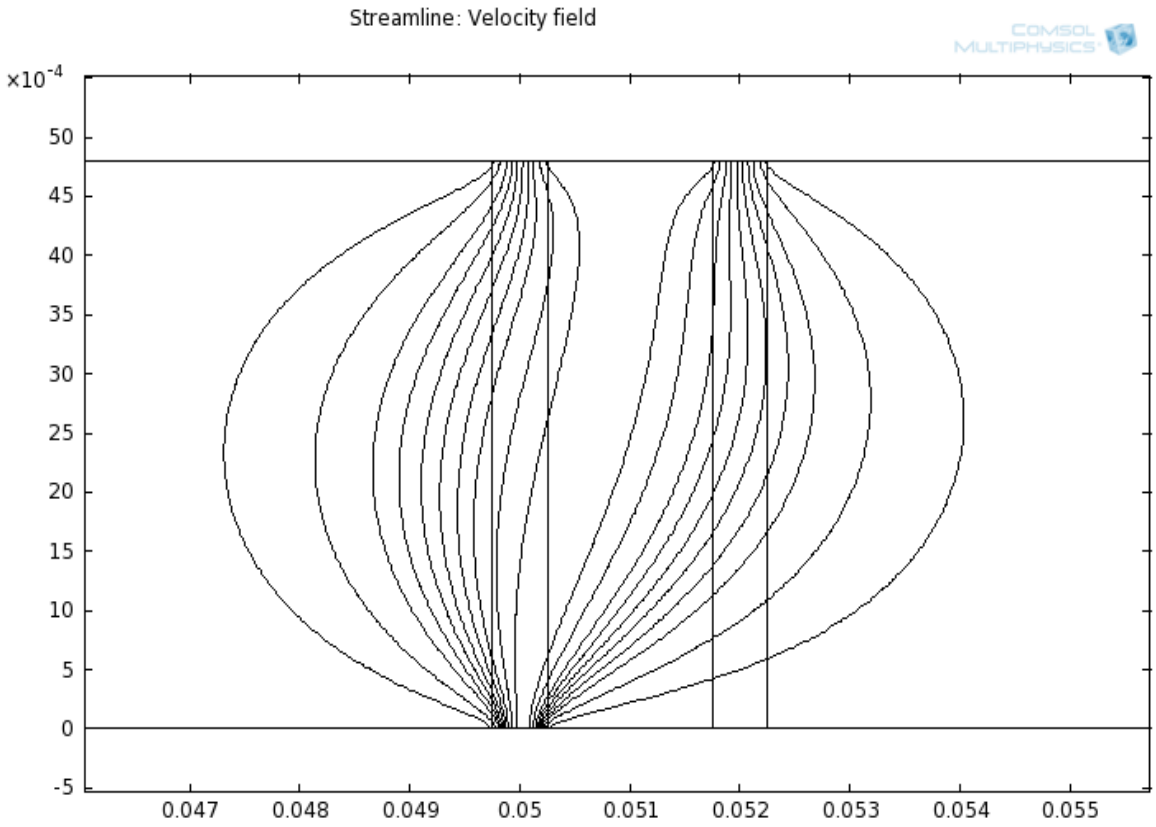

Figure 5.20: Streamline plot of velocity field from two inlets where water is introduced (15 V).

5.7.2 Double Channel Activation

COMSOL was also used to view velocity profiles of double channel activation. The boundary conditions were altered to apply a charge on the second outlet. This means at the two outlets 0 V was set as the boundary condition and ion flux allowed at each inlet. As expected, there was a high degree of symmetry throughout the models. In Figure 5.21, the two channels appear as a superposition of two of the single channel velocity arrow profiles. From the line plot, Figure 5.22, the velocities exiting the device are approximately 0.125 mm/s, matching with the individual channel velocity.

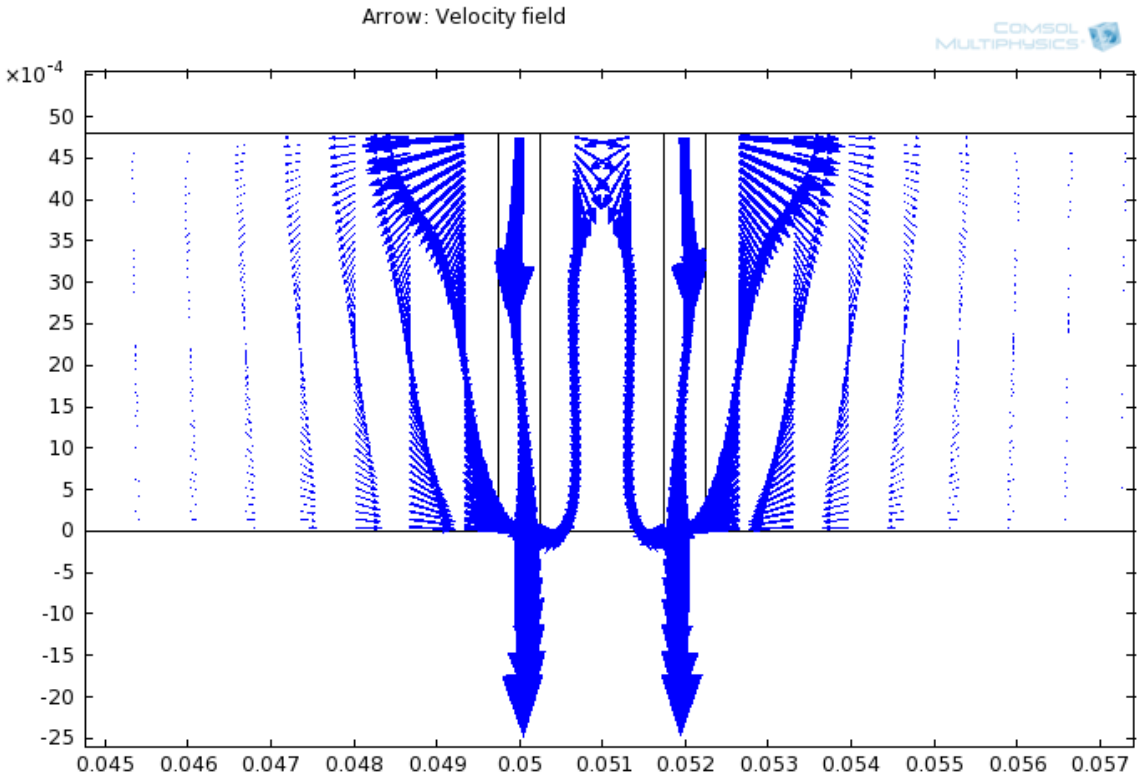

Figure 5.21: Velocity arrow plot for two active channels (15 V).

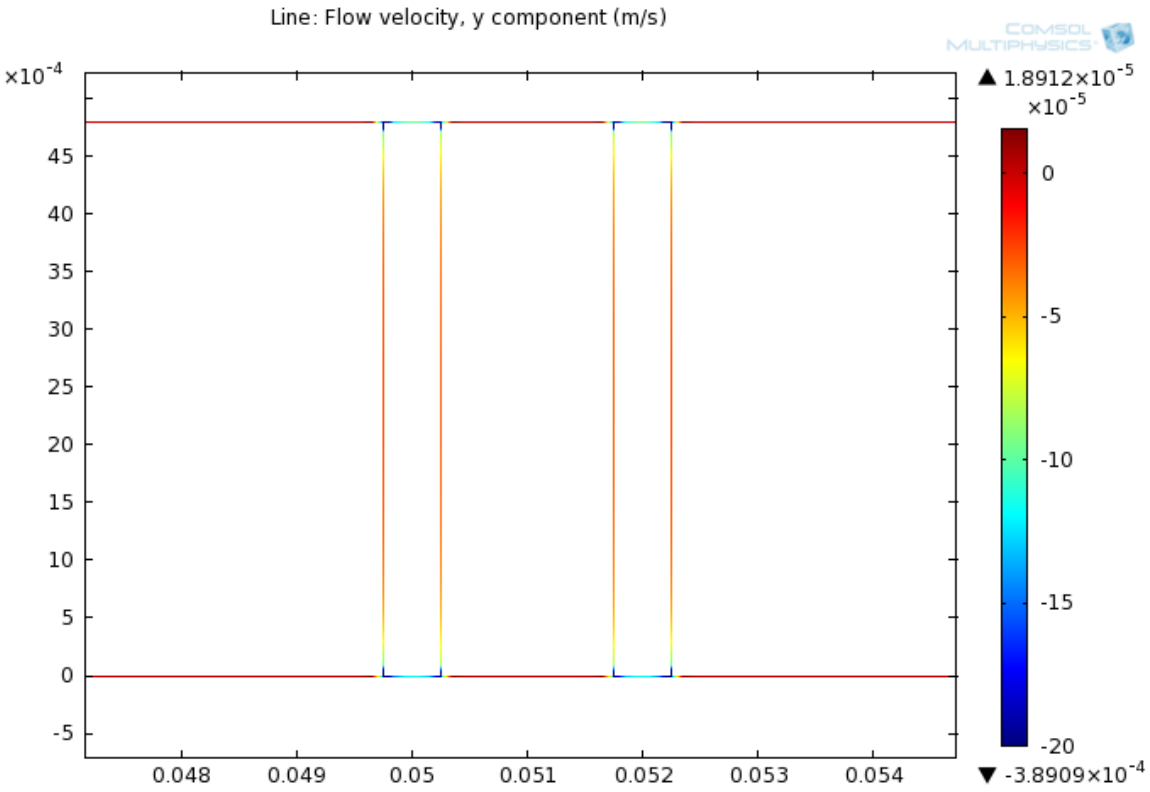

Figure 5.22: Velocity line plot for two active channels (15 V).

Again, a streamline plot was produced (Figure 5.23), which shows the velocity lines from both inlets. The water coming in from each inlet exits through its corresponding outlet. In between the two channels the velocity flow is almost completely vertical due to the equal and opposite forces pushing the velocity towards the center and back to the corresponding charged outlet.

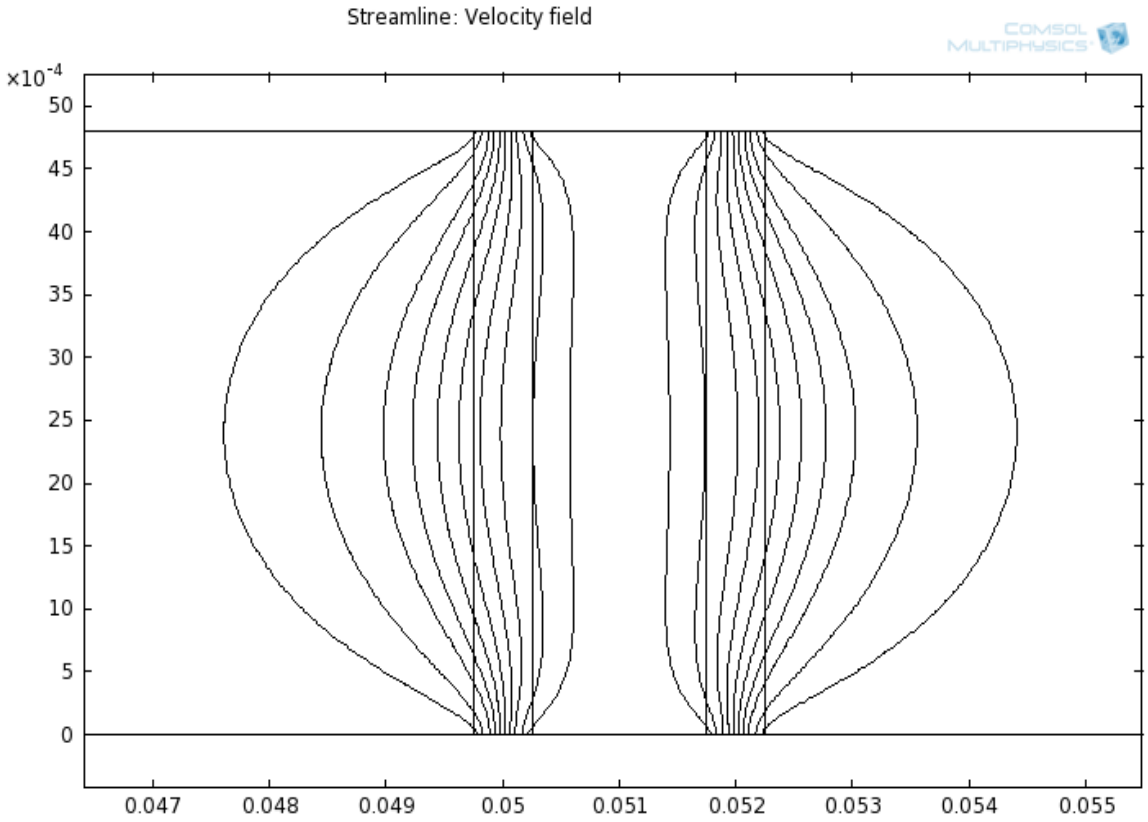

Figure 5.23: Streamline plot for two active channels (15 V).

Finally a surface plot was created for the velocity through the two active channels (Figure 5.24). Again, the velocity can be approximated to be 0.125 mm/s. The effects of the velocity outside the two channels taper off to zero within about a millimeter.

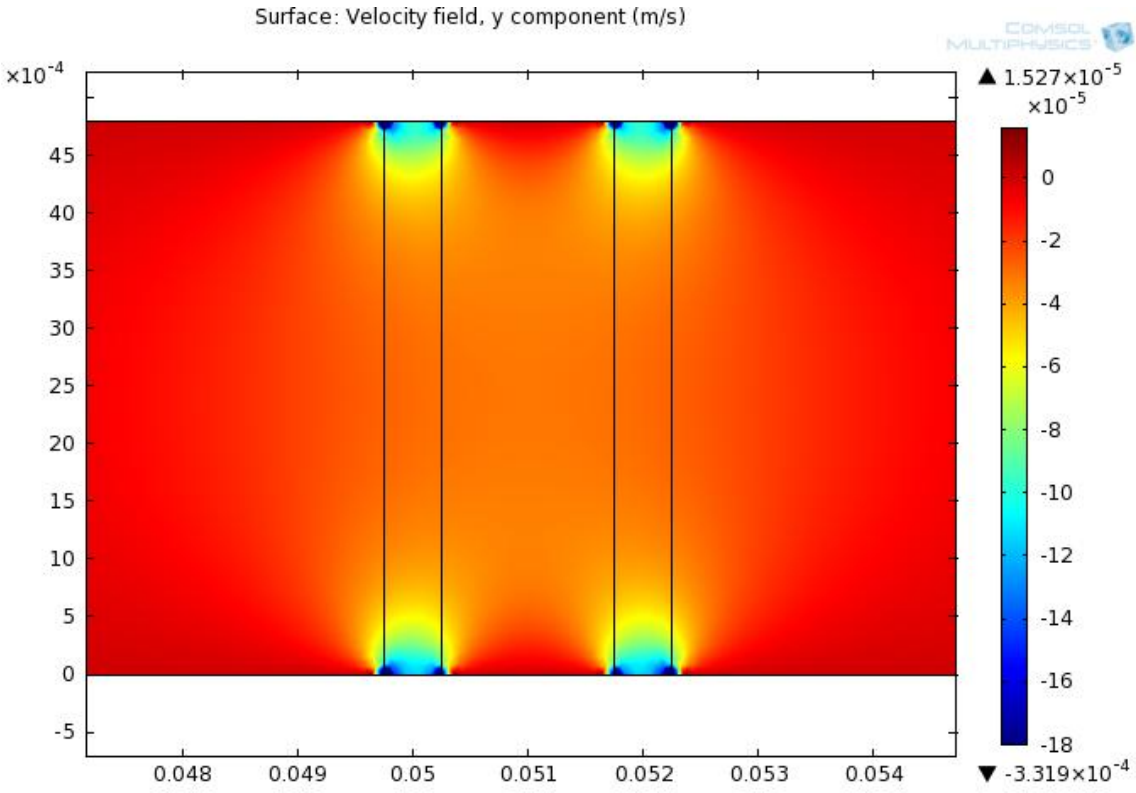

Figure 5.24**:** Surface plot for two active channels (15 V).

5.7.3 Analytical solutions for single channel activation effects on neighboring channels

From analytical results, the velocity of the liquid in the surrounding channels can be computed from equation 1, where instead of ρ being set to zero to find the velocity at the activated channel, it is set to the distance of the neighboring pore. In Figure 5.25, the velocity decreases as a function of approximately c/r^2, where c is a constant and r is the distance between the source and the location of interest. This matches the theory of the decay of a point charge electric field decreasing proportionally to the inverse of r^2. From this information, it shows that since the locations are so close to the point charge (as opposed to the plate) that they seem to better fit equations relevant to point charges. This would explain the high velocities near the channel that are not physically experienced. While this model is sufficient for finding the flow of liquid directly in the activated channel (simulated by the point charge), it over-estimates the electric field magnitude due to the point charge assumption and the lack of incorporation of droplet resistance. Furthermore, this model does not take into account that part of the electric field which passes through the Tango+, which is an insulating material based on its dielectric constant. That means the electric field experienced, and therefore the velocity induced, would be lower than these values.

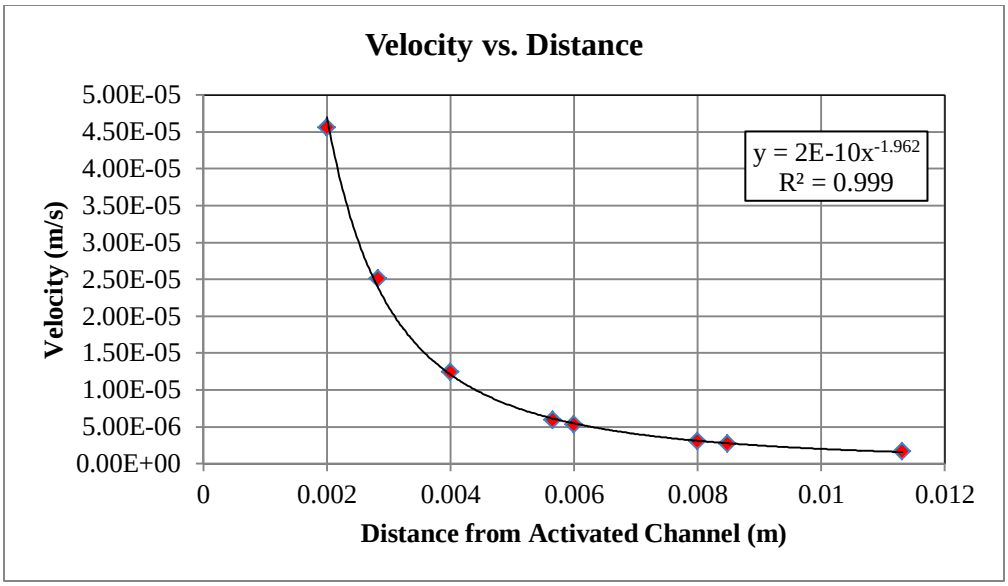

Figure 5.25: Distance vs. Velocity (y direction) plot based on method of images.

5.8 Comparison of Results

In order to fully assess the time scale of the pick and place process, it is necessary to be able to accurately predict the velocity of fluids operating under different experimental conditions (i.e. applied voltage, channel diameter, frit properties, etc.). In the case of the electrokinetic processes, knowledge of the double layer thickness, zeta potential, electric field strength, and surface potential is crucial in modeling the velocity field accurately. These quantities can be difficult to measure reproducibly and so now the discussion will shift towards a more qualitative description of how the velocity would change if certain parameters were to increase/decrease.

In our case, the parameters with the largest uncertainty are the Debye length and the electric field strength. As was mentioned before, the Debye length is most likely smaller than the theoretical upper limit on distilled water of 970 nm (we assumed a large electric double layer or EDL). The distilled water resides in a plastic jug and comes into

contact with the air each time the container is opened. Not only are there chemicals leaching from the plastic but there is also dissolution of CO_2 from the air into the water. There is also the possibility of contamination as a result of handling the frits with bare hands and not chemically treating them prior to use to rid them of any organic contaminants or loose particulates from processing them into different shapes. There is also the chance that some of the surface groups of the borosilicate glass frit could dissolve. Dissolution of CO_2 alone produces a Debye length of 215 nm [20]. Inclusion of the other effects could further decrease the Debye length to something on the order of ten nanometers or possibly even smaller. To see the effects of a thin double layer on the axial velocity, the coefficient c_{11} in front of the electroosmotic term in equation 1 was set to one (for small EDL), and both the simulation and the theoretical models were recalculated. The results of these calculations, the experimental value determined from image analysis, and other case studies (permeability and capillary pressure) are summarized in Table 5.6.

Table 5.6: Comparison of results.

Case:	Velocity (mm/s) of main channel
Experimental	0.136
Analytical (Thick EDL)	0.131
Analytical (Thin EDL)	0.305
Simulation (Thick EDL)	0.125
Simulation (Thin EDL)	0.300
Case:	Pore Radius (microns)
Experimental	2.08
Manufacturer (ROBU)	0.575
Case:	Permeability (m^2)
Analytical (bed of spheres)	6.16E-15
Manufacturer (ROBU)	4.95E-15
Outsourced (PMI)	2.85E-15
Case:	Capillary Pressure (psi)
Experimental	26.95
Outsourced (PMI)	22.87

From Table 5.6, we can see that there is agreement between the theory and the simulation. This is expected, since the set of equations used in the simulation reduces down to the same equation as the theory under conditions of steady state. Notice that the predicted velocity in the case of a thick double layer is about twice the experimental value whereas in the case of a thin double layer, the predicted velocity is four times greater. The discrepancy may be explained by the uncertainty in the electric field. The electric potential equation was derived under the assumption that both the point charge and the infinite plate were suspended in a medium with a permittivity equal to $\varepsilon_{w/f}$. This is not actually true. From Figure 2.3, we see above the frit there is only water but the image charge actually resides somewhere in the reservoir. And since the permittivity of water is much higher than that of the frit, much of the electric field strength is lost to the polarization of the water molecules [33]. Furthermore, the voltage has to pass through a

number of electrically resistive materials. Since these are in series, the frit itself will not experience the whole 15 V. Hence, the effective potential difference across the frit could be smaller than the 15 V.

Furthermore, the analytical solution treats the electric field as that between a point charge and an infinite plate. In reality, it is not a point charge, but a thin cylinder of Sn/Pb coating around the channel, and the plate is not infinite. Therefore, this causes the electric field at areas near the printed circuit board to appear as a point charge, which creates a large electric field at areas close to the source. In reality, these numbers would be lower since it is not, in fact, a concentrated point charge. If the method of images is used for a thin ring, the electric field is 96.2% of the point charge model. Also, the simulation models the outlet charge as a line charge in 2D, when realistically it is an outline of a sphere in 3D.

In addition, as a result of the capacitance effect of the double layer, the potential difference is decreased even further and becomes a time dependent quantity [33]. For a similar setup [32], it has been found that the effective potential difference is around half of the applied value. Their model takes into account the resistance of the electrode, fluid, and the frit in addition to the capacitive effects of the electrode. A lower electric potential corresponds to a smaller electric field, which, in effect, corresponds to a smaller velocity. This holds true irrespective of the double layer thickness. There is also capillary pressure and ion charge concentration building over time as the water droplet forms above the printed circuit board, which is not taken into consideration in either the analytical or simulated solutions, but is experienced in the experimental velocities.

Another major issue which may influence the success rate of picking or not picking spheres is related to the fact that the reservoir is not currently vented to the atmosphere. During pumping of drops, the pump is pulling against the syringe which would tend to create suction within the device. By incorporating a tube connected to the atmosphere, any such suction would be largely eliminated. Beyond just that, whenever there is curvature difference between any two drops (as experienced in the trials), there will be capillary pressure difference between those drops. In such a case, one drop can remove volume from the other, sometimes called volume scavenging [34]. How fast volume scavenging occurs depends on the resistance to flow between the drops and the driving pressure difference. These flows could be accounted for by including the Darcy term and introducing a capillary pressure driving force.

There is also experimental variability to consider. These conditions include slightly varying voltage (15.3V-14.5V) due to the voltage source, vibrations affecting the xyz platform and thus the PICEM, and chemical reactions happening inside the frit. However, the experimental velocity was in between the analytical and simulated values for the thick and thin EDL, which is to be expected since we are looking at upper and lower bounds. It is closer to the thin EDL velocity, which leads to the conclusion that the water used was not pure distilled water and that fouling had occurred.

Next, it is important to look at the other parameters studied. When looking at the pore radius, the microscope results were four times larger than the manufacturer's specifications. The average radius was supposed to be 0.575 microns, but the manufacturing process (and the compression process) allows for variations throughout the frit. Even from PMI data, different permeabilities were found for different parts of

the frit. This leads to the belief that the frit does not have uniform pores. Under the microscope, it was possible to see the large pores, but smaller pores were not visible. Therefore, the results were skewed in the direction of large pores. Furthermore, under the microscope, all images were examined in the plane perpendicular to the direction of compression. This means all in plane results would be stretched. Any out of plane pores would be compressed to a smaller radius. Were it possible to example out of plane surfaces, it is possible that these pores would become visible under the microscope changing the average radius of the pores.

As for the permeabilities, the outsourced average permeability was about half of the analytical and manufacturer's value. This could be due to errors in the experimental testing of the frit. The frit was epoxied on the sides in order to reduce the chance of water flowing around and not through the frit. Since the frit is porous, the epoxy is absorbed by the frit, and may have bleed through to some of the areas being tested. If epoxy were to enter into the testing region, this would decrease the flow through the material, therefore decreasing the permeability.

Finally the capillary pressures from both experimental testing and PMI data were very close. Differences between the two could involve the fact that they were testing a different frit than what was used in the experimental testing. Since each frit is slightly different in permeability, pore size, and pore distribution, it is possible that there would be variances amongst the two frits that would explain this discrepancy.

CHAPTER 6

Conclusions/Results

The experiments have shown that electroosmosis can be used in an individually addressable arrayed device to pick up objects with minimal energy and no mechanical input. While the placing capability was not thoroughly examined, placement only requires reversing the polarity of the voltage and decreasing the volume of the capillary bridges. The constant-volume instabilities of a liquid bridge pinned on a plate at one end and a sphere at the other end are already well characterized. Once the sphere or tile is in contact with its base the objects can be force fit using the circuit board platform as a force base to interlock tiles or place spheres. Regarding the accuracy and reliability of the device, the checkerboard platform is the most intricate design possible to show the capabilities of the PICEM. Success rates were high in all trials, but a much higher success rate could be established with more precise mechanical apparatuses that are used to move the PICEM device. For instance, the platform on which the spheres rest is not completely level, nor was the circuit board face with respect to the sphere array. This would cause inconsistencies in pick up, especially around the edges, which can be seen from the data. However, since the PICEM device did have a 100% success rate on creating droplets in the desired configurations, it is only a matter of perfecting the positioning apparatus in order to increase success rates.

Since the current design has 0.508 mm diameter channels for water droplet growth, it has a limited ability to pick up small objects with maximum dimensions around this range. In the future, this limited capability will be removed. Because of the modular

design, the top circuit board can be easily customized for the application at hand by altering the density and diameter of the channels. Consequently, the PICEM device will be able to pick up objects as large as 2 mm (based on the capillary length of the liquid, which in this case is water), and is limited in size decrease mainly by manufacturing processes. As shown in testing, the PICEM was able to pick up 1.5 mm plastic spheres, 3D printed tiles, 1.5 mm stainless steel spheres, and circuit board components. Limitations include the smallest size hole that can be drilled into a printed circuit board, as well as the changes in frit pore size due to a smaller channel diameter. At smaller diameters, Debye lengths include due to the higher surface area to volume ratio, and hydrostatic pressure must be considered.

Furthermore since each of the slices in the device is individually 3D printed, it is already set up for rapid mass production. Currently each of the slices in the device is individually 3D printed and assembled. However, as technology progresses, the two different materials used in the layers (Tango+ and FullCure720) will be able to be printed in one process further removing steps in the assembly process. This multi-material printing is already available, but has limitations in terms of quality of printing small features—something necessary in creating the Tango+ gaskets with holes the diameter of the object needed to be picked and placed.

Beyond just the assembly and hole size, the length of the arrays on the circuit board will be able to be expanded to hold millions of channels. Expanding this 5 x 5 array to a larger scale will only require larger circuit boards and a slightly more complex control system. At this point the device is controlled by manually connecting a voltage source. However, it will be easy to connect this system to a computer in order to

individually control the voltage flowing through each channel. This would allow for both positive and negative voltage to be used simultaneously to ensure that each droplet is uniform and consistent amongst the array.

In terms of tile assembly, which is what has been studied in this lab, the future holds the creation of nanofabricated tiles that are small enough to appear as sand. These tiles would be put on a shake plate for alignment and the PICEM device would be able to hold a million channels to pick from the variety of plates of tiles for the desired final assembly. This is very much related to current patent docket # D-4009-01 regarding digital matter. However, on a grander scale, this device could be used to pick up objects of varied size, have the ability to stack these objects, and to have an integrated control system to ensure desired droplet size and picking ability. Furthermore, other liquids could be used for different desired surface tensions for the particular surface materials of the objects to be picked.

Based on the comparison between experimental testing, COMSOL simulations, analytical calculations, outsourced testing, and manufacturer's specifications, it can be seen that the PICEM device is a reliable and accurate means of picking millimeter scaled objects in parallel and with individual control.

6.1 Contributions of This Thesis

1. A printed circuit board was designed to individually control a parallel pick and place electroosmosis device, allowing for mass parallel motion.
2. 3D printing and digital materials were used and optimized for electroosmotic flow through a frit.

3. Tests were performed in order to quantify the reliability of individual control of the PICEM, including unique configurations pick up: all spheres, single spheres, rows, checkerboard pattern, X shape, # shape, small square, and top hat shape.
4. Capillary pressure for ultra fine borosilicate glass frits was determined for the frit using weights and ring stands for frit characterization.
5. ROBU Ultra Fine frit was characterized for permeability and for capillary. This information was not known to even the manufacturer.
6. A provisional patent has been filed for the PICEM device.
7. Analytical solutions to electroosmotic flow through channels of porous media were created and evaluated.
8. COMSOL simulations were created simulating electroosmosis through channels of porous material, determining how electric fields cause velocity throughout the PICEM mechanism.
9. Simulations, experimental testing, outsourced experiments, manufacturer's data, and analytical solutions were compared in order to verify accuracy of the PICEM.

6.2 Contributions of Others to This Thesis

1. A printed circuit board was designed with the help of Robert MacCurdy to allow for the individual control of water droplets using electroosmosis.
2. An xyz platform was created based on a design by Dr. Jonathon Hiller in order to control the motion of picking and placing.
3. All troubleshooting of the SECAD and PICEM device and MotionPro analysis was done with the help of Ashley Macner.
4. Help with analytical solutions and editing from Ashley Macner.

APPENDIX A

Table A1: System comparison of current technology for pick and place.

System	Aproximate Object Scale	Parallel	Physics	Major Limitations
Micro Chemo-Mechanical System (MCMS) [13]	200-500 microns	No	Chemical reactions with acetic acid and hydrogren peroxide	Must submerge in chemicals
AFM/SEM and laser ablation [11]	200-400 nm	No	Lasor ablation is used to cut into nm scale objects, joy stick to move object	Very expensive and complicated to replicate
Metallic Microgripper (SU-8 adapter) [9]	52-165 microns	No	Voltage and pulsed wave voltage close jaws of microfab gripper	Manual alignment makes for signification deviation of tool head.
Single Crystal Silicon deep reactive ion etched locking notches [8]	100 microns	4 in parallel	Electrothermal, electrostatic, and piezoelectric techniques	Extremely fragile, extremely specialized end effectors
Microfabricated Grippers [7,10]	5 microns	No	Scanning Probe Microscopy, electron beam deposition for local glueing and bonding	No integrated feedback, SEM needed, limited range of picking techniques
Needle-tip with SEM [6]	1 micron or less	No	Electrostatic forces to pick, needle to push and move laterally	No placing ability, electrostatic forces unreliable
Pick and Place Shape Forming [5]	1 micron or less	No	Electrostatic forces to pick, needle to push and move laterally	No placing ability, electrostatic forces unreliable
Vacuum Tool and Nanorobot [3]	100 microns	No	Pipettes use pressure changes to push and pull objects	No accuracy in placing, fragile tools, use another end effortor for hand-in-hand operation
Water mist and Tweezers [14]	200 microns	No	Droplets are put in close contact with each other using tweezers, mist serves to force final alignment	Still need external fragile grippers, need to be in a misty atmosphere for use
Water droplets and Tweezers [15]	50-300 microns	No	Once two tiles are within a certain height and angle of each other the water droplet between them pulls them together	Still need external fragile grippers, tiles can get caught in energy minima and stay misaligned
Parellel and Indiviudally Controlled Electroosmosis Device	**1.5mm-TBD**	**High capacity for massively parallel**	**Electrosomosis used to form droplets to pick up objects**	**Manufacturing limitations on using 3D printed materials**

APPENDIX B

Official Test Report for Sintered Glass Disks

Liquid Permeability Sample preparation:

Tests results were most reliable when the samples were glued to adapter plates from underneath and around the edges of the sample. Silicon-rubber gasket material was used on both sides of the adapter plate and then the sample was sealed in the sample chamber by a piston.

Distilled water filled a cavity above the sample to exert a force of about 0.1 psi at open pressure in the PMI lab about 800 feet above sea level (14.4 psi).

The sample was allowed to soak in the water before the test outside and inside the sample chamber. While inside the sample chamber the scale was monitored for up to 15 hours to ensure that no liquid was bleeding through the sample while only under the head pressure of 0.1 psi. If no liquid came through, then the test was brought up incrementally to nearly the maximum of 100 psi.

Official Test Data for Sintered Glass Disks

Cornell University
Sintered glass square, sample 1 and 2
Permeability test, sample soaked in silwick, ran in LLP once, dried, re-wetted in desiccators with water
comp pressure 42.84 psi

diameter tested 27mm at 4.5 mm thickness
open valve 7, all others closed

Head pressure when filled = 0.1 psi

3:50 scale: 1.2595 down to low 1.2507 --- pressure 14.4

3:52 scale: 1.6598 increasing --- pressure 14.4 (open to air)
3:53 scale: 2.2807 increasing --- pressure 14.4
3:56 scale: 3.5040 increasing --- pressure 14.4
3:58 scale: 4.5011 increasing --- pressure 14.4
5pm scale: 26.7093 increasing --- pressure 14.4

5:03 scale 28.44 inc fast --- pressure 19.4
5.27 scale 93.73 inc faster --- pressure 19.42

Blank metal disk test, same setup as Cornell:
compression pressure at 43psi

10:47 --- scale 25.2042 --- 14.4 open to air
10:48 --- scale 25.1964
11:27 --- 24.9912 ---14.4

11:28 --- 24.9856 --- 19.42 psi
12:05 --- 24.7947 --- 19.42

12:06 --- 24.7883 --- 34.14 psi
12:47 --- 24.5899 --- 34.14 (evaporation)
1:14 --- 24.46 --- 34.3 psi
2:40 --- 23.999 --- 34.3 psi end blank, no leak

new test:
40 psi compression
black centered silicon gasket
22mm diameter testing

4:57 --- scale 74.5160 to .5207 --- 14.4 psi (open to air)
4:59 liquid filled --- waiting for scale increase
5:02 leaking again --- 74.9616 and increasing at

New test:
thicker sealing red silicon
comp pressure to 50.75 psi
5:10 --- scale 18.9872 - 18.9991 (open to air)
5:58 --- scale 23.8452 - leaking
5:59 --- scale 24.1189

New test:
comp pressure to 66.54
red silicon rubber

6:22 --- 13.364 - (open to air)
6:23 --- 13.361 - 14.38
6:40 --- 17.5 - leaking again

new test plugged red silicone, 25 mm diameter,
comp pressure 72psi
10.26 --- scale 12.0741 (open to air)
10:27 --- scale 12.0720
10:37 --- scale 12.0732
10:38 --- leak again 12.3213
10:39 --- leak 12.6142

new test:
glued to steel plate
comp pressure 71.22, plus red silicon on top
9:50 --- scale 60.96640 --- open to air
failed, leaked at open pressure

new BLANK:
metal disk with large red silicon rubber
testing leak on silicon
10:16 --- scale 13.8566 --- open to air
10:36 --- scale 13.8234 --- open air
10:38 --- 13.8191 --- 19.8
10:42 --- 13.8169

SAMPLE 1 --- new test
9 cm adapter plate diameter tested, comp pressure 81.62
psi
red silicon rubber on outside and under area tested: 28.392 mm2
triangle sample glued to metal plate
10:47 --- scale 15.8922 --- open to air
11:10 --- 15.9107 --- open air
11:37 --- 15.8965 --- open air (evaporation)
11:38 --- 15.8969 --- 19.41 psi
11:50 --- 15.8909 --- 19.41

11:52 --- 15.8901 --- 29.82 psi
12:05 --- 16.0136 --- 29.73 psi (pressure drop with
liquid loss)
2:07 --- 38.5247 --- 29.78
2:11 --- 39.1998 --- 29.64

2:12 --- 39.4612 --- 39.6 psi
2:14 --- 40.1251 --- 39.66
2:35 --- 47.8385 --- 39.52

2:36 --- 48.3684 --- 49.28 psi
2:47 --- 55.1178 --- 49.21 psi
3:10 --- 71.6579 --- 49.31 psi

SAMPLE 2 --- NEW TEST:
epoxied, smaller piece, 8 mm diameter adapter plate area tested: 20.189 mm2
sealed all holes on bottom with large red silicone-rubber
top seal with red stiff silicon
water soak overnight
6:53 --- scale 13.8668 --- 14.31 psi open air
bled through, scale full

test retry:
9:25 --- scale 13.1817 --- open air
9:30 --- 13.7216 --- open
9:51 --- 15.3186 --- open

retry2 comp pressure 86psi
11:53 --- 13.1873 g --- open
12:18 --- 13.1411 --- open
12:19 --- 13.1408 --- 19.4psi
12:58 --- 13.0954 --- 19.4
12:59 --- 13.0932 --- 29.51
1:47 --- 13.0470 --- 29.51 (evaporation, scale shift)
1:48 --- 13.0488 --- 39.64
1:50 --- 13.2608 --- 39.64
1:52 --- 13.4959 --- 39.69
2:20 --- 17.2271 --- 39.73
2:22 --- 17.5160 --- 49.56
3:38 --- 37.8455 --- 49.56
3:40 --- 38.5124 --- 59.85
4:07 --- 49.8616 --- 59.72
4:24 --- 54.5820 --- 59.86 (out of water)

4:28 --- 55.6708 --- 59.74 (water refill)
4:29 --- 56.0067 --- 59.87
4:32 --- 56.9193 --- 59.79
5:15 --- 75.8792 --- 59.84
5:18 --- 76.8695 --- 59.79
5:37 --- 85.2499 -- 59.92
5:38 --- 85.5658 --- 69.68
6:48 --- 121.5222 --- 69.85

new test - same sample as retry2 --- 5.07 mm diameter
comp pressure 88.04
7pm --- 23.9132 g --- open air

7:34 --- 23.8737 --- open
8:07 --- 23.8462 --- open

10:00 am --- 25.5210 --- open
10:02 --- 25.78087 --- 79.91
10:06 --- 29.1471 --- 79.9
10:08 --- 30.4765 --- 80.04
10:41 --- 54.0499 --- 80.05
10:47 --- 58.3126 --- 79.97

Cornell University
Sintered glass square, sample 3, area tested = 78.54 mm^2
Permeability test, sample soaked in silwick, ran in LLP once, dried, re-wetted in desiccators with water
Time --- scale (g) --- pressure (includes 14.4 standard)
9:46 --- 8.0319 --- 14.36
9:51 --- 8.0033 --- 14.4 (open)
10:51 --- 10.2833 --- open
11:01 --- 10.9763 --- open
11:02 --- 11.7254 --- 25.67 (includes
14.4)
11:16 --- 26.4314 --- 25.83
11:45 --- 56.5448 --- 25.69
11:46 --- 57.6373 --- 35.48
11:52 --- 69.0158 --- 35.74
12:25 --- water max reached
refilled water
2:32 --- 4.0734 --- 45.73
2:41 --- 23.4629 --- 45.61
2:43 --- 25.7182 --- 55.31
2:50 --- 42.7644 --- 55.40
2:51 --- 45.3241 --- 65.78
2:56 --- 59.8933 --- 65.71

APPENDIX C

Images of various frits (used and new) and frit shards under 80x magnification.

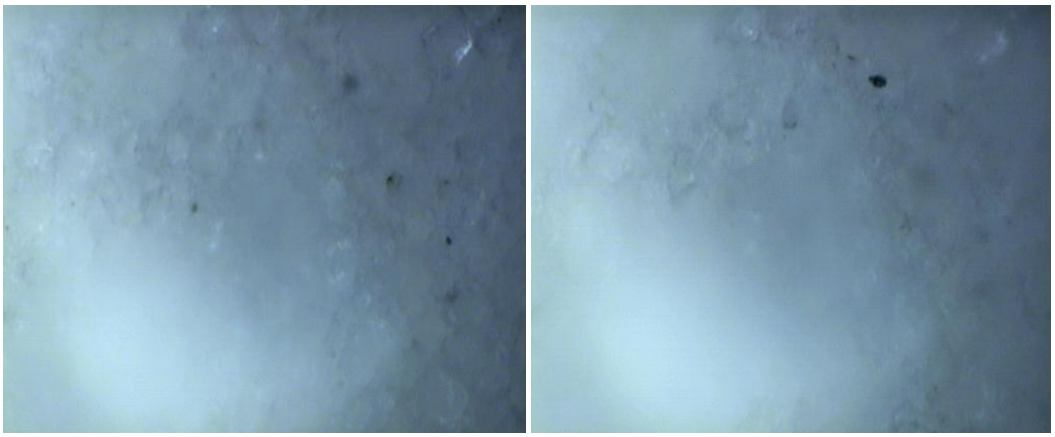

Figure B.1: New Frit

Figure B.2: Shard 1

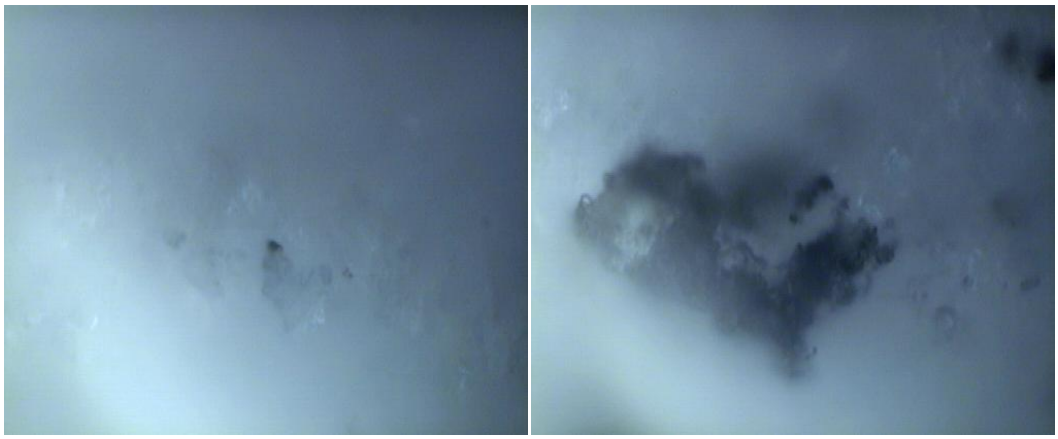

Figure B.3: Shard 2

Figure B.4: Shard 3

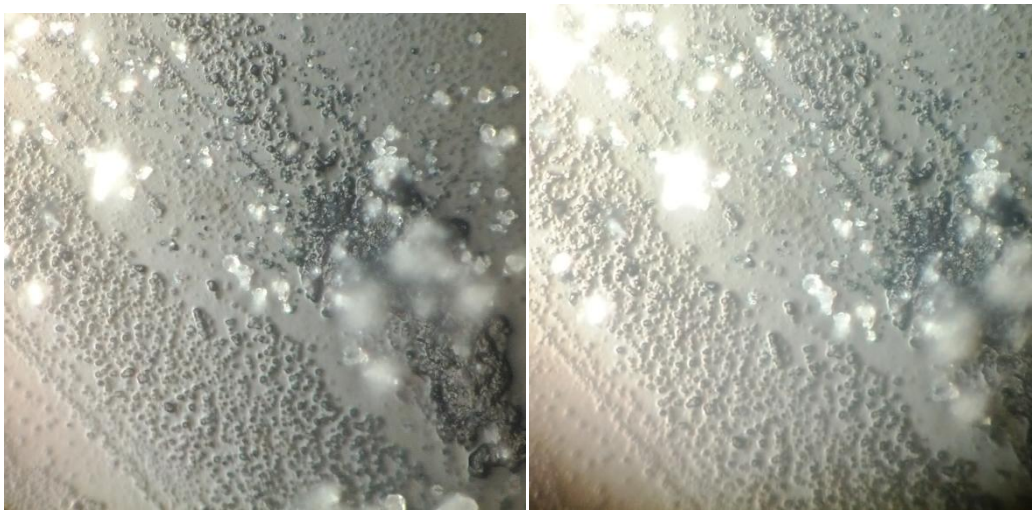

Figure B.5: Used Frit under Microscope using camera up to eye piece

REFERENCES

[1] Vogel, Michael J., Peter Ehrhard, and Paul H. Steen. "The Electroosmotic Droplet Switch: Countering Capillarity with Electrokinetics." *Proceedings of the National Academy of Sciences* 102.34 (2005): 11974-1979. Print.

[2] Vogel, Michael J., and Paul H. Steen. "Capillarity-based Switchable Adhesion." *Proceedings of the National Academy of Sciences* 107.8 (2010): 3377-381. Print.

[3] Zesch, W.; Brunner, M.; Weber, A.; , "Vacuum tool for handling microobjects with a NanoRobot," *Robotics and Automation, 1997. Proceedings., 1997 IEEE International Conference on* , vol.2, no., pp.1761-1766 vol.2, 20-25 Apr 1997.

[4] Huang, Tian, Zhanxian Li, Meng Li, Derek G. Chetwynd, and Clement M. Gosselin. "Conceptual Design and Dimensional Synthesis of a Novel 2-DOF Translational Parallel Robot for Pick-and-Place Operations." *Journal of Mechanical Design*126.3 (2004): 449. Print.

[5] Miyazaki, H.; Sato, T. "Pick and place shape forming of three-dimensional micro structures from fine particles," *Robotics and Automation, 1996. Proceedings., 1996 IEEE International Conference on* , vol.3, no., pp.2535-2540 vol.3, 22-28 Apr 1996

[6] Saito, S.; Miyazaki, H.; Sato, T.; , "Pick and place operation of a micro-object with high reliability and precision based on micro-physics under SEM," *Robotics and Automation, 1999. Proceedings. 1999 IEEE International Conference on* , vol.4, no., pp.2736-2743 vol.4, 1999

[7] Kristian Mølhave; Torben Mikael Hanse;, Dorte Nørgaard Madsen, and Peter Bøggild;, “Towards Pick-and-Place Assembly of Nanostructures,” *Journal of Nanoscience and Nanotechnology.*, vol. 4,no.3, pp.279-282, 2004.

[8] Tsui, Kenneth, Aaron A. Geisberger, Matt Ellis, and George D. Skidmore. "Micromachined End-effector and Techniques for Directed MEMS Assembly." *Journal of Micromechanics and Microengineering* 14.4 (2004): 542-49. Print.

[9] Kim, K., E. Nilsen, T. Huang, A. Kim, M. Ellis, G. Skidmore, and J.-B. Lee. "Metallic Microgripper with SU-8 Adaptor as End-effectors for Heterogeneous Micro/nano Assembly Applications." *Microsystem Technologies* 10.10 (2004): 689-93. Print.

[10] Mølhave, Kristian, Thomas Wich, Axel Kortschack, and Peter Bøggild. "Pick-and-place Nanomanipulation Using Microfabricated Grippers." *Nanotechnology* 17.10 (2006): 2434-441. Print.

[11] Rubio-Sierra, F. J., W. M. Heckl, and R. W. Stark. "Nanomanipulation by Atomic Force Microscopy." *Advanced Engineering Materials* 7.4 (2005): 193-96. Print.

[12] Sitti, M., "Survey of nanomanipulation systems," *Nanotechnology, 2001. IEEE-NANO 2001. Proceedings of the 2001 1st IEEE Conference on* , vol., no., pp.75-80, 2001.

[13] Randhawa, Jatinder S., Timothy G. Leong, Noy Bassik, Bryan R. Benson, Matthew T. Jochmans, and David H. Gracias. "Pick-and-Place Using Chemically Actuated Microgrippers." *Journal of the American Chemical Society* 130.51 (2008): 17238-7239. Print.

[14] Bo Chang; Jääskeläinen, M.; Quan Zhou; , "Microassembly combining pick-and-place and water mist," *Micro-NanoMechatronics and Human Science (MHS), 2010 International Symposium on* , vol., no., pp.333-337, 7-10 Nov. 2010

[15] Sariola, Veikko, Mirva Jaaskelainen, and Quan Zhou. "Hybrid Microassembly Combining Robotics and Water Droplet Self-Alignment." *IEEE Transactions on Robotics* 26.6 (2010): 965-77. Print.

[16] Graphic of method of images: http://www.google.com/imgres?start=377&num=10&um=1&hl=en&biw=1064&bih=707&tbm=isch&tbnid=FAaFazKvQxPh0M:&imgrefurl=http://bestofgreater.com/ericalmassy/insurance/administrator/electric-potential-difference&docid=TOznYonN1QL2QM&imgurl=http://bestofgreater.com/ericalmassy/insurance/administrator/electric-potential-difference-i14.gif&w=319&h=312&ei=rFiET_u1E9Hq0QGt0YTtBw&zoom=1&iact=hc&vpx=138&vpy=300&dur=562&hovh=222&hovw=227&tx=149&ty=167&sig=102564269364051555233&page=22&tbnh=160&tbnw=164&ndsp=16&ved=1t:429,r:12,s:377,i:333. Date visited: April 14, 2012.

[17] Hiller, Jonathan, and Hod Lipson. "Design and Analysis of Digital Materials for Physical 3D Voxel Printing." *Rapid Prototyping Journal* 15.2 (2009): 137-49. Print.

[18] Objet Material Properties Sheets: http://www.objet.com/Portals/0/docs2/Objet%20Materials%20Data%20Sheets.pdf . Date visited: April 14, 2012.

[19] Hill, Reghan J., Donald L. Koch, and Anthony J.C. Ladd. "The first Effects of fluid Inertia on flows in Ordered and Random Arrays of Spheres." *The Journal of Fluid Mechanics*448 (2001): 213-41. Print.

[20] Gennes, Pierre-Gilles De., Francoise Brochard-Wyart, and David Quere. "Chapter 10: Transport Phenomena." *Capillarity and Wetting Phenomena: Drops, Bubbles, Pearls, Waves.* New York: Springer Science Business Media, 2010. 261-87. Print.

[21] Chang, Hsueh-Chia. "Chapter 11: Bubble/drop Transport in Microchannels." *The MEMS Handbook*. CRC, 2002. 11-1-1-2. Print.

[22] Y. Fintschenko, B.J. Kirby, E.F. Hasselbrink A.K. Singh, T.J. Shepodd, "Monolithic Materials: preparation, properties, and applications: Miniature and Microchip Technologies", *Journal of Chromatography Library* (2003), Vol. 67, Ch. 25, pp. 675-685. Print.

[23] Image of electroosmosis process: http://en.wikipedia.org/w/index.php?title=File:Electroosmotic_Flow_Depiction.tiff&page=1 Date visited: April 10, 2012.

[24] Image of testing apparatus: http://pmiapp.com/testing/index.html Date visited: April 12, 2012.

[25] Information about Repellix coating: http://www.insurftech.com/ Date visited: April 1, 2012.

[26] ROBU data for pore size: http://www.robuglas.com/fileadmin/user_upload/download_documents/poresizes%20vitrapor%20e.pdf Date visited: March 15, 2012.

[27] ROBU data for pore distribution: http://www.robuglas.com/fileadmin/user_upload/download_documents/poredistribution%20vitrapor%20e.pdf Date visited: March 15, 2012.

[28] ROBU data for flow rate: http://www.robuglas.com/fileadmin/user_upload/download_documents/flowrate%20vitrapor%20e.pdf Date visited: March 15, 2012.

[29] Kirby, Brian. "Chapter 6: Electroosmosis." *Micro- and Nanoscale Fluid Mechanics: Transport in Microfluidic Devices*. New York: Cambridge UP, 2010. 131-52. Print.

[30] Method of Images: http://www.astro.uvic.ca/~tatum/elmag/em01.pdf Date visited: April 20, 2012.

[31] Kirby, Brian. "Chapter 15: Fluid Transport." *Micro- and Nanoscale Fluid Mechanics: Transport in Microfluidic Devices*. New York: Cambridge UP, 2010. 336-350. Print.

[32] D. Barz, M. Vogel, P. Steen, "Determination of the Zeta Potential of Porous Substrates by Droplet Deflection. I. The Influence of Ionic Strength and pH Value of an Aqueous Electrolyte in Contact with a Borosilicate Surface," *Langmuir*, 2009 Vol. 25, pp.1842-1850.

[33] Griffiths, David Jeffrey. *Introduction to electrodynamics*. 3. ed. Upper Saddle River, NJ. Prentice Hall, 1999. Print.

[34] H. Lengerich, M. Vogel, P. Steen, "Dynamics and stability of volume-scavenging drop arrays: Coarsening by capillary," *Physcia D* (2009) Vol. 238, pp. 531-39.

[35] J. Hiller, H. Lipson, “Rapid Assemblers for bridging the mesoscale integration gap,” Nature 2012 (under review).